Orbital Averaging and Control Parametrization for Many-Revolution Low-Thrust Transfer Trajectory Optimization

With an Application to Active Debris Removal

R.A. Klavers

Delft University of Technology

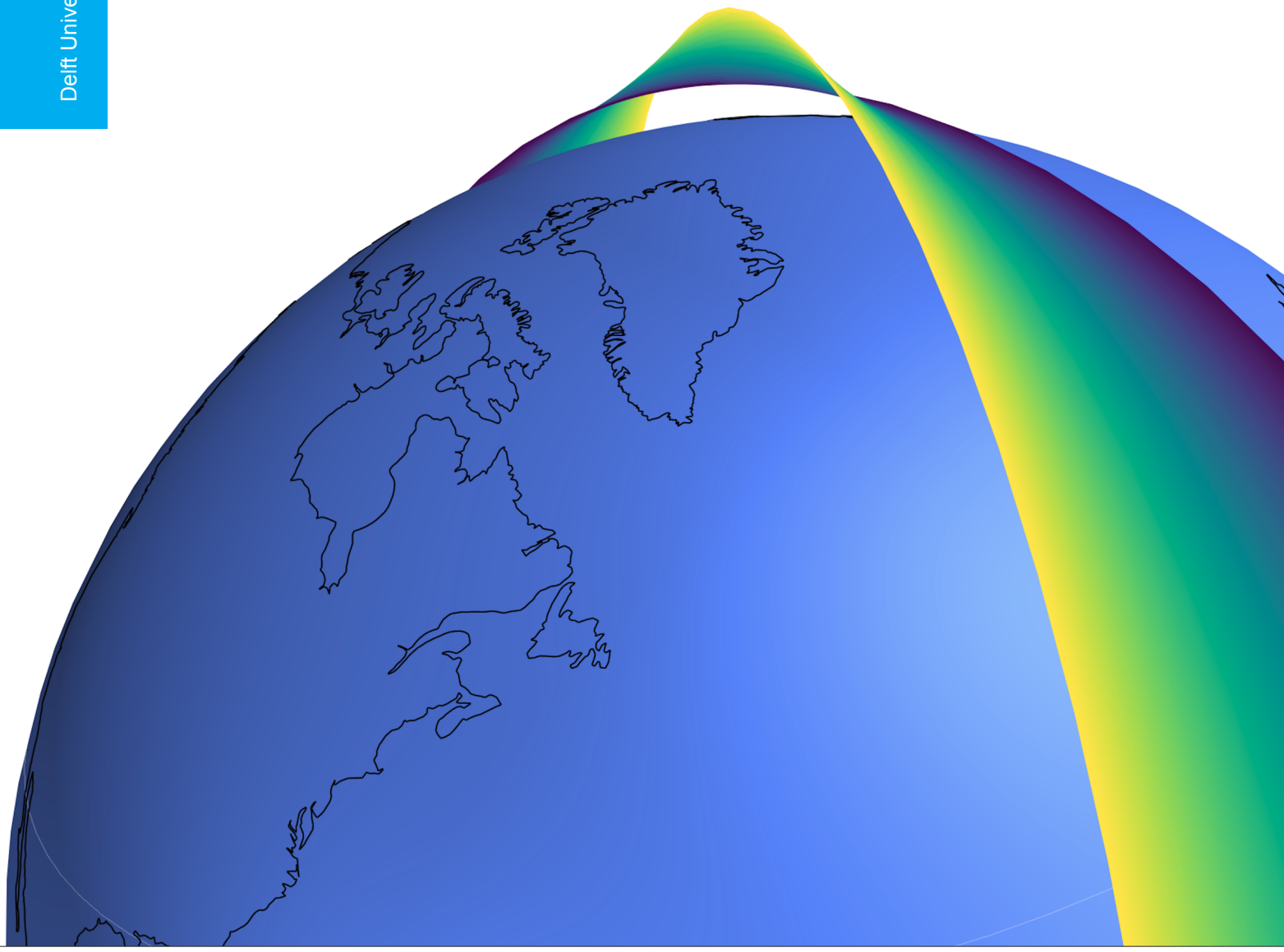

TU Delft Delft University of Technology

Challenge the future

Orbital Averaging and Control Parametrization for Many-Revolution Low-Thrust Transfer Trajectory Optimization

With an Application to Active Debris Removal

by

Robert Alexander Klavers

to obtain the degree of

Master of Science

in Aerospace Engineering, Track Spaceflight
at Delft University of Technology
to be defended publicly on Friday, October 29, 2021

Student Number:	4222660		
Supervisor:	Ir. R. Noomen	TU Delft	
Committee:	Prof. dr. L.L.A. Vermeersen	TU Delft,	Committee chair
	Dr. S. Speretta	TU Delft,	Examiner
	Ir. R. Noomen	TU Delft,	Supervisor

An electronic version of this thesis is available at `http://repository.tudelft.nl/`.

TU Delft

Preface

Before starting my studies at Delft University of Technology, I remember attending a lecture on the problem of space debris at the faculty of Aerospace Engineering, part of the university open days. Despite my passion for space exploration, I nonetheless decided there was too much 'aero' and too little 'space' in the curriculum, so I went on to obtain my bachelor's degree in Computer Science instead. After a Spaceflight minor, lengthy discussions with Ron Noomen, and several months of additional courses, I ended up at Aerospace Engineering after all. Perhaps it's somewhat poetic that I ended up with the space debris problem in my master thesis.

Although that was the best decision I had made in my academic career, these past two years ended up being more difficult. An unexpected global pandemic and personal hurdles needed to be overcome, but I am proud to have gotten there in the end. Of course, I would not have been able to get there on my own, and I have several people to thank for that.

First and foremost, I want to thank my supervisor Ron Noomen, without whom I would not have even been in the position to start my thesis work under his guidance. It wasn't always smooth sailing, but thanks to our weekly meetings, filled with encouraging discussions and constructive feedback, I was able to stay on track. I want to thank Marie for the help with Tudat. My friends in Delft for providing the necessary distractions from the thesis life. AJ, for patiently listening to my ramblings. Lastly, my family, especially my parents and sister, for your encouragement, support, and belief.

I did not use the most direct path to get here, but I do not regret taking it a single second.

Robert Klavers
Delft, October 2021

Abstract

The use of Solar Electric Propulsion (SEP) as a primary propulsion system for Earth-centered spacecraft is rapidly increasing, due to its high efficiency and development throughout the last decades. An expanding proportion of commercial satellites uses electronic propulsion, where this was formerly the domain of Solar-System exploration or station-keeping. make it an increasingly attractive choice. Compared to traditional chemical propulsion systems, significant amounts of propellant can be saved, and thus lowering costs. With this development come additional challenges from a trajectory optimization perspective, but also new applications that can benefit from these developments.

The problem of low-thrust trajectory optimization is by no means a novel area of study, having a heritage tracing back multiple decades. Despite this, it remains an active field of research, especially for the Earth-centered many-revolution trajectory design. One of the applications is Active Debris Removal (ADR), aiming to reduce the space debris problem, by performing a rendezvous transfer to a debris object, attach to it and perform a combined maneuver to a decay orbit. Clearly, using a limited amount of propellant opens up the possibility to target and retrieve a series of debris objects, so it has a potential benefit over chemical propulsion implementations. This thesis project encompasses a hybrid implementation using control parametrization and Orbital Averaging (OA) that aims to optimize such a trajectory, for preliminary design of many-revolution, Earth-centered, low-thrust trajectories.

The method uses control parametrization to reduce the complexity of the optimization problem, by discretizing the control history at select points. This parametrization is done by using the necessary conditions from optimal control theory. The spacecraft state, governed by the resulting design parameters, is then propagated using OA to vastly reduce the computations required and allowing the computation of a large number of trajectories. Finally, these trajectories are then optimized using a self-adaptive variant of Differential Evolution (DE), greatly reducing user input and manual tuning required. Furthermore, several improvements and enhancements compared to previous authors were implemented to increase robustness and computation times.

Results for the minimum-time and minimum-propellant GTO-to-GEO transfer problem are presented. Solutions for the minimum-time transfer demonstrated robust convergence within 0.06% or 0.1 days of each other. When including the effect of Earth's shadow on thrust, the optimizer was unable to reliably converge for the worst-case scenario, i.e. the apogee of the initial orbit lies in Earth's shadow. With local optimal differences of up to 5.39%, as much as 6 days, its performance could not be verified. Adjusting the initial orbit with perigee in Earth's shadow, showed significant improvement in terms of convergence reliability (within 0.33%), as well as improved consistency compared to the results obtained by previous authors. The minimum-propellant solutions, using coasting arcs, closely resembled the optimal results obtained by Jimenez-Lluva (2017).

The second case deals with the problem of ADR, studying the minimum-time orbit-to-orbit transfer problem from a parking orbit in Low Earth Orbit (LEO) to the orbit of a derelict Vostok second stage. Both a simple co-planar transfer without additional perturbations and a more complex transfer were considered, the latter requiring a plane change in inclination of $2°$ and an additional change in Right Ascension of the Ascending Node (RAAN). Without any additional tuning or a-priori estimates, consistent results were obtained, within 0.7% (0.12 days) for the simple transfer and 2.6% (0.88 days) for the more complex transfer. When requiring additional plane changes and a final RAAN of $-45°$, the time-of-flight showed an increase of 97%, emphasizing the importance of minimizing required plane changes.

Although the implemented hybrid optimization method using OA shows great performance, there is room left for improvement, in particular for the OA propagation. Several approximations can yield an unacceptable error accumulation, especially in the perturbed LEO environment, where the orbital elements display significant short-period variations. Furthermore, taking into account shadow conditions needs further improvement to ensure its validity in the averaging expression. Nonetheless, the method has shown a large amount of flexibility, requiring minimal user input and no manual tuning of the optimization algorithm. Taking into account additional perturbations or operational constraints is possible without the need of further derivations. Additionally, no initial guess is required to find near-optimal solutions, increasing its flexibility further.

Contents

List of Abbreviations

ADR	Active Debris Removal
AOF	Aggregate Objective Function
AOP	Argument of Periapsis
CI	Continuous Integration
DE	Differential Evolution
ECI	Earth-Centered-Inertial
EOM	Equations of Motion
EP	Electric Propulsion
ESA	European Space Agency
GA	Genetic Algorithm
GEO	Geostationary Earth Orbit
GTO	Geostationary Transfer Orbit
IVP	Initial Value Problem
JAXA	Japan Aerospace Exploration Agency
JPL	Jet Propulsion Laboratory
LEO	Low Earth Orbit
MADR	Multiple Active Debris Removal
MEE	Modified Equinoctial Elements
NAIF	NASA's Navigation and Ancillary Information Facility
NASA	National Aeronautics and Space Administration
NEP	Nuclear Electric Propulsion
NLP	Non-linear Programming
OA	Orbital Averaging
OCP	Optimal Control Problem
OT	Optimization Tool
PaGMO	Parallel Global Multiobjective Optimizer
pDE	pagmo Differential Evolution
RAAN	Right Ascension of the Ascending Node
RK4	fourth-order Runge-Kutta
RKF	Runge-Kutta Fehlberg
SaDE	Self-Adaptive Differential Evolution
SEP	Solar Electric Propulsion
SQP	Sequential Quadratic Programming
SSO	Sun-Synchronous Orbit
TLE	Two-Line Element set
TOF	Time of Flight
TPBVP	Two Point Boundary Value Problem
Tudat	TU Delft Astrodynamics Toolbox
USSA	United States Standard Atmosphere

List of Symbols

Notation

$\mathbf{x}$	Vector
$\hat{\mathbf{x}}$	Unit vector
$\mathbf{A}$	Matrix
$\mathbf{x}^{\mathsf{T}}$	Transpose
$\dot{x}$	Derivative of x w.r.t. time
$\ddot{x}$	Second derivative of x w.r.t. time

Constants

c	Speed of light in vacuum	$299\,792\,458\,\mathrm{m\,s^{-1}}$
g_0	Standard acceleration due to Earth's gravity	$9.806\,65\,\mathrm{m\,s^{-2}}$
G	Universal gravitational constant	$6.674\,30 \times 10^{-11}\,\mathrm{m^3\,kg^{-1}\,s^{-2}}$
R_E	Earth's equatorial radius	$6378.1366\,\mathrm{km}$

Greek Symbols

α	Yaw steering angle	rad
β	Pitch steering angle	rad
η	Thruster efficiency	-
γ	Flight path angle	rad
λ	True longitude	rad
μ	Gravitational parameter	$\mathrm{m^3\,s^{-2}}$
Ω	Right ascension of the ascending node	rad
ω	Argument of pericenter	rad
ρ	(Atmospheric) density	$\mathrm{kg\,m^{-3}}$
θ	True anomaly	rad
φ	Polar angle	rad

Roman Symbols

A	(Cross-sectional) area	$\mathrm{m^2}$
a	Semi-major axis	m
C_D	Drag coefficient	-
C_R	Reflectivity coefficient	-
E	Eccentric anomaly	rad
e	Eccentricity	-
F	Force	N

H	Specific angular momentum	$m^2\,s^{-1}$
I_{sp}	Specific impulse	s
i	Inclination	rad
M_0	Mean anomaly at epoch	rad
m_0	Spacecraft dry mass	kg
m_f	Spacecraft final mass	kg
m_p	Spacecraft propellant mass	kg
M	Mean anomaly	rad
m	Mass	kg
n	Mean motion	$rad\,s^{-1}$
$P_{n,m}$	Associate Legendre polynomial of degree n and order m	-
P_n	Legendre polynomial of degree n	-
P	Power	W
p	Semi-latus rectum	m
r	Radial distance	m
T_p	Orbital period	s
T	Thrust force	N
t	Time	s
U	Gravitational potential	$m^2\,s^{-2}$
u	Argument of latitude	rad
W	Power density	$W\,m^{-2}$

Sets

$a, e, i, \omega, \Omega, \theta$	Keplerian elements	-
a_R, a_S, a_W	Acceleration in RSW-frame	$m\,s^{-2}$
p, f, g, h, k, L	Equinoctial elements	-
$x, y, z, \dot{x}, \dot{y}, \dot{z}$	Cartesian position and velocity	m, $m\,s^{-1}$

1 Introduction

The concept of Electric Propulsion (EP) systems for spacecraft propulsion was introduced in the early 20th century (Choueiri, 2004), it has been regarded as an attractive option for spacecraft propulsion due to its high efficiency compared to traditional chemical propulsion. The high-thrust chemical propulsion engines are generally limited to a specific impulse of a few hundred seconds, whereas EP can reach specific impulses in the order of thousands of seconds, allowing significantly larger velocity changes for equal propellant mass. This comes at the cost of reduced thrust and consequently significantly longer burn times as the low-thrust force of the engine is applied continuously during the maneuver. Initially, its use was limited to station-keeping, technology demonstration, and attitude control (Martinez-Sanchez and Pollard, 1998). Later, in the late 1990s and early 2000s it saw use as a primary propulsion system for solar system exploration missions such as National Aeronautics and Space Administration (NASA) Deep Space 1 (Rayman et al., 2000), Japan Aerospace Exploration Agency (JAXA) Hayabusa (Kawaguchi et al., 2008) and European Space Agency (ESA) SMART-1 (Racca et al., 2002). The technology eventually also made its way to the commercial domain and started seeing use for Earth-orbit purposes, such as Eutelsat or Airbus ABS-3 (Henry, 2017).

A Solar Electric Propulsion (SEP) system is characterized by its low thrust and high efficiency when compared to traditional chemical propulsion systems and its use of solar panels to provide the power required for the propulsion system. From a trajectory optimization point of view, using a low-thrust propulsion system such as SEP[1] presents a different set of challenges. Thrust is now acting continuously during (parts) of the transfer trajectory instead of being modeled as impulsive shots at discrete points in the trajectory, changing the dynamics of the problem and vastly increasing the domain of possible solutions.

Earth-centered transfer trajectories show additional properties that need to be taken into account. The low orbital period, when compared to interplanetary trajectories means that an arbitrary transfer will consist of many orbital revolutions about the Earth, i.e. a many-revolution transfer trajectory. Additionally, Earth's irregular gravity field and aerodynamics due to its atmosphere present an extra set of challenges. However, these properties can also be exploited. From the perspective of low-thrust trajectory optimization, the many-revolution nature of the problem can be used in an Orbital Averaging (OA) approach, reducing required propagation time. From a mission design point of view, Earth's oblateness can be used to design specific trajectories such as Sun-Synchronous Orbit (SSO) trajectories, exploiting the effects caused by the irregular gravity field of the Earth.

A mission concept that can take full advantage of both low-thrust propulsion systems and the previously mentioned optimization problems is the concept of Active Debris Removal (ADR). The number of space debris objects, i.e. the objects in Earth orbit with no active control or functionality, is increasing. Collision events such as the collision between the Iridium-33 communication satellite and the derelict Russian Kosmos-2251 in 2009 could cause a cascading effect, dubbed the *Kessler Syndrome* (Kessler and Cour-Palais, 1978). As the launches to LEO have an increasing rate and simulations show that the number of objects in LEO will keep increasing, even with adherence to mitigation and no future launches (Liou et al., 2013), the necessity for ADR becomes apparent.

[1] Other examples are solar sailing or Nuclear Electric Propulsion (NEP)

It was exactly this problem that sparked the idea for this thesis project, to contribute to solutions for the optimization of Earth-centered many-revolution low-thrust transfer trajectories to objects in LEO for the purpose of ADR. In particular, through the use of a low-thrust propulsion system, reducing propellant needs, the targeting of multiple debris objects in a single mission, i.e. Multiple Active Debris Removal (MADR). The research in this project aims to develop a low-thrust trajectory optimization tool, taking into account most relevant perturbations, to allow preliminary mission design of ADR transfer trajectories. Based on an extensive literature study (Klavers, 2020), a hybrid methodology, or control parametrization technique was selected (Jimenez-Lluva, 2017). The remainder of this section will formalize the project goal and research questions.

1.1. Problem Statement

During the literature study performed prior to this thesis project (Klavers, 2020), low-thrust transfer trajectory optimization techniques were studied to identify promising areas of study, and aim to improve the capabilities of the preliminary low-thrust trajectory design tools available in TU Delft Astrodynamics Toolbox (Tudat). Eventually, a control parametrization method, utilizing OA, was selected with the goal of optimizing transfer trajectories to space debris in LEO. This method has great flexibility, utilizing the strengths of direct and indirect optimization techniques, and can exploit the specific properties of Earth-centered low-thrust transfer trajectories by using an OA approach.

It was concluded that the area of active space debris removal is an area of research with many open unanswered questions, one of which is the optimization of transfer trajectories to debris objects, using a low-thrust propulsion system. Specifically, to find optimal trajectories between decay orbits and specific debris objects. Ultimately the purpose of which is to automatically find time-optimal sequences of debris that allow removal of at least five objects per year from certain orbital regimes. Several techniques for low-thrust trajectory optimization for preliminary design were discussed and a hybrid control parametrization method was selected. This method combines the strengths of both indirect and direct optimization and is a promising development that could yield good results for this specific problem.

The work in this thesis is considered an iteration on the MSc thesis by Jimenez-Lluva (2017). He included mass as part of the control parametrization derivation, which allows optimization of minimum-propellant transfer problems that can benefit from coasting arcs. However, Jimenez-Lluva limited himself to transfer trajectories to GEO and included limited perturbations. Therefore this project aims to improve in certain areas: Take into account relevant perturbations for transfers problems in LEO, and improve the performance of the OA algorithm employed.

From these conclusions, several research questions and project goals were derived. The former is aimed a developing a scientific understanding and better understand the applicability of the hybrid method. The latter is aimed at the project itself, and the expansion of the capabilities of Tudat.

1.1.1. Research Questions

The following research question was formed based on the literature study performed:

> *To what extent can the hybrid control parametrization optimization method, including orbital averaging, be used to find optimal low-thrust transfer trajectories to space debris objects in low Earth orbit, with the ultimate purpose of enabling its use in preliminary trajectory design of active debris removal missions?*

This question can be divided into a number of sub-questions to allow easier discussion and prioritization:

1. To what extent can the method be improved by implementing recommendations by the original author.
   (a) To what extent will self-adaptive DE in Parallel Global Multiobjective Optimizer (PaGMO) improve the overall optimization process?
   (b) To what extent will variable-step integration improve the computational effort, especially for OA?
2. Can the hybrid optimization method be successfully used to optimize low-thrust transfer trajectories in LEO?
   (a) How do the atmospheric drag and gravity field perturbations in LEO impact the optimization process?
   (b) How do requirements such additional plane changes influence the results?

Initially, the research questions included an additional focus on *multiple* ADR, i.e. finding optimal trajectories between sequences debris objects. However, at an early stage, this was deemed infeasible. The requirement of debris sequence selection and sequence optimization would increase the scope excessively. Nonetheless, Chapter 5 will briefly touch upon this problem. The main research question of this project was therefore slightly adapted from the literature study.

1.1.2. Project Goals

These research questions are translated to overall project goals, the overall research goal is stated as:

> *Expand the Tudat low-thrust optimization suite with a novel hybrid optimization approach in order to improve optimization capabilities for the many-revolution problems, such that we can find optimal solutions for the multiple active space debris removal problem.*

from which the following sub-goals are derived:

1. Implement and Test the hybrid optimization method
   (a) Implement and test Orbital Averaging
   (b) Implement and test optimization algorithm improvements
   (c) Perform verification using the cases presented by Jimenez-Lluva
   (d) Implement coasting arc mechanism
2. Perform a case study on single debris object transfer optimization.
   (a) Set up single transfer from parking/decay orbit to debris object orbit
   (b) Investigate performance of the hybrid method
3. Find time-optimal sequence of debris objects using manual target selection.
   (a) Investigate the viability of OA optimization for target selection purposes
   (b) Set up manual debris removal sequence (based on achievable range)
   (c) Attempt automatic (global) optimization procedure for sequence selection

1.2. Report Structure

This thesis project report is divided into six chapters. Chapter 2 describes all methods and techniques used to implement the method, including fundamental astrodynamics, numerical integration and propagation methods, optimal control, and optimization algorithms. Chapter 3 discusses how the implemented methodology was tested, this includes testing of the perturbations and the implementation of the propagator. Chapter 4 describes the results obtained for the Geostationary Transfer Orbit (GTO)-to-Geostationary Earth Orbit (GEO) transfer problem and the discussion thereof. Chapter 5 consists of the results and analysis of several transfer trajectory optimizations to the orbit of a space debris object in LEO. Finally, Chapter 6 finishes with the conclusions gained from this project and several recommendations for future work and research.

2

Methodology

This chapter will discuss everything that is required for the implementation of the hybrid methodology in an Optimization Tool (OT). A high-level overview of the followed methodology is shown in Figure 2.1 in the form of a flowchart. In general terms: the global DE optimization method is used to find an optimal design vector. To find this optimal solution, many different trajectories will need to be propagated, given a user-defined initial spacecraft state and a design vector generated by the DE algorithm. These are propagated through either a Continuous Integration (CI) process or through the use of OA, which uses an 'embedded' CI. Through the use of OA, computation times can be greatly reduced. The final state obtained by the propagator is used by the optimizer to compute a fitness value, which is fed back into the optimizer to compute a new set of design vectors, ultimately arriving at an optimal solution.

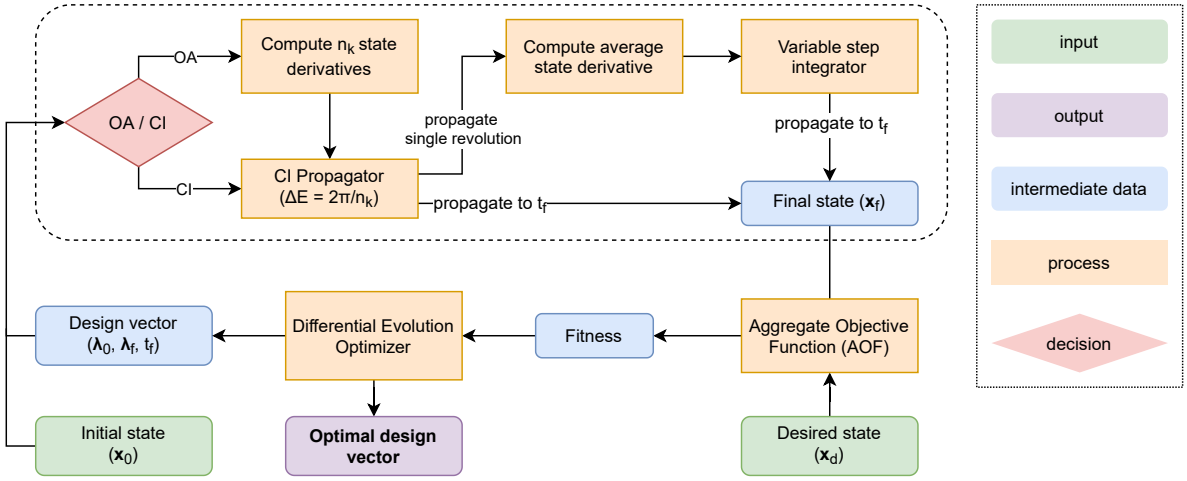

Figure 2.1: High-level overview flowchart of the Optimization Tool (OT).

The Optimization Tool (OT) leans on two concepts: 1) hybrid optimization of the optimal control problem (control parametrization), and 2) orbital averaging for reducing computation times. The hybrid methodology aims to use the advantages of indirect optimization methods in a direct approach, using the strengths of both. It uses control parametrization to reduce the number of parameters defining the control history, by using the optimality conditions from the Optimal Control Problem (OCP) to find the optimal control (thrust steering angles and magnitude) as a function of the system state and co-states. Indirect methods fully derive the resulting equations to solve the Two Point Boundary Value Problem (TPBVP), whereas the direct approach uses these expressions directly to parametrize the control history.

Before describing the full methodology in detail, Section 2.1 briefly summarizes previous work on the hybrid method. Then, Section 2.2 describes all relevant fundamental astrodynamics required, such as references frames,

Equations of Motion (EOM), and orbital perturbations. Section 2.3 discusses propagation methods, namely numerical integration and state propagation, detailing the CI and OA algorithms. Finally, Section 2.4 deals with the optimization problem. This encompasses the optimal control theory used to parameterize the problem and the global optimization method, DE, in more detail.

2.1. Hybrid Low-Thrust Trajectory Optimization

The specific control parametrization approach was initially proposed by Kluever and Pierson (1995), where the problem was transformed to a Non-linear Programming (NLP) problem. They assumed constant thrust and only optimized the two steering angles. Later, they expanded this approach by incorporating OA, averaging the state derivatives over a single revolution, and propagated the state averages for a set number of days (Kluever, 2010). They showed competitive performance for the minimum-time LEO-to-GEO and GTO-to-GEO transfer problems.

Work in preceding theses included the work done by Boudestijn (2014), he re-derived the optimal control expressions in terms of Modified Equinoctial Elements (MEE) and included eclipse conditions. This was further improved upon by Gómez-Jenkins (2015), incorporating perturbations due to non-spherical distribution of Earth's gravity field and gravitational attraction due to third bodies. This was done by deriving averaged expressions for the state derivatives caused by these perturbing accelerations. Jimenez-Lluva (2017) added a coasting arc mechanism by incorporating thrust in the control law, leading to a bang-bang control problem, based on the switching function derived by Gao and Kluever (2004). A summary of reference implementations and their specific properties is presented in Table 2.1: The propagation logic used to represent system state and control law derivations. The perturbations that were incorporated such as non-spherical gravity distribution, aerodynamic drag, or third-body gravitation attractions. Options for the thrust magnitude, all allow constant thrust and incorporating zero thrust in Earth's shadow.

As introduced in Section 1.1, the work in this project is considered an iteration of the work by Jimenez-Lluva (2017), aiming to further refine the optimization process and increasing its applicability. This is done by implementing several enhancements to improve optimization behavior, such as co-state scaling and using Self-Adaptive Differential Evolution (SaDE). Additionally, aerodynamic drag perturbations are also taken into account as the additional case of low-thrust transfers in LEO are investigated. With these improvements, the novel application to transfer trajectories to space debris object orbits in LEO will be investigated.

Table 2.1: Properties of hybrid optimization implementation by previous authors. Propagation describe spacecraft state and control law derivations

Source	Propagation	Perturbations	Thrust Opts.	Optimizer
(Kluever, 2010)	Keplerian	gravity	constant Earth-shadow variable I_{sp}	SQP (*fmincon*)
(Boudestijn, 2014)	Keplerian, MEE	None	constant Earth-shadow	DE
(Gómez-Jenkins, 2015)	MEE	gravity, drag third bodies	constant Earth-shadow	DE
(Jimenez-Lluva, 2017)	MEE, mass	gravity	constant Earth-shadow coasting arcs	DE
This project	MEE, mass	gravity, drag	constant Earth-shadow coasting arcs	SaDE

2.2. Astrodynamics

2.2.1. Reference Frames

Three reference frames are used in this work: The Earth-Centered-Inertial (ECI) frame is used for the trajectory output and internally by Tudat. Furthermore, ephemerides of additional bodies such as the Sun are also obtained in this frame. The RSW-frame, as shown in Figure 2.2, is used to describe all perturbing accelerations on the spacecraft, this is the frame used by previous authors. Additionally, the EOM based on orbital elements can be described in this frame through the Gaussian form of Lagrange's planetary equations. Closely related to the RSW-frame is the NTW-frame, whose direction is instead related to the velocity vector. This frame is occasionally used to represent the thrust vector, and thrust steering angles, with respect to the velocity.

Inertial Frame

To represent the state of the spacecraft and ephemerides of other celestial bodies, an ECI reference frame is typically used. An ECI frame is an inertial frame, i.e. fixed with respect to the stars. More specifically, the J2000 ECI frame is used. Its origin is at the center of the Earth, with the x- and y-axes in the equatorial plane and the z-axis in the direction of the North Pole. The J2000 frame defines the fixed x-axis as the direction of mean equinox at noon on January 1st, 2000. J2000 was selected as it is commonly used and is directly available in Tudat. Note that the definition ECLIPJ2000 is also encountered, specifically in the SPICE software; this frame is defined with respect to Earth's mean ecliptic and equinox at epoch J2000, i.e. the x- and y-axes are in the ecliptic plane, as opposed to the equatorial plane.

Local Frame

A local, co-moving frame is often used to study effects relative to the spacecraft such as relative motion, or perturbing forces. This project uses the RSW-frame (radial, transverse, cross-track), and is defined as:

$$\mathbf{Q} = \left[\hat{\mathbf{R}}, \hat{\mathbf{S}}, \hat{\mathbf{W}}\right] = \left[\frac{\mathbf{r}}{||\mathbf{r}||}, \frac{(\mathbf{r}\times\mathbf{v})\times\mathbf{r}}{||\mathbf{r}\times\mathbf{v}||||\mathbf{r}||}, \frac{\mathbf{r}\times\mathbf{v}}{||\mathbf{r}\times\mathbf{v}||}\right] \tag{2.1}$$

where $\mathbf{r}$ and $\mathbf{v}$ are the Cartesian position and velocity, respectively. The R-direction aligned with the radius vector, the W-direction is in line with the angular momentum vector and the S-direction completes the right-handed frame in the direction of, but not necessarily in line with, the velocity vector. The RSW-frame will be used to represent the perturbing accelerations and for the derivation of the optimal steering angles, as will be discussed in Section 2.4.2. In contrast, for the similar NTW-frame (Normal, Tangential, Cross-track) the N-direction is *normal* to the velocity vector, T-direction is tangential to the orbit and the W-direction completes the right-handed system equal to the RSW-frame. Both frames are shown in Figure 2.2.

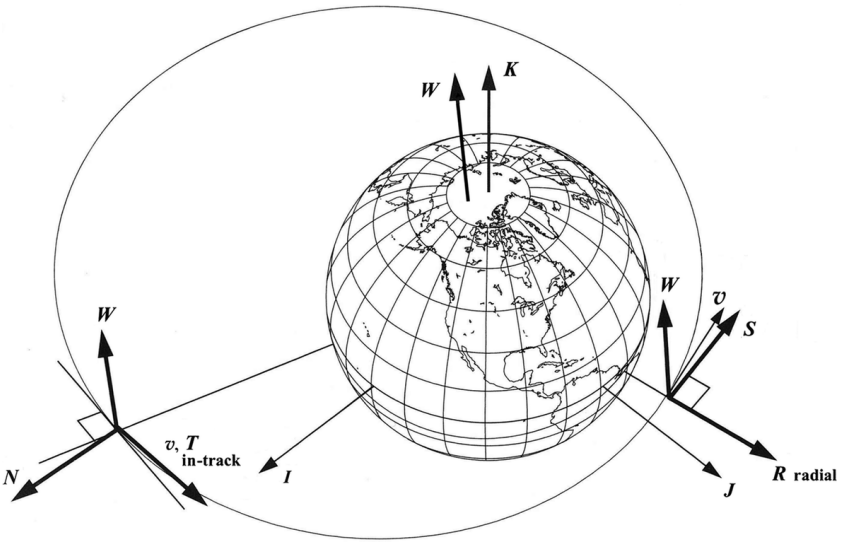

Figure 2.2: Illustration of the RSW- and NTW-frames (Vallado and McClain, 2001).

2.2.2. Coordinate Systems

In this project, three coordinate systems are used to represent the spacecraft state: Cartesian coordinates representing position and velocity in inertial space, and the two orbital element sets: Keplerian elements and Modified Equinoctial Elements (MEE), which are used to represent the orbital shape and orientation, and the position of the spacecraft therein.

Cartesian Coordinates

In a Cartesian coordinate system in three dimensions the values x, y, z denote the distance from the origin to the projection of the point on each of the three axes. The state vector includes this position $\mathbf{r}$ and its time derivative, the velocity $\mathbf{v}$:

$$\mathbf{x} = [x, y, z, \dot{x}, \dot{y}, \dot{z}]^\mathsf{T} \tag{2.2}$$

Orbital Elements

As Cartesian coordinates are generally unwieldy when representing orbits, other element sets are often used. The traditional Keplerian orbital elements are the most known:

$$\mathbf{oe} = [a, e, i, \Omega, \omega, \theta]^\mathsf{T} \tag{2.3}$$

These consist of the semi-major axis a, eccentricity e, inclination i, RAAN Ω, argument of pericenter ω, and true anomaly θ. In Figure 2.3 a geometric representation of the angular parameters $[i, \omega, \Omega, \theta]$, is shown.

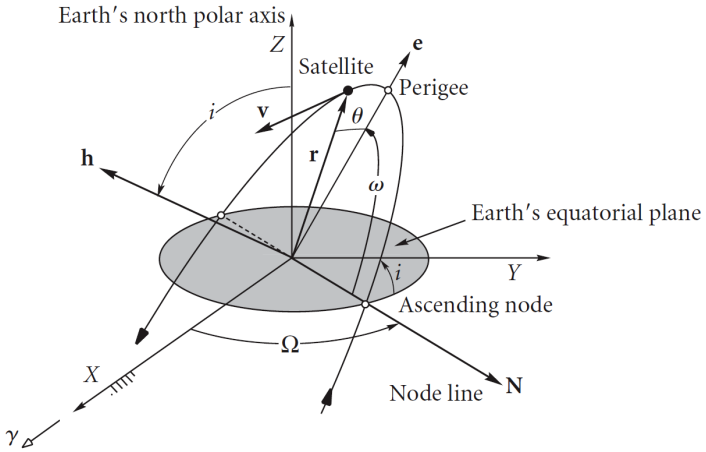

Figure 2.3: Illustration of the angular parameters in the classical Keplerian elements (Curtis, 2008).

Instead of the true anomaly, the mean anomaly, M or eccentric anomaly E, can also be used. The eccentric anomaly is measured with respect to the center of the ellipse. The mean anomaly is directly related to time:

$$M = n(t - \tau) \tag{2.4}$$

where n is the mean motion, t the current time, and τ the time of perigee passage. Its relationship to the eccentric- and true anomaly is described through Kepler's Equation:

$$M = E - e \sin E \tag{2.5}$$

where e is the eccentricity. As there is no closed-form solution when solving for E, it is solved numerically. For example through Newton's method.

Although these elements are intuitive to use and have several attractive properties such as the slow change of each element, apart from θ, there are two singularities that can cause problematic behavior. Ω is undefined for $i = 0, \pi$

and ω is undefined for $e = 0$. To circumvent his, MEE are used. MEE are an alternative set of six elements, introduced by Walker et al. (1985). These elements only show a singularity for $i = \pi$. Because pure retrograde trajectories are not studied in this project, this singularity can be safely ignored. MEE are defined in terms of the Keplerian elements by Equations 2.6:

$$p = a(1 - e^2) \tag{2.6a}$$

$$f = e\cos(\omega + \Omega) \tag{2.6b}$$

$$g = e\sin(\omega + \Omega) \tag{2.6c}$$

$$h = \tan\left(\frac{i}{2}\right)\cos(\Omega) \tag{2.6d}$$

$$k = \tan\left(\frac{i}{2}\right)\sin(\Omega) \tag{2.6e}$$

$$L = \Omega + \omega + \theta \tag{2.6f}$$

and can be converted back to Keplerian elements using Equations 2.7:

$$a = \frac{p}{(1 - f^2 - g^2)} \tag{2.7a}$$

$$e = \sqrt{f^2 + g^2} \tag{2.7b}$$

$$i = 2\arctan\left(\sqrt{h^2 + k^2}\right) \tag{2.7c}$$

$$\Omega = \text{atan2}\left(\frac{k}{\sqrt{h^2 + k^2}}, \frac{h}{\sqrt{h^2 + k^2}}\right) \tag{2.7d}$$

$$\omega = \arctan\left(\frac{g}{f}\right) - \arctan\left(\frac{k}{h}\right) = \text{atan2}(gh - fk, fh + gk) \tag{2.7e}$$

$$\theta = L - \Omega - \omega \tag{2.7f}$$

When required, the state in MEE can be converted to Cartesian position and velocity by Equations (2.8) and (2.9) (Betts, 2000).

$$\mathbf{r} = \begin{bmatrix} \frac{r}{s^2}\left(\cos L + (h^2 - k^2)^2\cos L + 2hk\sin L\right) \\ \frac{r}{s^2}\left(\sin L - (h^2 - k^2)^2\sin L + 2hk\cos L\right) \\ \frac{2r}{s^2}(h\sin L - k\cos L) \end{bmatrix} \tag{2.8}$$

$$\mathbf{v} = \begin{bmatrix} -\frac{1}{s^2}\sqrt{\frac{\mu}{p}}\left(\sin L + (h^2 - k^2)^2\sin L - 2hk\cos L + g - 2fhk + (h^2 - k^2)^2 g\right) \\ -\frac{1}{s^2}\sqrt{\frac{\mu}{p}}\left(-\cos L + (h^2 - k^2)^2\cos L + 2hk\sin L - f + 2ghk + (h^2 - k^2)^2 f\right) \\ \frac{2}{s^2}\sqrt{\frac{\mu}{p}}(h\cos L + k\sin L + fh + gk) \end{bmatrix} \tag{2.9}$$

2.2.3. Equations of Motion

In general, the motion of a spacecraft about a central body, subject to one or more perturbing forces, can be described as:

$$\ddot{\mathbf{r}} = -\frac{\mu}{r^3}\mathbf{r} + \mathbf{a}_{pert} \tag{2.10}$$

where μ is the gravitational parameter of the central body, $\mathbf{r}$ the position vector, and $\mathbf{a}_{pert}$ the acceleration due to all perturbing forces acting on the spacecraft. The acceleration vector generally consists of multiple perturbations such as aerodynamic drag, the influence of Earth's non-spherical gravity field, or thrust. These perturbations are further discussed in Section 2.2.4. In general, no analytical solution can be found for Equation (2.10), and numerical methods are required. This is also called the special perturbations method. In contrast, analytical techniques for finding approximate solutions are called general perturbation methods. The most simple special perturbation method is *Cowell's method*, which means direct numerical integration of Equation (2.10). Another approach is the *method of variation of orbital elements*, discussed in the remainder of this section. The specific numerical methods used to solve these problems will be discussed in Section 2.3.

Method of Variation of Orbital Elements

By the method of variation of orbital elements, a set of equations can be derived that describe the variation of each osculating orbital element in terms of a perturbing potential, or perturbing function. This set of first-order differential equations are called *Lagrange's planetary equations*. From these equations, another set of differential equations can be derived, describing the variation of the orbital elements in terms of perturbing accelerations: *Gauss' form of Lagrange's planetary equations*. The six differential equations for the classical Keplerian elements are given by Equation (2.11), the derivation of which can be found in numerous astrodynamics textbooks. The form stated here can be found in (Wakker, 2015).

$$\frac{\mathrm{d}a}{\mathrm{d}t} = 2\frac{a^2}{\sqrt{\mu p}}\left[a_R\, e\sin\theta + a_S\frac{p}{r}\right] \tag{2.11a}$$

$$\frac{\mathrm{d}e}{\mathrm{d}t} = \sqrt{\frac{p}{\mu}}[a_R\sin\theta + a_S(\cos E + \cos\theta)] \tag{2.11b}$$

$$\frac{\mathrm{d}i}{\mathrm{d}t} = a_W\frac{r}{\sqrt{\mu p}}\cos u \tag{2.11c}$$

$$\frac{\mathrm{d}\omega}{\mathrm{d}t} = -\sqrt{\frac{p}{\mu}}\left[a_W\frac{r}{p}\cot i\sin u + \frac{1}{e}\left\{a_R\cos\theta - a_S\left(1+\frac{r}{p}\right)\sin\theta\right\}\right] \tag{2.11d}$$

$$\frac{\mathrm{d}\Omega}{\mathrm{d}t} = a_W\frac{r}{\sqrt{\mu p}\sin i}\sin u \tag{2.11e}$$

$$\frac{\mathrm{d}M}{\mathrm{d}t} = n - a_R\left[\frac{2r}{\sqrt{\mu a}} - \frac{1-e^2}{e}\sqrt{\frac{a}{\mu}}\cos\theta\right] - a_S\frac{1-e^2}{e}\sqrt{\frac{a}{\mu}}\left(1+\frac{r}{p}\right)\sin\theta \tag{2.11f}$$

where $\mathbf{a} = [a_R, a_S, a_W]^\mathsf{T}$ describe the perturbing accelerations in the R-, S- and W-directions, as previously discussed in Section 2.2.1, and $u = \theta + \omega$ is the argument of latitude. As stated in Section 2.2.2, the classical orbital elements show various singularities, making their use for propagation unattractive in certain cases. The planetary equations can therefore also be derived in terms of the MEE, given by Equations 2.12 (Walker et al.,

1985):

$$\frac{\mathrm{d}p}{\mathrm{d}t} = \sqrt{\frac{p}{\mu}}\frac{2p}{w}a_S \tag{2.12a}$$

$$\frac{\mathrm{d}f}{\mathrm{d}t} = \sqrt{\frac{p}{\mu}}\left\{a_R \sin L + \frac{(w+1)\cos L + f}{w}a_S - \frac{g(h\sin L - k\cos L)}{w}a_W\right\} \tag{2.12b}$$

$$\frac{\mathrm{d}g}{\mathrm{d}t} = \sqrt{\frac{p}{\mu}}\left\{-a_R \cos L + \frac{(w+1)\sin L + g}{w}a_S + \frac{f(h\sin L - k\cos L)}{w}a_W\right\} \tag{2.12c}$$

$$\frac{\mathrm{d}h}{\mathrm{d}t} = \sqrt{\frac{p}{\mu}}\frac{s^2\cos L}{2w}a_W \tag{2.12d}$$

$$\frac{\mathrm{d}k}{\mathrm{d}t} = \sqrt{\frac{p}{\mu}}\frac{s^2\sin L}{2w}a_W \tag{2.12e}$$

$$\frac{\mathrm{d}L}{\mathrm{d}t} = \sqrt{\frac{p}{\mu}}\frac{h\sin L - k\cos L}{w}a_W + \sqrt{\mu p}\left(\frac{w}{p}\right)^2 \tag{2.12f}$$

where w and s^2 are auxiliary variables, defined as:

$$w = \frac{p}{r} = 1 + f\cos L + g\sin L \tag{2.13}$$

$$s^2 = 1 + h^2 + k^2 \tag{2.14}$$

To complete the full set of EOM, the spacecraft mass is also taken into account. From the general equation for the spacecraft mass due to propulsion:

$$\frac{\mathrm{d}m}{\mathrm{d}t} = -\frac{T}{g_0 I_{sp}} \tag{2.15}$$

With thrust T, standard gravity g_0, and specific impulse I_{sp}. The full state vector is therefore:

$$\mathbf{x} = [p, f, g, h, k, L, m]^\mathsf{T} \tag{2.16}$$

2.2.4. Orbital Perturbations

As shown in the previous section, the spacecraft motion is modeled by separately considering the two-body and perturbing effects. This section will discuss how these perturbing accelerations can be modeled to allow their use in the variational EOM. This section will discuss thrust, Earth's non-spherical gravity distribution and aerodynamic drag as the main perturbations under consideration.

Thrust

The effect of thrust on the spacecraft mass m is given by Equation (2.15). In addition, thrust can be considered a perturbing acceleration, $\mathbf{a}_{thrust}$. The thrust acceleration can be obtained from the thrust pitch and yaw angles:

$$\mathbf{a}_{thrust} = \frac{T}{m}[\sin\alpha\cos\beta, \cos\alpha\cos\beta, \sin\beta]^\mathsf{T} \tag{2.17}$$

where m is the spacecraft instantaneous mass and T the thrust. In the RSW-frame, the thrust acceleration vector, $\mathbf{a}_{thrust}$, is defined by the thrust magnitude and the two steering angles α and β, the yaw- and pitch steering angles, respectively, as illustrated in Figure 2.4. Here the yaw steering angle is defined with respect to the S-direction. Note that the yaw-angle can sometimes also be defined w.r.t. the velocity vector, requiring an additional rotation by the flight-path angle γ.

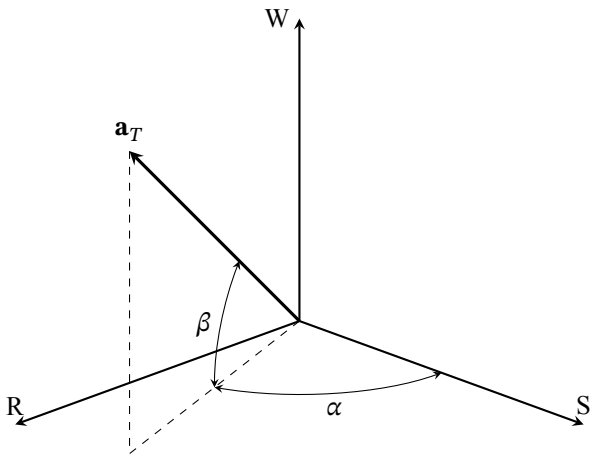

Figure 2.4: yaw- and pitch angles in the RSW-frame

Although thrust T is generally used directly in this work, it can also be described in terms of the engine parameters thruster efficiency η and total propulsion system electrical power P_e:

$$T = \frac{2\eta P_e}{g_0 I_{sp}} \tag{2.18}$$

where g_0 is Earth's standard gravity and I_{sp} the specific impulse. This definition is used to allow comparison with reference material.

Earth's Oblateness

The non-spherical distribution of Earth's gravity field will have a perturbing effect on any orbiting object. This distribution can be described by the gravitational potential (geopotential) U (Wakker, 2015):

$$U = -\frac{\mu}{r}\left[1 - \sum_{n=2}^{\infty} J_n \left(\frac{R_E}{r}\right)^n P_n(\sin\phi) + \sum_{n=2}^{\infty}\sum_{m=1}^{n} J_{n,m}\left(\frac{R_E}{r}\right)^n P_{n,m}(\sin\phi)\left\{\cos m(\Lambda - \Lambda_{n,m}\right\}\right] \tag{2.19}$$

where r, ϕ, Λ are the spherical coordinates relative to the geocentric rotating reference frame. R_E is the mean equatorial radius of the Earth and $J_{n,m}$ and $\Lambda_{n,m}$ are constant model parameters of degree n and order m, respectively. For convenience $J_n \equiv J_{n,0} = -C_{n,0}$. Finally, $P_n(\sin\phi)$ and $P_{n,m}(\sin\phi)$ are Legendre polynomials and their associated Legendre functions. The terms with $m = 0$ are the zonal harmonics, which are independent of longitude. The terms with $n = m$ are the sectoral harmonics, and terms with $m \neq 0$ and $n \neq m$ are tesseral harmonics (Wertz et al., 2011). Figure 2.5 shows a representation of these harmonics. The boundaries between the shaded regions are the locations where the expansion terns change sign.

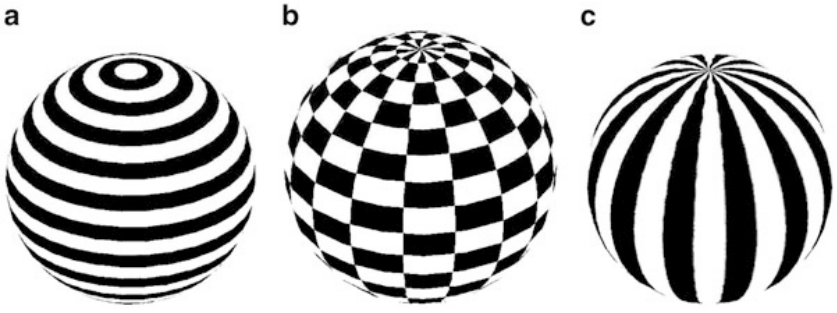

Figure 2.5: Illustration of spherical harmonic expansions, with a) zonal, b) tesseral and c) sectoral terms (Markley and Crassidis, 2014).

The coefficients then scale and hence define the geopotential model of the Earth. As the J_n coefficients correspond with the zonal harmonics, the term corresponding with the J_2 coefficient defines the equatorial bulge, also called

oblateness or flattening. Given that $J_2 = 1.083 \times 10^{-3}$ and the other coefficients are smaller than 2.6×10^{-6}, the term with J_2 dominates the perturbing force (Wakker, 2015), causing a secular drift of the right ascension of the ascending node and the argument of perigee. This effect can be utilized for specialized Earth orbits such as ground-track repeat orbits and sun-synchronous orbits.

When only considering the J_2 term, the perturbing acceleration in terms of MEE and given in the RSW-frame are (Kechichian, 1997):

$$a_R = -\frac{3\mu J_2 R_E^2}{2r^4}\left[1 - 12\frac{(h\sin L - k\cos L)^2}{s^4}\right] \tag{2.20a}$$

$$a_S = -\frac{12\mu J_2 R_E^2}{r^4} \cdot \frac{(h\sin L - k\cos L)(h\cos L + k\sin L)}{s^4} \tag{2.20b}$$

$$a_W = -\frac{6\mu J_2 R_E^2}{r^4} \cdot \frac{(h\sin L - k\cos L)(1 - h^2 - k^2)}{s^4} \tag{2.20c}$$

For a preliminary analysis of the oblateness effect, it can be useful to investigate the effects of this perturbation in terms of Keplerian Elements. The J_2 perturbation has an oscillatory effect on the semi-major axis a, eccentricity e, and inclination i. In contrast, the argument of perigee ω, and right ascension of the ascending node, Ω, will show a secular drift due to the J_2 perturbation. This secular drift is given by Equations (2.21) and (2.22) (Wakker, 2015):

$$\dot{\Omega}_{J_2} = -\frac{3}{2}nJ_2\left(\frac{R_E}{a(1-e^2)}\right)^2 \cos i \tag{2.21}$$

$$\dot{\omega}_{J_2} = \frac{3}{4}nJ_2\left(\frac{R_E}{a(1-e^2)}\right)^2 \left(5\cos^2 i - 1\right) \tag{2.22}$$

where $n = \sqrt{\mu/a^3}$ is the mean motion.

Aerodynamic Drag

The acceleration of a satellite due to aerodynamic drag is given by:

$$\mathbf{a}_{drag} = -C_D\frac{1}{2}\rho\frac{A}{m}|\mathbf{v}|\mathbf{v} \tag{2.23}$$

where ρ is the atmospheric density, $\mathbf{v}$ the velocity vector w.r.t. the (rotating) atmosphere, m the satellite mass, C_D the drag coefficient corresponding to the cross-sectional area A. The ballistic coefficient of the vehicle is defined as $BC = m/(A \cdot C_D)$. Although the vehicle mass and velocity are generally known quantities, determining ρ, A and C_D can present some challenges. Several assumptions will need to be made on the atmospheric model used and the vehicle properties. As a first approximation an exponential atmospheric model can be used as the atmospheric density decreases approximately exponentially with increasing altitude (Wertz et al., 2011):

$$\rho \approx \rho_0 e^{-\Delta h/h_0} \tag{2.24}$$

where ρ and ρ_0 are the densities at two different altitudes, Δh is this altitude difference, and h_0 is the atmosphere scale height. In reality, atmospheric density can vary significantly and the exponential model is generally not sufficient for accurate calculations, and also not for preliminary design. Instead, tabulated values for the mean atmospheric density at certain altitudes can be used, using exponential interpolation to determine the values between these altitudes. Tudat has already provided this functionality with values based on the United States Standard Atmosphere (USSA) 1976 model. The atmospheric density is also largely depending on the solar cycle, with a large difference between solar minimum and maximum. Although the tabulated atmosphere model is considered sufficient for the first-order approach taken, if higher accuracy is required, Tudat also provides an implementation of the empirical NRLMSISE-00 atmosphere model, which is a more accurate atmospheric model that takes into account these environmental effects.

Earth eclipse conditions

The eclipse model implemented in Tudat is based on a conical shadow model, as presented in Section 3.4 of Montenbruck and Gill (2000). This model is used to determine when the position of the spacecraft is in eclipse conditions, i.e. in the shadow region of the Earth, during which no energy can be generated by the solar panels and thus no thrust is produced. This section summarizes the conical shadow model and briefly investigates its implication on the implementation of the propagation.

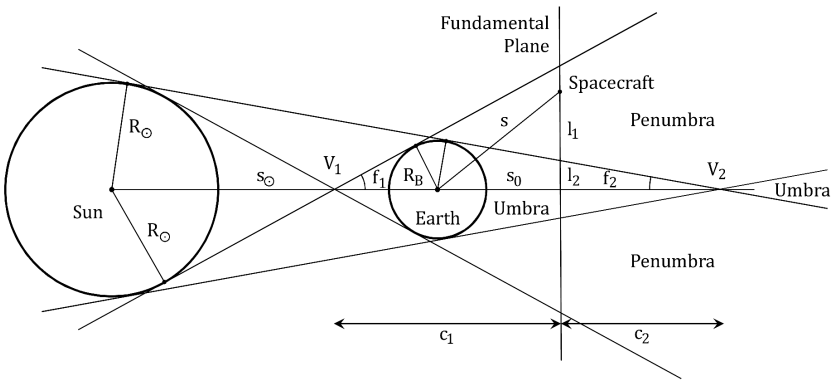

Figure 2.6: Conical shadow model as shown in Montenbruck and Gill (2000).

In the conical shadow model shown in Figure 2.6, the shadow conditions are determined by the position of the spacecraft with respect to the occulting body, i.e. Earth and the occulted body, i.e. the Sun, and their respective radii. When the spacecraft is in the umbra region, the radiation coming from the occulted body is entirely blocked by the occulting body. When in penumbra, the occulted body is only partially blocked. From the position of the orbiting spacecraft, a shadow function, ν, is constructed to quantify the occultation of the Sun, where

$\nu = 0$ when spacecraft is in umbra

$\nu = 1$ when spacecraft is in sunlight

$0 < \nu < 1$ when spacecraft is in penumbra

This is done by using a simple model of two overlapping circular disks, shown in Figure 2.7.

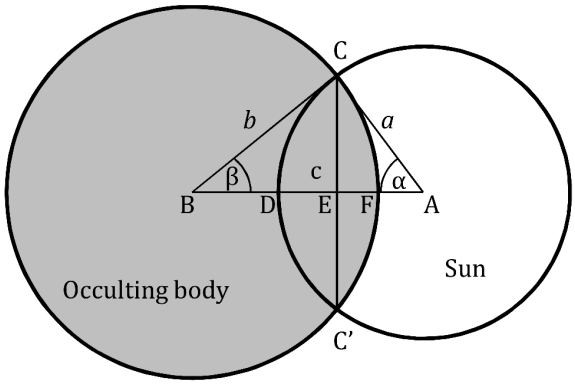

Figure 2.7: Circular overlapping disks, modeling the occultation of the Sun by the Earth from the viewpoint of the orbiting spacecraft (Montenbruck and Gill, 2000).

Given the position of the spacecraft with respect to the occulting body:

$$\mathbf{s} = \mathbf{r} - \mathbf{r}_B \tag{2.25}$$

where $\mathbf{r}$ is the position of the spacecraft and $\mathbf{r}_B$ the position of the occulting body. Together with the radius of the Sun $R_\odot$ and radius of the occulting body R_B, the apparent radii, a of the Sun, and b of the Earth, are given

by

$$a = \arcsin\left(\frac{R_\odot}{|\mathbf{r}_\odot - \mathbf{r}|}\right) \tag{2.26}$$

$$b = \arcsin\left(\frac{R_E}{s}\right) \tag{2.27}$$

and the apparent separation c of the bodies is given by

$$c = \arccos\left(\frac{-\mathbf{s}^\mathsf{T}(\mathbf{r}_\odot - \mathbf{r})}{s\left\|\mathbf{r}_\odot - \mathbf{r}\right\|}\right) \tag{2.28}$$

Under the condition

$$|a - b| < c < a + b \tag{2.29}$$

and the definitions $x \equiv \overline{AE}$, $y \equiv \overline{EC}$, and $\alpha \equiv \angle CAE$, the occulted area A is given by

$$\begin{aligned} A &= 2(A_{BCF} - A_{BCE}) + 2(A_{ACD} - A_{ACE}) \\ &= a^2 \arccos\frac{x}{a} + b^2 \arccos\frac{c - x}{b} - cy \end{aligned} \tag{2.30}$$

where

$$x = \frac{c^2 + a^2 - b^2}{2c} \tag{2.31}$$

$$y = \sqrt{a^2 - x^2} \tag{2.32}$$

Finally, the fraction of sunlight is given by the shadow function ν:

$$\nu = 1 - \frac{A}{\pi a^2} \tag{2.33}$$

When the condition Equation (2.29) does not hold, either no occultation, total occultation, or partial occultation takes place. An overview of these conditions is given in Table 2.2.

Table 2.2: Occulting conditions based on the apparent radii a, b and apparent distance c, between the occulted and occulting body, respectively.

Condition	Occultation
$a + b \leq c$	No
$c < b - a$, implying $a < b$	Total
$c < a - b$, implying $a > b$	Partial

Boudestijn (2014) and Gómez-Jenkins (2015) simplified the influence of eclipse conditions by setting thrust levels to zero only when in total occultation. In contrast, Jimenez-Lluva (2017) used a minimum light percentage threshold of 80% to determine when to switch thrust on. In this work, the simplified approach is taken as this vastly simplifies the implementation and is considered sufficient for preliminary analysis as is the goal of this project. Furthermore, the position of the Sun with respect to the Earth needs to be known at each propagation epoch. In Tudat these are directly available through a connection to the information system, SPICE. This toolkit provided by NASA's Navigation and Ancillary Information Facility (NAIF) at Jet Propulsion Laboratory (JPL) containing navigation and other data, including ephemerides of planetary bodies (Acton, 1996), and is used for this purpose.

Other perturbations

In addition to the perturbations discussed in this section, there are several other perturbing effects that are not taken into account but can be relevant for certain cases. These are the gravitational effect of thirst bodies, most notably solar and lunar attraction, solar radiation pressure, and electromagnetic forces. For an in-depth discussion on third body effects, Gómez-Jenkins (2015) provides an analysis and derivation of their average contribution. Solar radiation pressure can become relevant for spacecraft orbiting at higher altitudes or for spacecraft using solar radiation as their primary means of propulsion, i.e. solar sailing. Perturbations due to Earth's magnetic field are generally extremely small (Wakker, 2015).

2.3. Propagation

Propagation deals with solving the Initial Value Problem (IVP), given a set of initial conditions and a set of differential equations, i.e. the EOM, find its evolution over time. For the OT this means propagating the spacecraft trajectory forwards in time, given an initial state. In the context of this project, numerical methods for solving ordinary differential equations are referred to as numerical integration methods, or integrators. Three different propagation methods (propagators) are used in the project and are briefly summarized in Table 2.3:

Table 2.3: Summary of propagation methods used in this project.

method	propagator	integrator	description
benchmark	Cowell	RKF7(8)	Generates high-accuracy reference trajectories using small step-sizes in the order of several seconds.
CI	Gauss MEE	RK4	Uses the Gaussian' form of Lagrange's Planetary equations to propagate with a fixed step-size in eccentric anomaly, E, as opposed to time.
OA	Gauss MEE	RKF4(5)	Uses average state derivatives, obtained by 'embedded' CI, to propagate forward in time with large step sizes in the order of days.

The benchmark propagator is used to allow verification of the OT and will be further explained in Chapter 3. The CI and OA approaches are the main subject of this section. Section 2.3.1 will first introduce the numerical integration methods used. Subsequently, Section 2.3.2 describes the CI and OA methods.

2.3.1. Numerical Integration

Formally numerical integration deals with solving the IVP:

$$\dot{\mathbf{x}} = \mathbf{f}(\mathbf{x}, t) \quad ; \quad \mathbf{x}(t_0) = \mathbf{x}_0 \tag{2.34}$$

This section will summarize the relevant integration techniques used for this project. This is based on a previously performed literature survey. For a more in-depth discussion on numerical methods, the reader is referred to existing literature such as the book by Burden and Faires (2011). Although a fixed-step integrator such as fourth-order Runge-Kutta (RK4) was considered sufficient for preliminary optimization based on the literature survey, variable step-size integration schemes such as Runge-Kutta Fehlberg (RKF) will also be discussed as their use can yield a major advantage in specific cases, especially when considering the OA propagation.

One of the most well-known multi-stage (i.e. using multiple function evaluations per time-step) methods, is the

fourth-order method, RK4:

$$\mathbf{k}_1 = \mathbf{f}(\mathbf{x}, t) \tag{2.35a}$$

$$\mathbf{k}_2 = \mathbf{f}\left(\mathbf{x} + \frac{1}{2}\mathbf{k}_1, t + \frac{1}{2}h\right) \tag{2.35b}$$

$$\mathbf{k}_3 = \mathbf{f}\left(\mathbf{x} + \frac{1}{2}\mathbf{k}_2, t + \frac{1}{2}h\right) \tag{2.35c}$$

$$\mathbf{k}_4 = \mathbf{f}(\mathbf{x} + \mathbf{k}_3, t + h) \tag{2.35d}$$

$$\mathbf{x}(t + h) = \mathbf{x} + h\frac{1}{6}(\mathbf{k}_1 + 2\mathbf{k}_2 + 2\mathbf{k}_3 + \mathbf{k}_4) \tag{2.35e}$$

where h is the (fixed) step size. Other orders of (explicit) Runge-Kutta methods are easily constructed but are still limited by their fixed step-size, h. These methods perform poorly when the dynamics change significantly over the integration time. Variable step-size or adaptive integration schemes vary the size of h based on the changing dynamics. For example, in an elliptical orbit, the dynamics can change orders of magnitude faster at periapsis than during apoapsis.

RKF is a common adaptive step-size integrator. It uses an embedded Runge-Kutta integrator to first estimate a local truncation error which is then used to determine an appropriate step size that reduces the error to be within a certain threshold. A common implementation uses a fifth-order integrator to estimate the local error of a fourth-order integrator, i.e. RKF4(5). These are chosen such that their coefficients overlap, i.e. embedded. Therefore only one extra function evaluation is needed to estimate the error. For a general Runge-Kutta method:

$$\mathbf{x}(t + h) = \mathbf{x}_0 + \sum_{i=1}^{N} c_i \mathbf{k}_i \tag{2.36}$$

note that generally the order of the method p, is not equal to the number of stages N. In general $p < N$ except for $N < 5$. For equal evaluations $\mathbf{k}_i$ we can construct a second method (of order $p - 1$):

$$\mathbf{x}^*(t + h) = \mathbf{x}_0 + \sum_{i=1}^{N-1} c_i^* \mathbf{k}_i \tag{2.37}$$

While the coefficients c_i and c_i^* are different, the function evaluations k_i are the same, therefore the number of function evaluations required is significantly lower when compared to two arbitrary methods of a different order. The error is then estimated:

$$\epsilon \approx \mathbf{x}^*(t + h) - \mathbf{x}(t + h) \tag{2.38}$$

From this error, a new time step is determined when the estimated error is higher than some threshold. In practice, tolerances are used to ensure some minimal sufficient step size. After the new step size is determined both the higher- and lower-order method can be used to perform the propagation. In practice, both approaches are used.

In contrast to single-step integration schemes, multi-step integrators such as Adams-Bashford also make use of previous function evaluations to compute future steps.

$$\mathbf{x}(t_{n+1}) = \mathbf{x}(t_n) + h \sum_{j=0}^{s} b_j \mathbf{f}\big(t_{n-j}, \mathbf{x}_{n-j}\big) \tag{2.39}$$

This uses s evaluations for every time step. This means the computational resources are more efficiently used and allows easier interpolation between steps. However, varying the time-step is not as straightforward as for single-step methods. Furthermore, some initialization is required. The above method is an explicit method; implicit approaches such as Adams-Moulton require the next step to be solved indirectly using a predictor-corrector approach.

Kluever (2010) and Boudestijn (2014) limited themselves to using a fixed-step Heun integrator which produced adequate results. Further testing by Gómez-Jenkins (2015) showed that the use of RKF variable step integration reduces the number of function evaluations while maintaining similar accuracy. Jimenez-Lluva (2017) uses RK4 integration for his CI implementation but does not explicitly state the method by which OA is propagated.

2.3.2. State Propagation

In this section, three methods of propagation were introduced: Cowell propagation, which will be used to generate benchmark trajectories, CI, and OA. The first will be further discussed in Chapter 3, the latter two will be described in the remainder of this section. The EOM obtained from Gauss' form of Lagrange's planetary equations in terms of MEE, can be numerically integrated using any method introduced in the previous section. In addition, the independent parameter is changed from time t, to eccentric anomaly E, to ensure a good spread of integration points over a single revolution. This approach of 'continuously integrating' the EOM is called CI. However, this will require integration of a large number of steps per orbit for a large number of revolutions. For trajectories in the order of tens of days, this can quickly become computationally expensive. Instead, two properties of low-thrust many-revolution transfer trajectories can be exploited. Firstly, five of the six orbital elements generally change slowly for low-thrust propulsion trajectories. Secondly, the change in orbital elements from one revolution to the next is small.

The OA method uses these properties by sacrificing accuracy in the fast-changing parameter, true anomaly θ, to greatly reduce the number of function evaluations required. The remainder of the section will describe the OA methodology in more detail. The OA methodology used in this project, as based on the work in Jimenez-Lluva (2017), uses an 'embedded' CI propagation, that propagates the trajectory for a single revolution to find the average state progression over this orbital revolution.

Continuous Integration

CI propagates the state in MEE from t_0 to t_f, using n_k steps per revolution with a fixed size in eccentric anomaly $\Delta E = 2\pi/n_k$. This change in independent parameters was done firstly, to allow re-use of the propagation logic 'embedded' in the OA approach and secondly, to ensure a good spread of integration points over a single revolution when compared to the use of time as independent parameter. This is especially important for eccentric trajectories, such as GTO. At each integration step, the time-step is calculated through:

$$\Delta E = \frac{2\pi}{n_k} \tag{2.40}$$

$$\Delta t = \Delta E \frac{\mathrm{d}t}{\mathrm{d}E} \tag{2.41}$$

Given the variational equation of the eccentric anomaly $\mathrm{d}E/\mathrm{d}t$ (Gao and Kluever, 2005):

$$\frac{\mathrm{d}E}{\mathrm{d}t} = \frac{na}{r} + \frac{1}{nae}\left[a_R(\cos\theta - e) - a_S\left(1 + \frac{r}{a}\right)\sin\theta\right] \tag{2.42}$$

where mean motion $n = \sqrt{\mu/a^3}$. When assuming that a_R and a_S are significantly smaller than the gravitational acceleration, $\mathrm{d}E/\mathrm{d}t$ can be approximated by

$$\frac{\mathrm{d}E}{\mathrm{d}t} \approx \frac{na}{r} \tag{2.43}$$

where r is the magnitude of the radius vector and follows from Equation (2.13):

$$r = \frac{p}{1 + f\cos L + g\sin L} \tag{2.44}$$

The approximation in Equation (2.43) was shown by Boudestijn (2014) and Gómez-Jenkins (2015) to be sufficiently accurate for the purpose of OA. This is immediately apparent for eccentric orbits, where the term $1/nae$ in combination with small perturbing accelerations results in a very small second term. For near-circular orbits, the first term is approximately n. The term $1/nae$ is of course no longer small for $e \to 0$, but this effect is nevertheless still canceled out for low perturbing accelerations. As shown by Gao and Kluever (2005), for $e = 0.001$ and $a = 1.05 \cdot R_E$, i.e. a near-circular LEO, and a perturbing acceleration of $a = 10^{-5}$ m s^{-1}, the second term is about two orders of magnitude smaller.

Note that Jimenez-Lluva uses the true anomaly θ to determine Δt: $\Delta t = \Delta\theta \mathrm{d}t/\mathrm{d}\theta$, and the approximation:

$$\frac{\mathrm{d}\theta}{\mathrm{d}t} \approx \frac{na}{r} \tag{2.45}$$

However, the author suspects this has been in error, as the approximation for $\mathrm{d}E/\mathrm{d}t$, as given by Equation (2.43), was shown to be valid for the eccentric anomaly E (Kluever, 2010). An approximation for $\mathrm{d}\theta/\mathrm{d}t$ would instead follow from Equation (2.46) (Vallado and McClain, 2001, p. 566).

$$\frac{\mathrm{d}\theta}{\mathrm{d}t} = \frac{H}{r^2} + \frac{\sqrt{1-e^2}}{nae}\left[a_R \cos\theta - a_S \frac{2 + e\cos\theta}{1 + e\cos\theta}\right] \tag{2.46}$$

where $H = \sqrt{\mu p}$ is the specific orbital angular momentum.

Furthermore, using the eccentric anomaly as opposed to the true anomaly to distribute the integration segments over the full trajectory ensures a denser distribution near perigee, where the dynamics change more significantly for eccentric orbits, which was the reasoning used by Jimenez-Lluva for using equidistant steps in θ. Nevertheless, because na/r is used to determine the time-step, the actual implementation is the same, thus still allowing comparison of results for verification purposes.

Orbital Averaging

OA was initially proposed by Gao and Kluever (2005) as an analytical approach as a means to drastically decrease the number of evaluations required to propagate the spacecraft state using a low-thrust propulsion system, for many-revolution planetocentric trajectories. OA achieves this by using the average progression of the orbital elements for a single revolution to propagate the full trajectory over a larger time span.

When considering the classical orbital elements $\mathbf{oe} = [a, e, i, \omega, \Omega, \theta]^\mathsf{T}$ these change slowly and gradually over the course of a single revolution, with the exception of θ. This highlights the main disadvantage of OA: Loss of accuracy for the fast-changing element. The same holds when considering MEE: All elements change slowly and gradually, with the exception of the true longitude L. When only the target orbit is of importance, and the exact location in this orbit can be disregarded, OA is an attractive option to significantly decrease the computational load.

The implementation of OA uses the existing propagation logic, i.e. CI to propagate the state over a single revolution. A similar approach is implemented as stated by Jimenez-Lluva (2017) and summarized in this section. To ensure the secular changes are accurately taken into account the orbit is fully propagated for exactly a single revolution. This is done by changing the independent variable to the eccentric anomaly, E and subsequently propagating from $E = 0$ to $E = 2\pi$, using n_k equidistant steps in E.

Propagating for a single revolution yields n_k values for $\dot{\mathbf{x}}$. These are subsequently numerically averaged to obtain $\bar{\dot{\mathbf{x}}}$ following the expression in Equation 2.47.

$$\bar{\dot{\mathbf{x}}} = \frac{\Delta \mathbf{x}}{T_p} = \frac{1}{T_p}\int_{t_0}^{t_{2\pi}} \frac{\mathrm{d}\mathbf{x}}{\mathrm{d}t}\mathrm{d}t = \frac{1}{T_p}\int_{0}^{2\pi} \frac{\mathrm{d}\mathbf{x}}{\mathrm{d}t}\frac{\mathrm{d}t}{\mathrm{d}E}\mathrm{d}E \tag{2.47}$$

where T_p is the orbital period. The orbital period results directly from the integration to $E = 2\pi$ and is simply taken as $t_{2\pi} - t_0$. This is in contrast to the original method where the orbital period is approximated through $T_p = 2\pi\sqrt{a^3/\mu}$.

The original method by Kluever (2010) uses the shadow exit and entry angle E_{ex} and E_{en} as integration bounds to account for the loss of thrust during eclipse conditions:

$$\bar{\dot{\mathbf{x}}} = \frac{1}{T_p}\int_{E_{ex}}^{E_{en}} \frac{\mathrm{d}\mathbf{x}}{\mathrm{d}t}\frac{\mathrm{d}t}{\mathrm{d}E}\mathrm{d}t \tag{2.48}$$

However, as other perturbations such as aerodynamic drag or the effect of spherical harmonics are still present during this period, the full revolution will be taken into account. When eclipse conditions need to be taken into account, the shadow function Equation (2.33) is used to determine thrust levels during propagation.

The integral $\Delta\mathbf{x}$ in Equation (2.47) is approximated using a trapezoidal scheme, Equation 2.49

$$\Delta\mathbf{x}_{trap} \approx \sum_{i=0}^{n_k-1}\left(\frac{\left[\frac{\mathrm{d}\mathbf{x}}{\mathrm{d}t}\frac{\mathrm{d}t}{\mathrm{d}E}\right]_{E=E_i}+\left[\frac{\mathrm{d}\mathbf{x}}{\mathrm{d}t}\frac{\mathrm{d}t}{\mathrm{d}E}\right]_{E=E_{i+1}}}{2}\Delta E\right) \tag{2.49}$$

with $E_{i+1} = E_i + \Delta E$.

At this point, an important observation is made. When using a fully numerical approach to determine the average state derivative $\dot{\mathbf{x}}$, i.e. using CI to propagate the full state, including perturbations for a single revolution, the use of a numerical quadrature to approximate $\Delta\mathbf{x}$ is not strictly necessary. After all, $\Delta\mathbf{x}$ follows directly from the difference between the initial and final state (in MEE). There are several reasons why this additional step is nevertheless maintained. Firstly, the method is based on the implementation by the previous author Jimenez-Lluva (2017), who uses a fully numerical approach as well as the quadrature approximation. Only at a later stage it was determined that this step was redundant. Secondly, for sufficiently large n_k, the result obtained for $\Delta\mathbf{x}$ will not be significantly different, making the result still valid, but more computationally intensive than required. Finally, this approximation is only redundant in this specific case.

Another method by which the average state derivatives can be obtained is by not propagating the full state, but by assuming each orbital element is constant over a single revolution and using the approximation $T_p = 2\pi\sqrt{a^3/\mu}$. Then the state derivatives are obtained by evaluating the EOM at n_k points, spread equidistantly through the eccentric anomaly E or true longitude L. Furthermore, when averaged expressions for perturbations can be found analytically, such as for Earth gravitational potential or third body perturbations, these can be simply added to the average state derivative and are not part of the trapezoidal quadrature. Nonetheless, independent of the means by which average state derivatives are obtained in Equation (2.47), these can be numerically integrated using a significantly larger step-size than used in the CI approach.

Using a lower-order method such as Euler, for example as used by Jimenez-Lluva (2017), will quickly lead to under- or overestimation and is generally not accurate enough. Using a higher-order method would quickly diminish the advantage of OA in terms of computational speed. Boudestijn (2014) also found the accuracy of a second-order technique to be sufficient for OA. Furthermore, Heun's method was also used by Kluever (2010) in the initial proposal. However, for many trajectories, the 'best' arc length varies over the course of the trajectory while maintaining similar accuracy. For example, when considering a LEO-to-GEO transfer trajectory, the orbital period will vary from about 90 minutes to 24 hours. In the later parts of the transfer a larger OA step size can be used, ultimately to significantly reduce computation times. Therefore, the variable step-size integrator RKF was selected, as was also recommended by (Gómez-Jenkins, 2015).

2.4. Optimization

This section aims to discuss and explain all techniques that are directly relevant to the optimization process. This encompasses the optimal control theory used to obtain the control parametrization. Co-state linearization is used to construct a design vector, greatly reducing the number of parameters left. Following this, the objective function that is to be optimized is explained. Finally, the optimizer itself is discussed. The method selected to optimize the low-thrust trajectories is a direct method that uses control parametrization to derive control laws for the optimal thrust angles and magnitudes. Although this is a direct method, it relies on optimal control theory to parametrize the OCP. This section briefly introduces the necessary background in optimal control and the way in which the control is parameterized to allow the direct approach. Lastly, the optimization algorithm, SaDE, is introduced, together with the Aggregate Objective Function (AOF).

2.4.1. Optimal Control

Optimal control deals with the problem of finding expressions for the control inputs that minimize a certain objective function. In this case, the specific objective is to find expressions for the optimal thrust steering angles α^* and β^* and thrust level T^*. This section aims to summarize the required background, an introduction of control parametrization. For a more comprehensive overview of optimal control theory, the reader is referred to more extensive literature, such as existing books on the subject (Longuski et al., 2014; Visser, 2014).

In general, the OCP consists of the state $\mathbf{x}(t)$, control inputs $\mathbf{u}(t)$ and the system of differential equations:

$$\dot{\mathbf{x}}(t) = f[\mathbf{x}(t), \mathbf{u}(t), t] \tag{2.50}$$

The objective function is defined as

$$\min_{\mathbf{u}(t)} J = \Phi\big[\mathbf{x}(t_f), t_f\big] + \int_{t_0}^{t_f} \mathcal{F}[\mathbf{x}(t), \mathbf{u}(t), t]\mathrm{d}t \tag{2.51}$$

where Φ and $\mathcal{F}$ are the Mayer and Lagrange terms, representing the final and integral cost, respectively, and $\mathbf{u}(t)^\mathsf{T} = [\alpha, \beta, T]$ is the control vector. Following Pontryagain's Minimum Principle, the optimal conditions that give the optimum of the corresponding TPBVP are those minimizing the Hamiltonian equations (Pontryagin, 1987):

$$\mathcal{H} = \mathcal{F} + \boldsymbol{\lambda}^\mathsf{T} \cdot \dot{\mathbf{x}} \tag{2.52}$$

where $\boldsymbol{\lambda}$ is the co-states vector, or sometimes referred to as the Lagrange multipliers corresponding to the state equations:

$$\boldsymbol{\lambda} = \big[\lambda_p, \lambda_f, \lambda_g, \lambda_h, \lambda_k, \lambda_m\big]^\mathsf{T} \tag{2.53}$$

These co-states correspond to each equinoctial element, with the exception of the fast-changing true longitude, and the spacecraft mass m. The true longitude is excluded as it will become obsolete through the use of OA, as was discussed in Section 2.3.2.

The co-states vector $\boldsymbol{\lambda}(t)$ can be interpreted as representing the relative importance of each state parameter as a function of time. The necessary optimality conditions state that the first-order derivative of the Hamiltonian with respect to the control variables has to be zero, i.e. the Karush-Kuhn-Tucher conditions as shown in Equation (2.54). Furthermore, the second-order derivative has to be positive definite, the Legendre-Clebsch condition as stated in Equation (2.55).

$$\frac{\partial \mathcal{H}}{\partial \mathbf{u}} = 0 \tag{2.54}$$

$$\frac{\partial^2 \mathcal{H}}{\partial \mathbf{u}^2} > 0 \tag{2.55}$$

With these conditions, expressions for the optimal thrust steering angles and thrust magnitudes can be obtained, as a function of the co-state equations. To complete the modeling of the TPBVP these equations are not sufficient for optimality, this requires deriving the co-states equations given in Equation (2.56) for each co-state.

$$\frac{\mathrm{d}\boldsymbol{\lambda}}{\mathrm{d}t} = -\frac{\partial \mathcal{H}}{\partial \mathbf{x}} \tag{2.56}$$

Solving Equation (2.56) for each co-state leads to a system of equations for the optimal co-states, $\boldsymbol{\lambda}(t)$, only as a function of a set of initial co-states, $\boldsymbol{\lambda}_0$. This is the approach taken by indirect methods, using the co-state equations to determine $\boldsymbol{\lambda}(t)$. However, having to re-derive Equation (2.56) for every addition to the problem, such as different perturbations, limits its general applicability. Furthermore, by parametrizing the thrust control input, the dimensionality of the problem is reduced (Kluever, 2010). In contrast, this work will focus on how the optimality conditions can be used to derive expressions for the optimal thrust, without having to derive Equation (2.56), as this condition hinders the general applicability. This method of parametrizing the control input is outlined in Section 2.4.2.

2.4.2. Control Parametrization

In contrast to indirect methods, the goal is to circumvent the requirement of the full derivation of all optimality conditions. Instead, only the derivatives with respect to the control inputs are used to derive expressions for the optimal control inputs α^*, β^* and T^*. The work by Kluever (2010) used the following Hamiltonian to derive the optimal thrust-steering control laws:

$$\mathcal{H} = \lambda_a \frac{\mathrm{d}a}{\mathrm{d}t} + \lambda_e \frac{\mathrm{d}e}{\mathrm{d}t} + \lambda_i \frac{\mathrm{d}i}{\mathrm{d}t} \tag{2.57}$$

limiting themselves to only the first three Keplerian elements. Boudestijn (2014) and later Gómez-Jenkins (2015) expanded this approach by deriving the equations for MEE. Finally, Jimenez-Lluva and Root (2020) expanded the derivation with the addition of the spacecraft mass co-state, to allow for a coasting arc mechanism and dropping the continuous thrust assumption. This is the method used here and thus using the following Hamiltonian (Jimenez-Lluva, 2017):

$$\mathcal{H} = \lambda_p \frac{\mathrm{d}p}{\mathrm{d}t} + \lambda_f \frac{\mathrm{d}f}{\mathrm{d}t} + \lambda_g \frac{\mathrm{d}g}{\mathrm{d}t} + \lambda_h \frac{\mathrm{d}h}{\mathrm{d}t} + \lambda_k \frac{\mathrm{d}k}{\mathrm{d}t} + \lambda_m \frac{\mathrm{d}m}{\mathrm{d}t} \tag{2.58}$$

Note that the fast-changing true longitude, L, is discarded as it will disappear by using OA. By applying the first-order necessary conditions Equation (2.54) to the Hamiltonian Equation (2.58) with respect to α and β, the optimal steering angles α^* and β^*can be found. Applying the first condition, i.e. $\partial\mathcal{H}/\partial\alpha = 0$ and $\partial\mathcal{H}/\partial\beta = 0$ results in

$$\tan\alpha^* = \frac{\Lambda^{\alpha}_{f,1} - \Lambda^{\alpha}_{\mathrm{g},1}}{\Lambda^{\alpha}_{p} + \Lambda^{\alpha}_{f,2} + \Lambda^{\alpha}_{\mathrm{g},2}} \tag{2.59}$$

$$\tan\beta^* = \frac{\Lambda^{\beta}_{f,3} + \Lambda^{\beta}_{\mathrm{g},3} + \Lambda^{\beta}_{h} + \Lambda^{\beta}_{k}}{\Lambda^{\beta}_{p} + \Lambda^{\beta}_{f,1} + \Lambda^{\beta}_{f,2} - \Lambda^{\beta}_{\mathrm{g},1} + \Lambda^{\beta}_{\mathrm{g},2}} \tag{2.60}$$

where Λ^{q}_{α} and Λ^{q}_{β} represent the constants in the partial derivatives of the Hamiltonian $\mathcal{H}$ with respect to the thrust steering angles α and β, corresponding to the q^{th} element in the state vector $\mathbf{x}$ and are given by Equations (2.61) to (2.74):

$$\Lambda^{\alpha}_{p} = \lambda_p \sqrt{\frac{p}{\mu}} \frac{2p}{w} \cos\beta \tag{2.61}$$

$$\Lambda^{\alpha}_{f,1} = \lambda_f \sqrt{\frac{p}{\mu}} \cos\beta \sin L \tag{2.62}$$

$$\Lambda^{\alpha}_{\mathrm{g},1} = \lambda_g \sqrt{\frac{p}{\mu}} \cos\beta \cos L \tag{2.63}$$

$$\Lambda^{\alpha}_{f,2} = \lambda_f \sqrt{\frac{p}{\mu}} \frac{[(w+1)\cos L + f]\cos\beta}{w} \tag{2.64}$$

$$\Lambda^{\alpha}_{\mathrm{g},2} = \lambda_g \sqrt{\frac{p}{\mu}} \frac{[(w+1)\sin L + g]\cos\beta}{w} \tag{2.65}$$

where the common terms $\sqrt{p/\mu}$ and $\cos\beta$ will cancel out. The partial derivatives with respect to β are:

$$\Lambda_p^\beta = \lambda_p \sqrt{\frac{p}{\mu}} \frac{2p}{w} \cos\alpha^* \tag{2.66}$$

$$\Lambda_{f,1}^\beta = \lambda_f \sqrt{\frac{p}{\mu}} \sin L \sin\alpha^* \tag{2.67}$$

$$\Lambda_{g,1}^\beta = \lambda_g \sqrt{\frac{p}{\mu}} \cos L \sin\alpha^* \tag{2.68}$$

$$\Lambda_{f,2}^\beta = \lambda_f \sqrt{\frac{p}{\mu}} [(w+1)\cos L + f] \cos\alpha^* \tag{2.69}$$

$$\Lambda_{g,2}^\beta = \lambda_g \sqrt{\frac{p}{\mu}} [(w+1)\sin L + g] \cos\alpha^* \tag{2.70}$$

$$\Lambda_{f,3}^\beta = \lambda_f \sqrt{\frac{p}{\mu}} \frac{g}{w} (h\sin L - k\cos L) \tag{2.71}$$

$$\Lambda_{g,3}^\beta = \lambda_g \sqrt{\frac{p}{\mu}} \frac{f}{w} (h\sin L - k\cos L) \tag{2.72}$$

$$\Lambda_h^\beta = \lambda_h \sqrt{\frac{p}{\mu}} \frac{s^2 \cos L}{2w} \tag{2.73}$$

$$\Lambda_k^\beta = \lambda_k \sqrt{\frac{p}{\mu}} \frac{s^2 \sin L}{2w} \tag{2.74}$$

where $w = 1 + f\cos L + g\sin L$, and $s^2 = 1 + h^2 + k^2$. By using the second necessary condition Equation (2.55) and some trigonometric manipulation, the sine and cosine of the optimal steering angle α^* and their proper signs can be found:

$$\sin\alpha^* = \frac{-\left(\Lambda_{f,1}^\alpha - \Lambda_{g,1}^\alpha\right)}{\sqrt{\left(\Lambda_{f,1}^\alpha - \Lambda_{g,1}^\alpha\right)^2 + \left(\Lambda_p^\alpha + \Lambda_{f,2}^\alpha + \Lambda_{g,2}^\alpha\right)^2}} \tag{2.75}$$

$$\cos\alpha^* = \frac{-\left(\Lambda_p^\alpha + \Lambda_{f,2}^\alpha + \Lambda_{g,2}^\alpha\right)}{\sqrt{\left(\Lambda_{f,1}^\alpha - \Lambda_{g,1}^\alpha\right)^2 + \left(\Lambda_p^\alpha + \Lambda_{f,2}^\alpha + \Lambda_{g,2}^\alpha\right)^2}} \tag{2.76}$$

The sine and cosine of the optimal steering angle β^* and proper signs are similarly found:

$$\sin\beta^* = \frac{-\left(-\Lambda_{f,3}^\beta + \Lambda_{g,3}^\beta + \Lambda_h^\beta + \Lambda_k^\beta\right)}{\sqrt{\left(-\Lambda_{f,3}^\beta + \Lambda_{g,3}^\beta + \Lambda_h^\beta + \Lambda_k^\beta\right)^2 + \left(\Lambda_p^\beta + \Lambda_{f,1}^\beta - \Lambda_{g,1}^\beta + \Lambda_{f,2}^\beta + \Lambda_{g,2}^\beta\right)^2}} \tag{2.77}$$

$$\cos\beta^* = \frac{-\left(\Lambda_p^\beta + \Lambda_{f,1}^\beta - \Lambda_{g,1}^\beta + \Lambda_{f,2}^\beta + \Lambda_{g,2}^\beta\right)}{\sqrt{\left(-\Lambda_{f,3}^\beta + \Lambda_{g,3}^\beta + \Lambda_h^\beta + \Lambda_k^\beta\right)^2 + \left(\Lambda_p^\beta + \Lambda_{f,1}^\beta - \Lambda_{g,1}^\beta + \Lambda_{f,2}^\beta + \Lambda_{g,2}^\beta\right)^2}} \tag{2.78}$$

The control laws thus far are equal to those derived in (Boudestijn, 2014). However, with the addition of the mass co-state, the constant thrust assumption can be dropped and an optimal control law for thrust T can be derived. This approach is based on the work in Gao and Kluever (2004) but then re-derived for MEE in Jimenez-Lluva

(2017). By evaluating the Hamiltonian derivative with respect to thrust T:

$$\begin{aligned}\frac{\partial \mathcal{H}}{\partial T} &= \Lambda_p^\beta \cos\beta \frac{1}{m} \\ &+ \left[\Lambda_{f,1}^\beta \cos\beta + \Lambda_{f,2}^\beta \cos\beta - \Lambda_{f,3}^\beta \sin\beta\right]\frac{1}{m} \\ &+ \left[-\Lambda_{g,1}^\beta \cos\beta + \Lambda_{g,2}^\beta \cos\beta + \Lambda_{g,3}^\beta \sin\beta\right]\frac{1}{m} \\ &+ \Lambda_h^\beta \sin\beta \frac{1}{m} + \Lambda_k^\beta \sin\beta \frac{1}{m} - \lambda_m \frac{1}{g_0 I_{sp}} = S_t\end{aligned} \tag{2.79}$$

As the Hamiltonian is linear in thrust T (see Equation (2.15)), this results in a switching function $S_t = \partial\mathcal{H}/\partial T$ and thus bang-bang control:

$$T^* = \begin{cases} 0, & \text{if } S_t > 0 \\ T_{max}, & \text{if } S_t < 0 \end{cases} \tag{2.80}$$

Note that a third condition where $S_t = 0$ and $\dot{S}_t = 0$, causing a potential thrust between 0 and T_{max} is neglected. Firstly, the numerical nature of the propagation means this condition is rarely reached. Furthermore, these singular arcs have a small duration in practice (Jimenez-Lluva, 2017).

In summary, the optimal thrust steering angles α^*, β^* and T^* are given by Equations (2.75) to (2.78) and the optimal thrust bang-bang control T^* from Equation (2.80). Note that the computation of the actual thrust steering angle is generally not required as the sine and cosine terms can be directly substituted in Equation (2.17) to obtain the thrust acceleration vector $\mathbf{a}_T$.

2.4.3. Co-state Linearization

We now have derived expressions for the optimal thrust steering angles, $\mathbf{u}^*(t)$, as a function of the individual co-states $\boldsymbol{\lambda}$, current state $\mathbf{x}$, and time t. So, given a time history of co-states, the optimal control parameters can be determined and subsequently the full EOM propagated. To achieve this the co-states can be set at fixed points, or nodes, and interpolated between them. This parametrization of the control parameters can be done among an arbitrary number of n nodes, spaced along the semi-major axis (Kluever, 2010) or in time (Gómez-Jenkins, 2015). An example of this is shown in Figure 2.8.

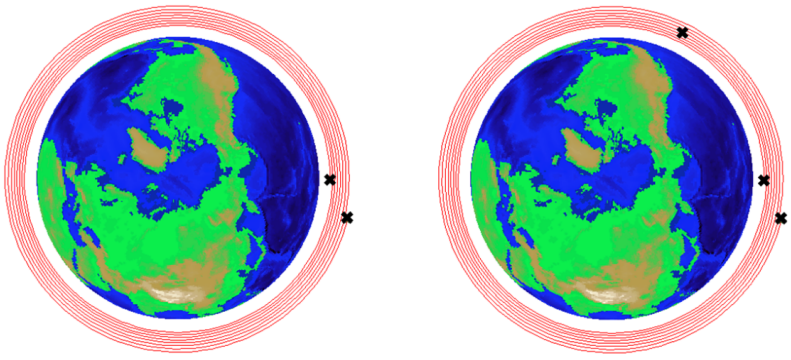

Figure 2.8: Example of two (left) or three (right) nodes, equally distributed in semi-major-axis (Gómez-Jenkins, 2015).

Gómez-Jenkins (2015) shows that using more than two nodes increases the solution accuracy slightly but at the cost of a significant increase in computational effort. This is supported by Kluever (2010) who also argues that the performance gain is relatively small when compared to the computation cost. Therefore in this work, only a single co-state arc will be considered, i.e. from initial co-states $\boldsymbol{\lambda}_0$ to final co-states $\boldsymbol{\lambda}_f$. Finally, the time-of-flight t_f, is considered a free parameter and part of the design vector:

$$\mathbf{y}^\mathsf{T} = \left[t_f, \boldsymbol{\lambda}_0^\mathsf{T}, \boldsymbol{\lambda}_f^\mathsf{T}\right] \tag{2.81}$$

Co-state Scaling

In an effort the improve optimizer convergence, it is desirable to be able to scale some co-states to ensure they vary in similar orders of magnitude. Especially the co-state elements corresponding with the semi-parameter p and mass m can be considerably larger and smaller than the other ones, respectively. Firstly, as seen in Equation (2.61) and Equation (2.67), the term $2p/w$ requires λ_p to be very small. Similarly, in Equation (2.79) for similar values of λ_q, the term with λ_m will dominate the switching function. In other words, for comparable bounds for the co-state vector, only a small region will yield actual coasting arcs.

To counteract this behavior, either the bounds for each co-state λ_q can be individually determined, or some co-states of the initial design vector can be scaled by some parameter. Therefore instead of λ_p, the design vector uses $p \cdot \lambda_p$ and $m^{-1} \cdot \lambda_m$ instead of λ_m. So using co-state vector in Equation (2.81):

$$\boldsymbol{\lambda} = \left[p \cdot \lambda_p, \lambda_f, \lambda_g, \lambda_h, \lambda_k, m^{-1} \cdot \lambda_m\right]^\mathsf{T} \tag{2.82}$$

2.4.4. Objective Function

Recall that the formulation of the optimization problem can be stated as the problem of minimizing some objective function $J = f(\mathbf{y})$, where $\mathbf{y}^\mathsf{T} = \left[t_f, \boldsymbol{\lambda}_0^\mathsf{T}, \boldsymbol{\lambda}_f^\mathsf{T}\right]$, subject to some final constraint $\boldsymbol{\Psi}_f$. For example, when considering purely a minimum-time problem, a cost-function could be purely be determined by the time-of-flight t_f:

$$J = t_f \tag{2.83}$$

For the case of a minimum-propellant problem, the cost function would depend on the initial mass m_0 and final mass m_f, or propellant mass:

$$J = \left(1 - \frac{m_f}{m_0}\right) \tag{2.84}$$

In practice, both t_f and minimum propellant might need to be targeted, in addition to other possible objectives such as minimum radiation exposure. Generally, these consist of conflicting objectives, e.g. minimizing propellant mass causes an increase of the minimal t_f . This multi-objective optimization problem can be handled by utilizing a weighted objective function, assigning weights to each objective, and summing their results (Michalewicz, 1995):

$$J = \sum_{i=1}^{n} w_i f_i(\mathbf{y}) \tag{2.85}$$

where w_i is the weight assigned to the objective function f_i. Such an objective function is called the Aggregate Objective Function (AOF). By varying the individual weights a Pareto front of the problem can be determined. The Pareto front describes the solutions for which no other objectives can be improved, without sacrificing any other objective. In spacecraft trajectory optimization a common Pareto front is propellant mass at the cost of transfer time and vice versa. Figure 2.9 demonstrates this with an example for the Cassini benchmark model, describing an interplanetary space mission to Saturn (Schlueter et al., 2021).

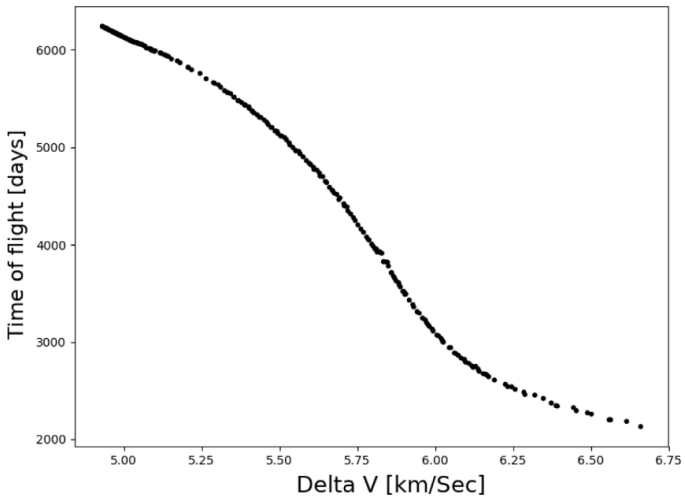

Figure 2.9: Pareto front of Cassini1 GTOP Benchmark problem (Schlueter et al., 2021).

To simplify the optimization problem, the final constraints can be incorporated into the objective function, transforming the problem into an unconstrained optimization problem. The AOF then incorporates both the target state and optimization target by adding an additional error, or penalty term to the cost function:

$$J_{error} = \sum_{i=1}^{6} w_i(\tilde{\varepsilon}_i)^2 \tag{2.86}$$

where w_i is the weight assigned to a scaled error $\tilde{\varepsilon}_i$, corresponding to each of the targeted orbital elements $\mathbf{oe} = [a, e, i, \omega, \Omega, \theta]^\mathsf{T}$. Note that Keplerian elements are used for the final target orbit, instead of the MEE that are used for the propagation of the trajectory. This allows easier handling of the target orbit and makes interpreting the optimization results more intuitive when inspecting intermediate fitness calculations. Furthermore, the true anomaly θ is included here to allow rendezvous targeting. While this will not be possible through OA, it is maintained here as the corresponding weight is set to 0 when OA is used. Finally, to improve convergence behavior and reduce weight tuning, the final orbit error is scaled with respect to the bounds set by the user. Given the absolute error of the propagated trajectory:

$$\boldsymbol{\varepsilon} = \left|\mathbf{oe}_{target} - \mathbf{oe}_{final}\right| \tag{2.87}$$

where $\mathbf{oe}^{target}$ and $\mathbf{oe}^{final}$ are the targeted and final orbital elements, respectively. The relationship in Equation (2.88) is used to determine $\tilde{\boldsymbol{\varepsilon}}$, i.e. the scaled orbit error corresponding to the elements in $\mathbf{oe}$:

$$\tilde{\boldsymbol{\varepsilon}} = 1 + \frac{\boldsymbol{\varepsilon} - \boldsymbol{\varepsilon}_{UB}}{\boldsymbol{\varepsilon}_{UB} - \boldsymbol{\varepsilon}_{LB}} \tag{2.88}$$

where $\boldsymbol{\varepsilon}_{UB}$ and $\boldsymbol{\varepsilon}_{LB}$ the user-determined upper and lower bound vectors of the final orbit error. Through this procedure, the error will be given a value $\tilde{\varepsilon}_j \in (0, 1]$ when within the constraints, and a value $\tilde{\varepsilon}_j \in (1, \infty)$ when outside of the constraints.

The full objective function used in the remainder of this work will therefore be

$$J = w_t t_f + w_m\left(1 - \frac{m_f}{m_0}\right) + \sum_{j=1}^{6} w_j(\tilde{\varepsilon}_j)^2 \tag{2.89}$$

The choice of the allowed final orbit error bounds is left free and generally depends on several factors such as mission requirements, trajectory type, or launcher characteristics. For example, Jimenez-Lluva (2017) uses the trajectory requirements as recommended by GMV for preliminary mission design shown in Table 2.4. Note he

targeted GEO applications, hence the use of final geodetic longitude, Λ, as a constraint. For rendezvous optimization a constraint on final true anomaly would be used for example. Boudestijn (2014) based his constraints on a maximum final error tolerance of 1 deg as accepted for preliminary design and Gómez-Jenkins (2015) bases accuracy requirements on the Ariane 5 launcher injection error.

Table 2.4: Upper bounds on the allowed final error in Keplerian orbital elements as used by Jimenez-Lluva (2017).

element	Upper Bound
a [km]	100.0
e [-]	0.01
i [deg]	0.1
Ω [deg]	1.0
ω [deg]	1.0
Λ [deg]	1.0

2.4.5. Differential Evolution

To solve the optimization problem as defined in the previous section, the self-adaptive DE algorithm in PaGMO, DE1220, i.e. pagmo Differential Evolution (pDE), was selected. This global optimization algorithm was selected for three main reasons. Firstly, based on an extensive literature survey on global optimization methods, DE was determined to be one of the best meta-heuristics available for this type of optimization problems (Klavers, 2020). However, the performance of the traditional DE version is very susceptible to the tuning of its optimization parameters crossover rate CR, weight coefficient F, and population size N_p, as well as the mutation variant used. The self-adaptive implementation of the DE algorithm in PaGMO circumvents the need for this tuning process by making use of two different adaptation schemes for CR and F, as well as randomly mutating the mutation variant used. Therefore, greatly reducing required user input while maintaining good convergence for different problems.

Secondly, in support of this, using pDE is also the approach recommended by previous authors Jimenez-Lluva (2017), Gómez-Jenkins (2015), and Boudestijn (2014). Thirdly, as an additional benefit from an implementation point of view, the connection between Tudat and PaGMO is already well-implemented and tested. This also allows the use of the generalized island model (Izzo et al., 2012), which provides parallel computing mechanisms as well as other advantages, such as parallel populations to further prevent premature convergence to local minima.

Traditional Differential Evolution

DE is a meta-heuristic optimization method introduced by Storn and Price (1997). Similar to other evolutionary algorithms such as Genetic Algorithms (GAs), a population of individual solutions is evolved over multiple generations to find a globally optimal individual. This section summarizes the basic mechanisms of DE, for further reading the reader is referred to either the original publication (Storn and Price, 1997) or the book outlining its mechanics in full detail by the same author (Price et al., 2005).

DE is based on four steps: initialization, mutation, crossover, and selection.

Initialization The population of size N_p is defined as:

$$x_{i,G},\ i = 1, 2, \dots, N_p \tag{2.90}$$

where i is the individual in generation G. The initial population is generally chosen randomly, covering the entire parameter space. By default, this is a uniform random distribution, but can also be created using a normal distribution around the values of a previous solution, for example, obtained through an analytical approximation method.

Mutation The various individuals in the parameter vector $x_{i,G}$ are combined to form a mutant vector v:

$$v_{i,G+1} = x_{r_1,G} + F \cdot \left(x_{r_2,G} - x_{r_3,G}\right) \tag{2.91}$$

where $r_1, r_2, r_3 \in 1, 2, \ldots, N_p$ are random integer indices, and the weight coefficient $F > 0$ and $F \in [0, 2]$. The random integer indices are also mutually different and different for each individual i. F controls the weight or amplification of the differential variation.

Crossover To diversify the mutated parameter vectors, and prevent local convergence, a crossover mechanism is used. To do this a new vector is formed, the trial vector u:

$$u_{i,G+1} = \left(u_{1i,G+1}, u_{2i,G+1}, \ldots, u_{Di,G+1}\right) \tag{2.92}$$

where

$$u_{ji,G+1} = \begin{cases} v_{ji,G+1} & \text{if } (randb(j) \leq CR) \text{ or } j = rnbr(i) \\ x_{ji,G} & \text{if } (randb(j) > CR) \text{ and } j \neq rnbr(i) \end{cases} \tag{2.93}$$
$$j = 1, 2, \ldots, D$$

where $randb(j) \in [0, 1]$ is the j^{th} evaluation of a uniform random number, $rnbr(i) \in 1, 2, \ldots, D$ is a random index and $CR \in [0, 1]$ is the crossover rate. Figure 2.10 gives an example of this mechanism for 7 parameters.

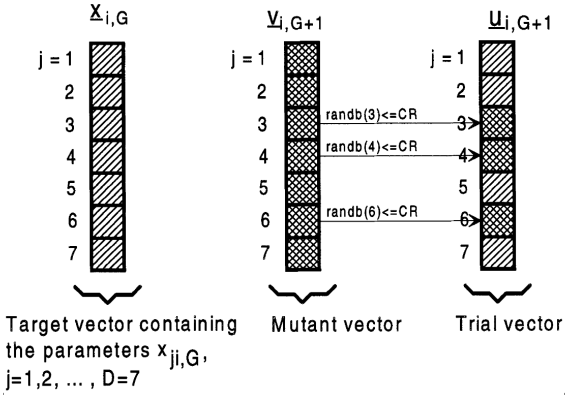

Figure 2.10: Illustration of the crossover operation (Storn and Price, 1997).

Selection Finally the trial vector $u_{i,G+1}$ is compared with the parameter vector $x_{i,G}$. If the fitness of the trial vector is larger than that of the parameter vector, it is selected to be part of the new generation. If not, the original parameter vector is maintained for the next generation.

Variations on the outlined scheme are possible, denoted using the notation $DE/x/y/z$ where:

1. x is the vector that is mutated, either randomly chosen (”rand”) or the best vector of the population (”best”), i.e. with the best fitness.

2. y is the number of difference vectors used

3. z is the crossover scheme used, for example, in this section, a binomial crossover is used (”bin”), although exponential crossover (”exp”) was used in the original proposition (Storn and Price, 1995).

Thus the variation outlined in this section is denoted as $DE/rand/1/bin$. The implementation of DE in PaGMO provides the variations shown in Table 2.5.

Table 2.5: Available variants in DE implementation in PaGMO (*Differential Evolution — Pagmo 2.17.0 Documentation* 2021).

variant
`best/1/exp`
`rand/1/exp`
`rand-to-best/1/exp`
`best/2/exp`
`rand/2/exp`
`best/1/bin`
`rand/1/bin`
`rand-to-best/1/bin`
`best/2/bin`
`rand/2/bin`

Self-Adaptive Differential Evolution

pDE uses the self-adaptation schemes proposed by Brest et al. (2006) and Elsayed et al. (2011), also called jDE and iDE, respectively. Furthermore, pDE implements an additional self-adaptation mechanism to specify the mutation variant used. Before the mutation step, the individual i is augmented with an additional integer V_i, specifying the variant to be used to generate the next trial individual. This variant V_i is selected as:

$$V_i = \begin{cases} random & r_i < \tau \\ V_i & \text{otherwise} \end{cases} \tag{2.94}$$

where $r_i \in [0, 1]$ is a random uniformly distributed number, and $\tau = 0.1$ by default. $random$ gives a randomly selected mutation variant from the set of available variants. The available variants are given in Table 2.6 and are in addition to those given in Table 2.5. The additional variants are introduced in the jDE implementation (Elsayed et al., 2011).

Table 2.6: Available variants in the jDE implementation of DE (Elsayed et al., 2011).

variant
`rand/3/exp`
`rand/3/bin`
`best/3/exp`
`best/3/bin`
`rand-to-current/2/exp`
`rand-to-current/2/bin`
`rand-to-best-and-current/2/exp`
`rand-to-best-and-current/2/bin`

With the use of SaDE, the only remaining required user input is the population size N_p. The original method recommends a population size between $N_p = 5D$ and $N_p = 10D$ where D is the number of design parameters, i.e. $D = 11$ for the minimum-time problem (5 for each initial and final co-states, and t_f), and $D = 13$ for the minimum-propellant problem. The reference implementation in Jimenez-Lluva (2017) employed $N_p = 10D$, which he showed provided generally reliable results. Because the optimization performance was not the primary focus of this project, no further analysis of the impact of the population size on the optimizer performance was done, and this same rule-of-thumb is used in the OT, and was confirmed to yield satisfactory results. Nevertheless, it should be noted that there can be room for improvement in general optimization performance (in terms of computation times) by further analyzing the effect of N_p for each specific problem, as well as the selection of mutation variants available to SaDE.

2.5. Summary

In summary, MEE are used to describe the spacecraft state. Several perturbations can be taken into account, the EOM of which are readily available in terms of MEE. Through the use of OA the spacecraft state is efficiently propagated for long periods of time, but at the cost of the loss in accuracy of the fast-changing orbital element. OA uses an 'embedded' CI propagation to propagate the spacecraft state for a single revolution, the average state progression obtained from these are then propagated using a variable-step integrator. Through this approach, the computational requirements for propagating a single trajectory can be reduced.

To perform the optimization process, the spacecraft control is parameterized to reduce the search space. This is accomplished by deriving the optimal control laws in terms of MEE co-states. In contrast to indirect techniques, only expressions for the optimal steering inputs are derived by using the optimality conditions. This control parametrization technique results in n nodes, defining the co-state arcs. Based on previous work, two nodes are used, i.e. a single co-state arc. Thus, the decision vector consists of 11 parameters for the minimum time problem and 13 for the minimum propellant problem. Furthermore, a co-state scaling method is used to ensure the design vector parameters are of similar magnitude, to improve convergence behavior.

The propagated trajectory will have an associated fitness value, defined by an Aggregate Objective Function (AOF), which incorporates the final orbit error, time-of-flight, and propellant mass; weights can be assigned to each, or even fully disabled. The self-adaptive variant of DE is used to optimize the overall optimization problem, avoiding the need for optimizer tuning, and therefore expected more robust convergence which comes at the cost of slower convergence.

3

Validation, Verification, and Propagator Testing

In Chapter 2 an implementation of an optimization technique was introduced, using OA to propagate a trajectory, and SaDE to optimize the parameterized control inputs, resulting in an Optimization Tool (OT) in Tudat. This chapter discusses the testing efforts of the implementation and an analysis of the integration parameters required to accurately capture a specific trajectory. In the context of this project, *validation* deals with testing against the physical reality and *verification* with testing against other models. Because validation is a difficult activity for such a project we generally limit ourselves to verification of the OT. Likewise, comparing propagated trajectories to results obtained from a properly validated tool is considered verification for consistency; for the purpose of this project we limit ourselves to the verification of the OT. Nevertheless, it is emphasized that it is critical to verify the obtained solutions with a properly validated propagation tool for actual applications. Closely related to verification is the testing of the propagator to determine the parameters required to ensure reliable results.

Not all components require thorough testing as many are either already available, such as SaDE in PaGMO, or have been extensively used previously as part of Tudat. Firstly Section 3.1 discusses the implementation of the orbital perturbations and the thrust under shadow conditions. Section 3.2 moves to verify the implemented propagation, both CI and OA by comparing with reference benchmark trajectories obtained from high-accuracy propagation methods in Tudat. These high-accuracy benchmark trajectories are obtained through the Cowell propagator in Tudat using a RK7(8) integrator with step-sizes in the order of tens of seconds.

3.1. Orbital Perturbations

As mentioned in Section 2.2.4, each perturbation implemented in the hybrid propagation model has been implemented in Tudat already and can be considered extensively tested. However, as they are part of a novel propagation implementation, the actions in this section serve as an additional test, to make sure they each behave as expected. The perturbations due to the J_2 effect and aerodynamic drag on a trajectory are evaluated. Additionally, the impact of the reduction of thrust due to eclipse conditions is verified. This section aims to verify that the CI implementation properly implements these perturbations, i.e. does a resulting trajectory from a CI propagation subject to certain perturbations, behave as expected. This will be accomplished by comparing the CI result to known solutions or approximations to verify their behavior. The behavior of OA will be discussed in Section 3.2.

3.1.1. Secular Drift due to Oblateness

As shown in Section 2.2.4, the oblateness of the Earth causes a secular drift of the RAAN Ω, and argument of periapsis ω. This drift can be approximated by Equations (2.21) and (2.22). It should be noted that these equations only describe a first-order approximation of the secular drift. The other (mean-mean) orbital elements are taken as constant. A trajectory with initial Keplerian elements $a = 10\,000$ km, $e = 0.1$, $i = 60°$ is propagated for 60 days. The trajectory is propagated using CI and $n_k = 40$. Only the J_2 effect is taken into account, with no other perturbations, nor thrust.

The absolute differences, $|\varepsilon_\Omega| = |\Omega_{\text{analytic}} - \Omega_{\text{CI}}|$, and $|\varepsilon_\omega| = |\omega_{\text{analytic}} - \omega_{\text{CI}}|$ between the analytically predicted mean elements and the CI propagated are shown in Figure 3.1.

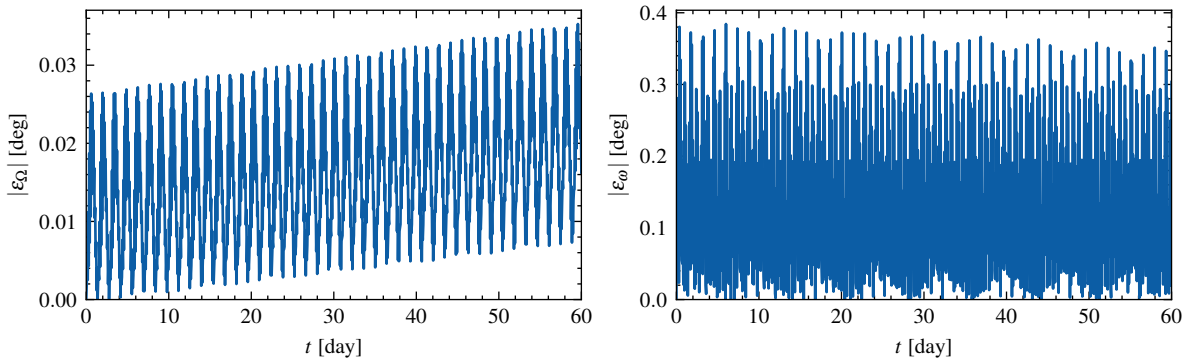

Figure 3.1: Absolute difference of Ω and ω between analytically expected drift and CI propagated trajectory.

Figure 3.1 clearly shows that both Ω and ω have a short-period variation, reflecting the secular approximation. More importantly, Ω shows a small secular error, which can be attributed to the first-order approximation of $\dot{\Omega}$. Although Figure 3.1 demonstrates the general effect of the J_2 is as expected, i.e. the first-order secular drifts are accurately captured, comparison with a reference benchmark trajectory shows higher-order effects are also accurately captured. Again, Figure 3.2 shows the absolute error between the trajectory propagated with the hybrid implementation and a high-accuracy benchmark trajectory.

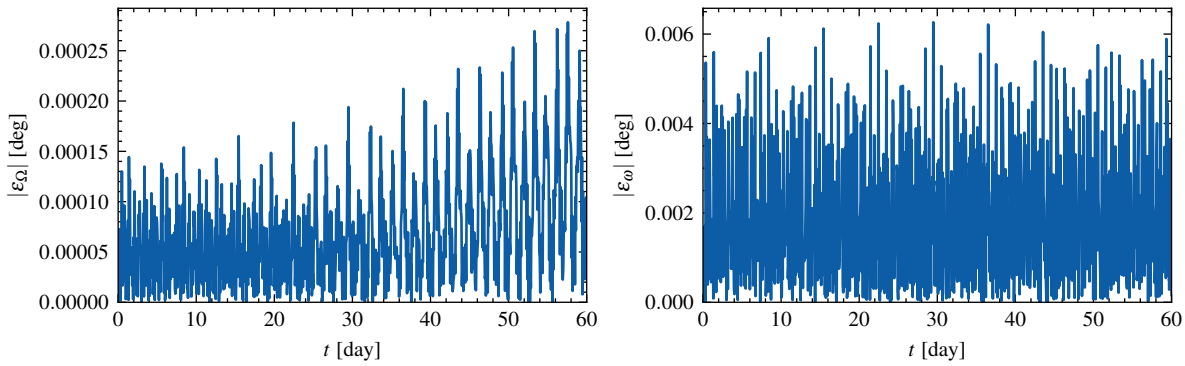

Figure 3.2: Absolute difference of Ω and ω between high-accuracy reference trajectory and CI propagated trajectory.

For this example, the maximum relative error compared to the expected drifts is in the order of 10^{-4} % and 10^{-2} % for Ω and ω, respectively. Based on this we can conclude that the implementation of CI does not significantly influence the effect of the J_2 perturbation on the propagated trajectory.

3.1.2. Aerodynamic Drag

The influence of aerodynamic drag depends on the spacecraft shape and size, orientation, mass, and atmospheric density. The atmospheric density ρ is especially difficult to determine as it is largely determined by the atmospheric conditions at specific altitudes, which in turn are largely influenced by the solar cycle. For example, Figure 3.3 shows the satellite lifetimes during solar minimum and maximum for a range of ballistic coefficients.

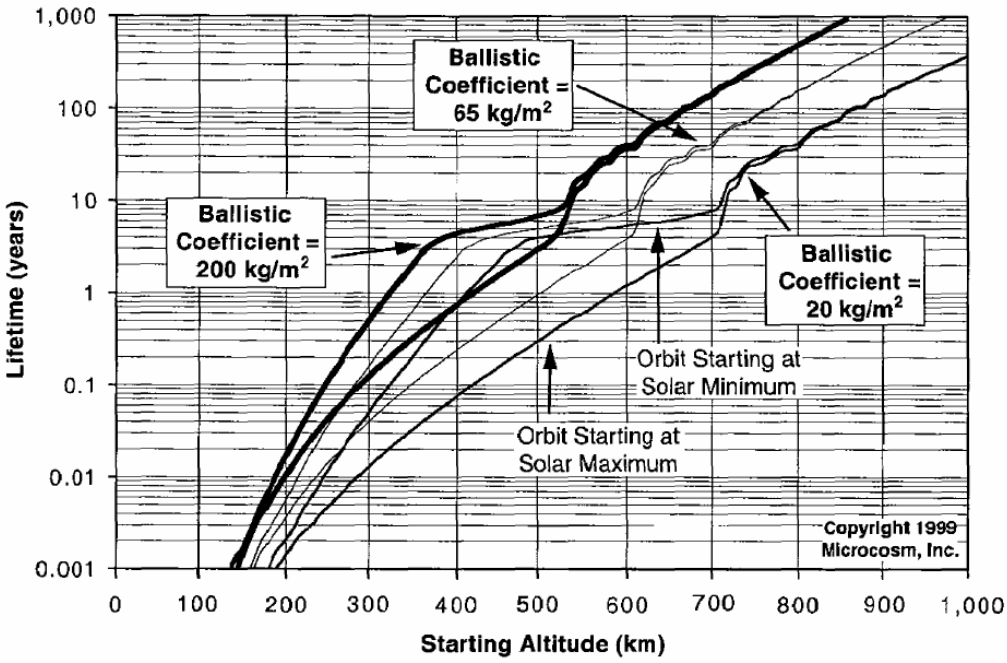

Figure 3.3: Satellite lifetime as a function of altitude, solar cycle phase, ballistic coefficient (Wertz, 2001).

The choice of atmospheric model, i.e. how ρ is determined, is a prime source of uncertainty. As mentioned in Section 2.2, this atmosphere model is approximated using tabulated values, available in Tudat, which is considered sufficient for first-order approximations. The spacecraft drag coefficient C_D and frontal surface area A are assumed constant. This allows preliminary analysis of drag on the CI.

An approximation of the expected decay of the semi-major axis, a, due to aerodynamic drag and assuming a circular orbit, is given by (Wakker, 2015):

$$\Delta a_{rev} = -2\pi\left(\frac{C_d A}{m}\right)\rho a^2 \tag{3.1}$$

where Δa_{rev} is the change in semi-major axis per orbital revolution. C_D is the drag coefficient, A the cross-sectional area, and ρ atmospheric density. It should be noted that this is a simplified approximation, but it does demonstrate the behavior of our propagation is as expected, as seen in Figure 3.4. This holds for a circular orbit with initial conditions $a = 6678.0\,\text{km}$, $e = 0$, $i = 79°$. Using a satellite with constant mass $m = 2.0\,\text{kg}$, frontal area $A = 0.028\,\text{m}^2$ and constant drag coefficient $C_D = 2.2$, which is representative of a CubeSat (Sundaramoorthy et al., 2010). The atmospheric density ρ is obtained from the tabulated value at that altitude.

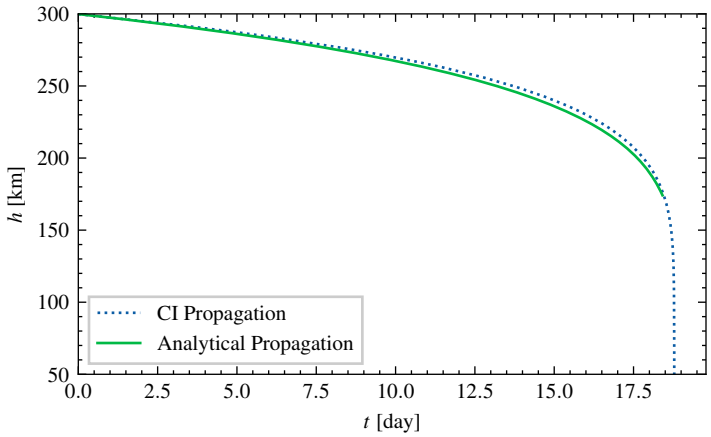

Figure 3.4: Decay of the semi-major axis due to aerodynamics drag.

Although this shows a similar decay pattern for the CI propagated trajectory as the expected analytical decay, comparison with a reference trajectory further confirms consistency. As the atmosphere models and aerodynamic perturbing equations of motion in Tudat have also been extensively used and tested, we can use a similar approach to verify the CI propagation. Again, a reference trajectory is compared to a trajectory propagated using the hybrid method.

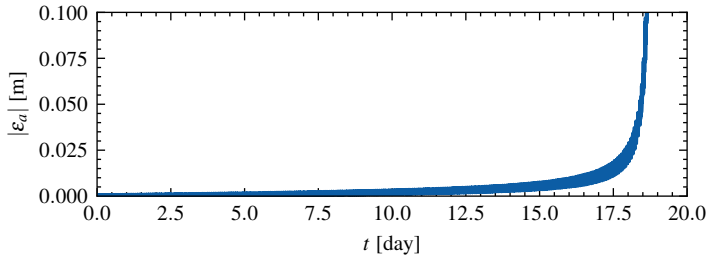

Figure 3.5: Absolute difference in semi-major axis between CI and benchmark propagated trajectories.

From Figure 3.5 it is clear that the implemented aerodynamic model does not create any noticeable error term, with the error only increasing somewhat at low altitudes, i.e. $h < 100\,\text{km}$, but remaining small.

3.1.3. Thrust Under Eclipse Conditions

As discussed in Section 2.2.4, the eclipse model has previously been implemented in Tudat, therefore the shadow function is assumed to function as expected. Nevertheless, its effect on the expected thrust profile is briefly investigated. A LEO trajectory with $a = 6927.0\,\text{km}$, $e = 0.01$ and $i = 0°$, is propagated for 50 days, using a tangential continuous-thrust model. The effect of disabled thrust during eclipse conditions can then be observed.

Figure 3.6: Top-down view of the propagated trajectory, showing regions with thrust in yellow and thrust off in purple.

In Figure 3.6 a top-down view of the propagated trajectory is shown. Areas during which thrust is disabled are shown in dark purple, thrust enabled is shown in yellow. It can be seen the areas of solar shadow rotate with the rotation of Earth about the Sun. Secondly, it is apparent that the semi-major axis increases, as well as the eccentricity.

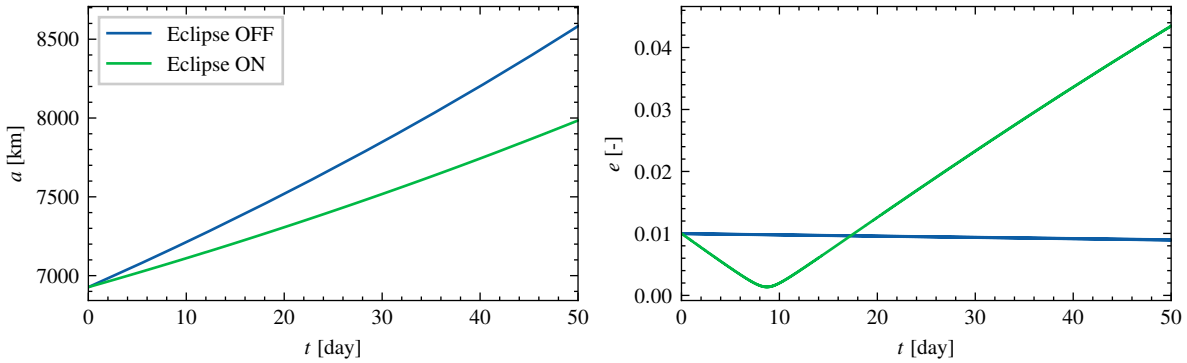

Figure 3.7: Semi-major axis and eccentricity for two propagated trajectories, with and without eclipse conditions.

This is also shown in Figure 3.7, showing the progression of the semi-major axis and eccentricity. Unsurprisingly the obtained change in semi-major axis is lower when thrust during eclipse is disabled. For constant tangential thrust in a near-circular orbit, the eccentricity will remain approximately constant as can be derived from Equation (2.11). When thrust is only possible during specific parts of the trajectory, an increase of the eccentricity is to be expected, as apogee will be raised predominantly in the shadow of the Earth. But, because the spacecraft is initially in shadow near perigee, the eccentricity will first decrease (as perigee is raised near apogee when thrust is enabled), before increasing again.

3.1.4. Summary

Based on the previous sections we conclude the implemented perturbations for the hybrid MEE propagator behave as expected. The secular drift induced by the oblateness of the Earth corresponds to the expected drift based on a

first-order analysis, as well as the observed drift in a numerically propagated, high-accuracy reference trajectory. The orbital decay caused by aerodynamic drag is also accurately captured by the (simplified) drag model. Finally, the effect of disabled thrust during eclipse conditions on the propagated trajectory is as expected and thrust is properly switched off during shadow conditions. It is worth repeating that the reference benchmark trajectory was propagated using a different Cowell propagator, to ensure little overlap with the implemented hybrid MEE propagation. Furthermore, the goal of this section was to verify the effect of the perturbations on the propagation, the implementation of the perturbations is considered properly tested due to their heritage in Tudat.

The remainder of the section will further verify the implemented propagator and investigate the required integration segments for OA.

3.2. Propagator

Verification of the implemented propagator is vital to ensure good performance of the optimization algorithm, both CI and OA. For the CI propagator, or more accurately: propagation using MEE and fixed step size in eccentric anomaly E. The number of integration epochs n_k, will largely determine its accuracy. Work by previous authors includes an analysis of required n_k. This is done to both evaluate its performance and determine suitable parameters that will be used for the optimization process, ultimately requiring a trade-off between accuracy and computational performance. Both Boudestijn (2014) and Jimenez-Lluva (2017) used a value of $n_k = 40$ for their propagation. Gómez-Jenkins (2015) included atmospheric drag and third body perturbations in his analysis and used $n_k = 70$ as the value best meeting his requirements. Because the work in this project includes the additional J_2 and thrust under eclipse conditions, and uses a fully numerical approach for the OA method, the impact of these perturbations on the propagation will be tested.

Two different initial orbits are used for the various test cases. The first test case uses an inclined GTO with high eccentricity and a low perigee. This orbit was selected for two reasons. Firstly, these are the same conditions used by Geffroy and Epenoy (1997) on which subsequently Jimenez-Lluva (2017) based his work. This allows us to compare the performance of the propagator to external references. No perturbations are taken into account for this test case as they are also not used in the reference results. The other spacecraft parameters are equal to those in the reference case: $T = 0.350\,\text{N}$, $m_0 = 2000\,\text{kg}$, and $I_{sp} = 2000\,\text{s}$.

For the second test case, the initial trajectory is a polar orbit in LEO. This orbital regime is used later in the project for investigating transfers to space debris objects. Furthermore, the low altitude and high inclination mean both the oblateness of the Earth and aerodynamic drag perturbations will play a role. This test case serves to investigate the impact of the additional perturbations on the integration requirements. Finally, the low orbital period will present different challenges for the OA approach when compared to the relatively larger orbital period of the GTO trajectory. The full input parameters of the verification cases are given in Table 3.1.

Table 3.1: Parameters used in both validation cases. Case 1 represents the initial conditions of a GTO. Case 2 represents the initial conditions of a polar orbit in LEO.

	Case 1	**Case 2**
a_0 [km]	24 505.9	7103.0
e_0 [-]	0.725	0.01
i_0 [deg]	7.0	95.5
ω_0 [deg]	0.0	0.0
Ω_0 [deg]	0.0	0.0
θ_0 [deg]	0.0	0.0
T [N]	0.35	0.5
I_{sp} [s]	2000.0	2000.0
m_0 [kg]	2000.0	2000.0
J_2	no	yes
drag	no	yes
eclipse	no	yes

The propagator performance is verified using three simplified thrust profiles: tangential, out-of-plane, and radial

thrust. To allow an accurate comparison, final orbit error constraints are taken equal to those used by Jimenez-Lluva (2017) as shown in Table 2.4. The reference trajectories are propagated by Tudat using the same parameters, but using a high-accuracy variable step size integrator and general Cowell propagation instead. Because this propagator has been extensively used in existing research and shares no implementation with the CI and OA approach as discussed in this work, this reference propagation can be considered thoroughly validated and usable as reference 'ground truth'.

The constant yaw- and pitch steering angles used for the three thrust profiles are defined as:

$$\begin{aligned} \text{tangential:} \quad & \alpha = \gamma \quad ; \quad \beta = 0 \\ \text{radial:} \quad & \alpha = \frac{\pi}{2} \quad ; \quad \beta = 0 \\ \text{out-of-plane:} \quad & \alpha = \gamma \quad ; \quad \beta = \text{sgn}(\cos(\omega + \theta))\frac{\pi}{2} \end{aligned}$$

It is worth repeating that α is defined with respect to the S-direction, therefore the tangential direction is defined through the flight-path angle γ. Equivalently for the out-of-plane thrust profile (aimed at maximizing inclination change), thrust is in the positive out-of-plane direction for $v_z > 0$ and in the negative direction for $v_z < 0$:

$$\alpha_{T_W} \equiv \begin{cases} 1 & \text{if } v_z > 0 \\ -1 & \text{if } v_z < 0 \end{cases} \tag{3.2}$$

where v_z is obtained from Equation (2.9). A geometric representation of these three profiles is shown in Figure 3.8.

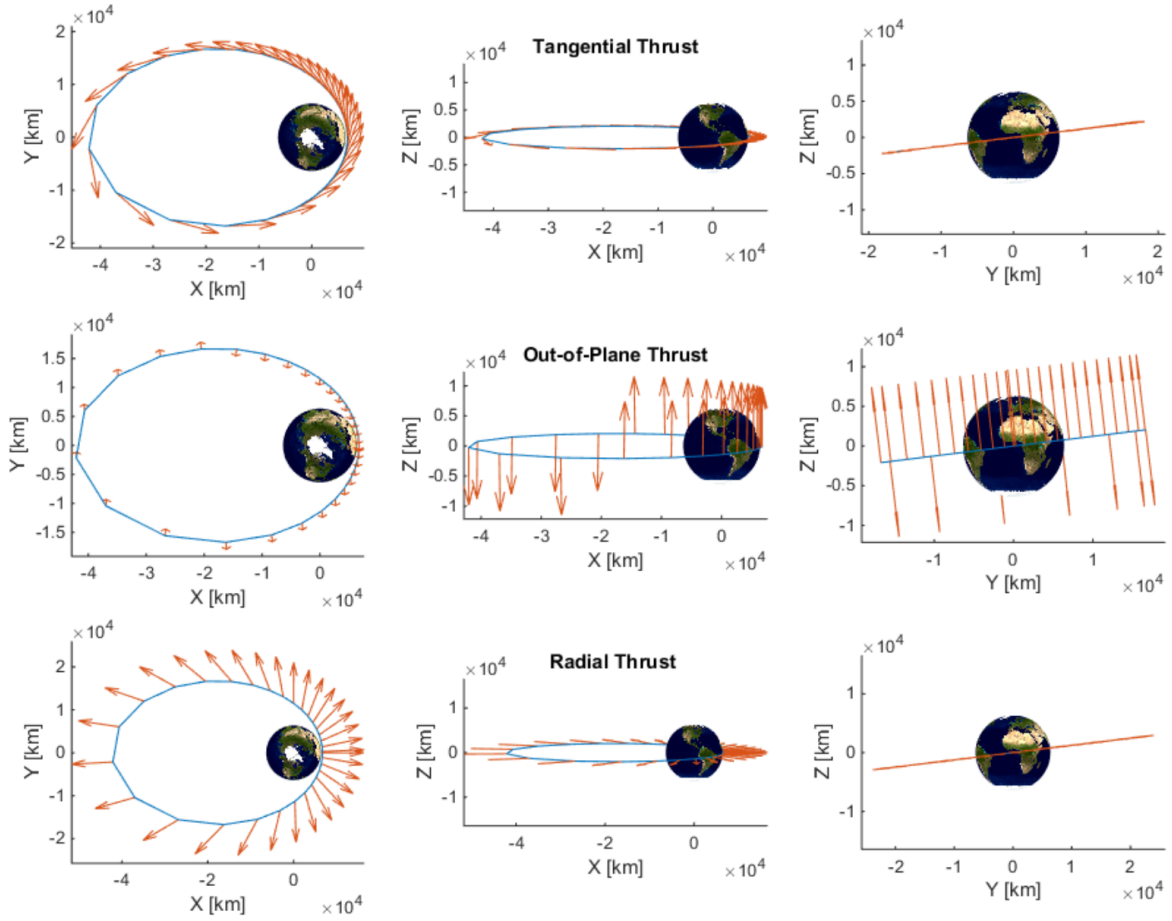

Figure 3.8: Geometric representation of the three simplified thrust profiles (Jimenez-Lluva, 2017)

For both test cases, we first look at the difference between the CI and benchmark trajectory, to both verify its

performance and determine the step size required to accurately capture the dynamics, similarly to the previous section but now incorporating a thrust model and the full perturbations for the second test case. Following this, an analysis on the OA performance is done, investigating the impact of n_k on the averaging approach, i.e. the number of state derivatives used in the numerical quadrature. It is worth repeating that n_k corresponds to the number of propagation epochs, and thus the fixed step-size in eccentric anomaly: $\Delta E = 2\pi/n_k$, as described in Section 2.3. Therefore, n_k also corresponds to the number of integration segments used in the numerical quadrature, as was shown in Equation (2.49).

3.2.1. Case 1: GTO Trajectory

The progression of the first three Keplerian elements, a, e and i, as a result of tangential, radial, and out-of-plane thrust is shown in Figures 3.9 to 3.11, as propagated by the reference benchmark. For tangential thrust a secular increase in semi-major axis and a decrease in eccentricity can be observed, which is as expected based on Gauss' planetary equations. For radial thrust, only a short-period variation in eccentricity, with no secular effects can be seen. For out-of-plane thrust, an increase in inclination, with no effect on the other elements is seen, again as expected.

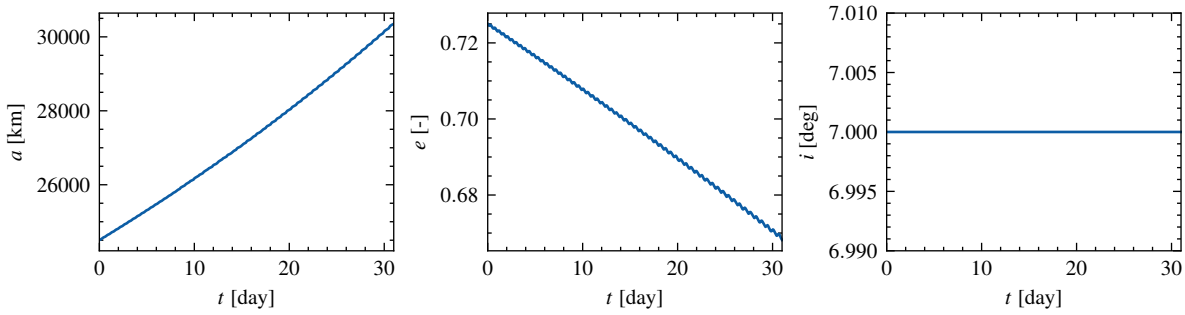

Figure 3.9: Progression of the first three Keplerian elements for the tangential thrusting program, propagated by the reference benchmark.

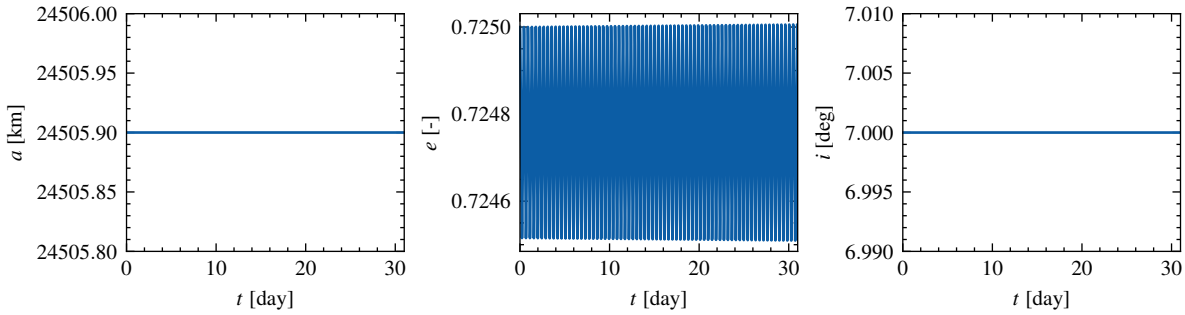

Figure 3.10: Progression of the first three Keplerian elements for the radial thrusting program, propagated by the reference benchmark.

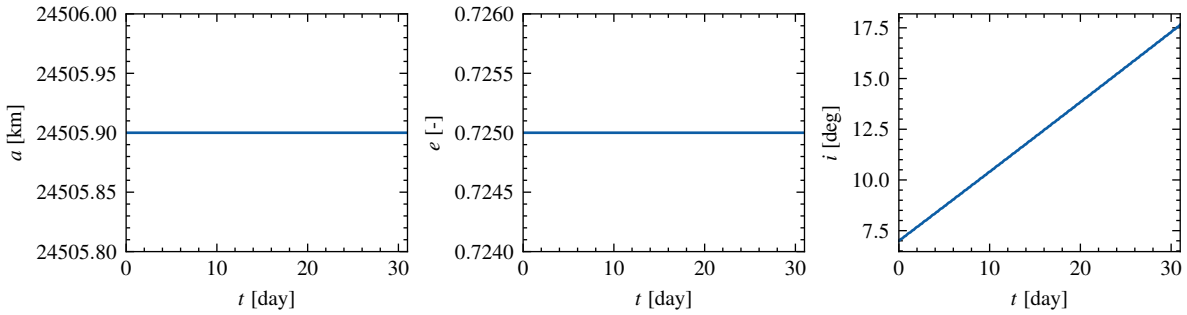

Figure 3.11: Progression of the first three Keplerian elements for the out-of-plane thrusting program, propagated by the reference benchmark.

CI Analysis

Figures 3.12 to 3.14 show the absolute difference between the CI propagated trajectory and the benchmark trajectory for the last 10 days and a range of n_k. Only the last part is shown here demonstrating the behavior of the difference in more detail. Although each element, for each propagation type, remains well within the required boundaries as previously discussed in Section 2.4, $n_k = 20$ and $n_k = 30$ shows a distinct secular trend. For $n_k \geq 40$ the behavior of the error is consistent.

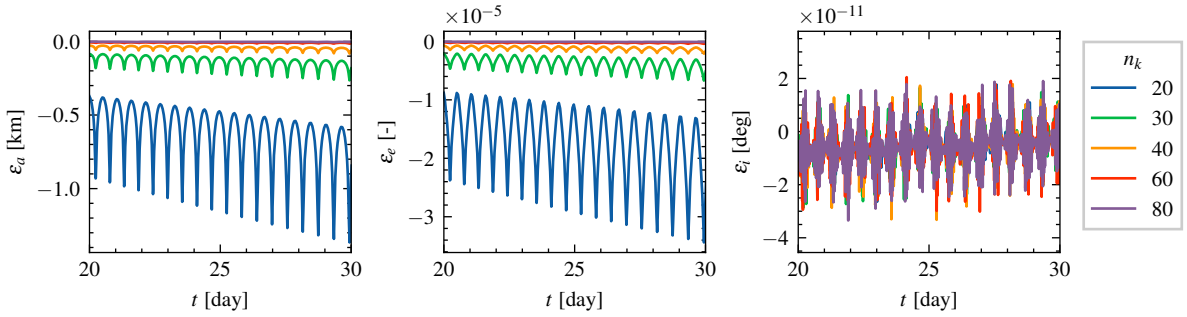

Figure 3.12: Error between the CI propagation and benchmark trajectory for the tangential thrust case.

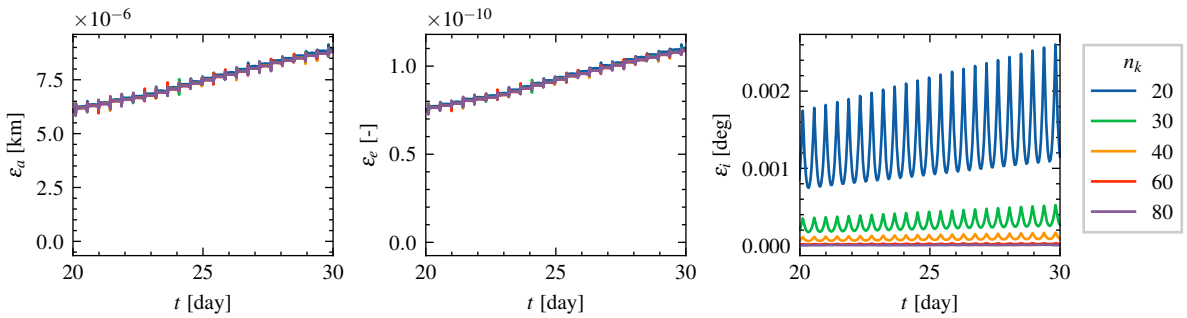

Figure 3.13: Error between the CI propagation and benchmark trajectory for the out-of-plane thrust case.

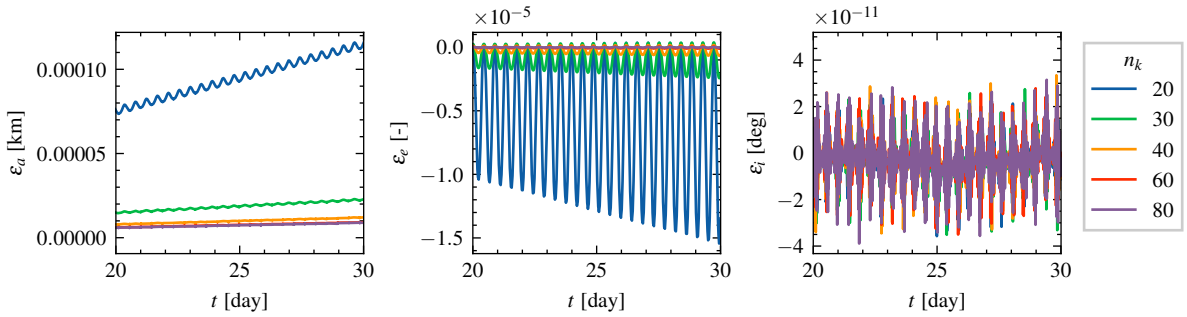

Figure 3.14: Error between the CI propagation and benchmark trajectory for the radial thrust case.

The absolute error at $t_f = 30$ days and the computational CPU time are given in Table 3.2, i.e. only the time used by the CPU to perform the propagation. The computational speed is averaged over 100 runs, to ensure random variations are averaged out. Although computational speeds can vary significantly, each additional 10 integration segments increases computation times by about 25%. $n_k = 40$ provides a good balance between accuracy and computational time as any lower shows a distinctly increasing error, which can accumulate for large propagation times. Note that the CPU times given in Table 3.2 cannot be compared to work by other authors as these largely depend on the specific implementation and machinery used. Finally, because there are still some short-period variations in the difference between the two propagations, especially for lower n_k, the final error at $t_f = 30$ days is of course to some extent somewhat arbitrary. Nonetheless, because the amplitude of these short-period variations remains well within the previously discussed constraints, this is still valid. In summary, we conclude that the CI propagation for the GTO trajectory is verifiably accurate for $n_k \geq 40$, which supports the same conclusion reached by previous authors.

Table 3.2: Absolute difference between reference trajectory and CI trajectory for each thrust profile at $t_f = 30$ days, and average CPU time per individual run, averaged over 100 runs.

	n_k	$\lvert\varepsilon_a\rvert$ [m]	$\lvert\varepsilon_e\rvert$ [-]	$\lvert\varepsilon_i\rvert$ [deg]	CPU time [ms]
tangential	20	8.44×10^{2}	2.42×10^{-5}	4.85×10^{-12}	19.1
	30	1.83×10^{2}	5.15×10^{-6}	1.08×10^{-11}	25.5
	40	6.07×10^{1}	1.70×10^{-6}	9.97×10^{-12}	33.2
	60	1.19×10^{1}	3.33×10^{-7}	4.89×10^{-12}	50.4
	80	3.68	1.03×10^{-7}	1.04×10^{-11}	68.8
radial	20	1.16×10^{-1}	1.35×10^{-5}	4.82×10^{-12}	19.3
	30	2.30×10^{-2}	2.08×10^{-6}	6.46×10^{-12}	29.2
	40	1.21×10^{-2}	5.84×10^{-7}	3.29×10^{-12}	44.8
	60	9.23×10^{-3}	9.24×10^{-8}	4.42×10^{-12}	70.0
	80	8.89×10^{-3}	2.71×10^{-8}	3.41×10^{-12}	93.2
out-of-plane	20	8.94×10^{-3}	1.10×10^{-10}	1.15×10^{-3}	21.7
	30	8.82×10^{-3}	1.09×10^{-10}	2.66×10^{-4}	34.8
	40	8.81×10^{-3}	1.09×10^{-10}	8.91×10^{-5}	40.2
	60	8.80×10^{-3}	1.09×10^{-10}	1.81×10^{-5}	72.4
	80	8.80×10^{-3}	1.09×10^{-10}	5.77×10^{-6}	98.8

OA analysis

To investigate the behavior of the OA propagation, a similar approach as in the previous section is taken. However, in contrast, only the secular trend of the differences is taken into account, as short-period variations disappear through the use of OA. This is accomplished by observing the error at each apogee passage, i.e. for $\theta = \pi$ rad. This is done because we are most interested in the secular trend of the differences, to gain a better understanding of its behavior. Near apogee, the dynamics change slowest and thus are less impacted by a small error in true anomaly. In contrast, the difference between each OA epoch and the benchmark trajectory could be arbitrarily within a short-period variation. To enable comparison at exact epochs, a cubic spline interpolator is used to

approximate the error at shared epochs between the reference benchmark and the trajectory propagated through OA. To propagate the state derivative averages a fourth-order RKF integrator is used, with tolerances $\epsilon_{abs} = \epsilon_{rel} = 10^{-3}$ and initial step size $h_0 = 1$ d. These parameters were tested by Gómez-Jenkins (2015) and were found to be sufficient. This was confirmed by performing several with varying the relative and absolute tolerances. Indeed, lower tolerances yielded solutions with unacceptable errors, whereas higher tolerances did not yield a noticeable accuracy improvement.

tangential thrust From Figure 3.15 the secular increasing difference in semi-major axis is immediately most apparent. As expected, for increasing n_k, the difference decreases, which is explained by the trapezoidal integration scheme used to compute $\Delta\mathbf{x}$. The increasing difference in a is also expected and can be explained by the OA approximation. The second-order increase of the semi-major axis, caused by the acceleration in the tangential direction, will be under- or overestimated by the OA technique. Nevertheless, the difference in the order of a few tens of kilometers is still deemed acceptable for preliminary design, in the case of transfer trajectories to GEO. Furthermore, it is noted that the difference in semi-major axis is already drastically reduced compared to the results obtained by Jimenez-Lluva (2017). For $n_k = 40$: approximately 100 km after 20 days compared to 20 km for the current implementation. This is the result of the use of both a multi-step integration scheme and adaptive OA step size. Nevertheless, the tangential thrust case highlights a limitation of the OA method. The difference in eccentricity is sufficiently small for all $n_k > 30$ and the difference in inclination, $\mathcal{O}(10^{-11}$ deg), are numerical errors, as can be expected due to the lack of an out-of-plane acceleration component. It should be noted that the error accumulation of the semi-major axis, does not cause for major concern, as realistic trajectories will not consist of purely tangential thrust. For example, a GTO to GEO requires both a plane change and circularization effort.

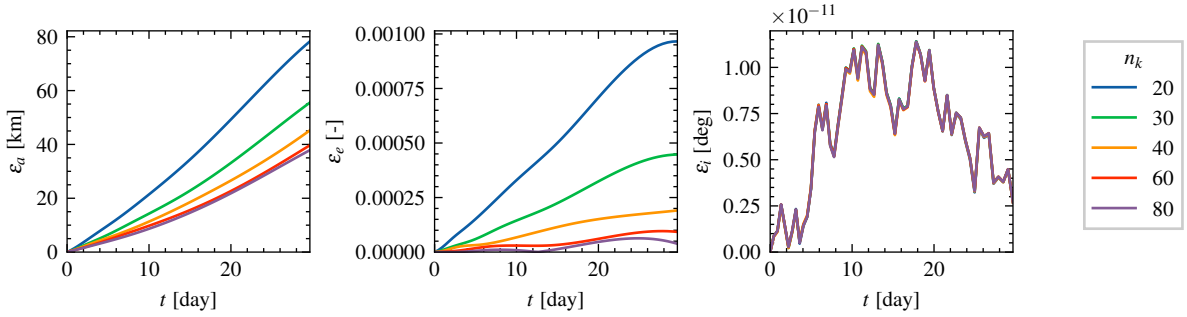

Figure 3.15: Interpolated absolute error at apogee between OA and benchmark trajectory for tangential thrust.

radial thrust The radial thrust profile is dominated by short-term oscillations (Figure 3.10) with only a very small secular component for the change in orbital elements. Again, $n_k = 20$ shows an unacceptable error behavior (Figure 3.16), in this case for the eccentricity, as it fails to accurately capture the short-period variations.

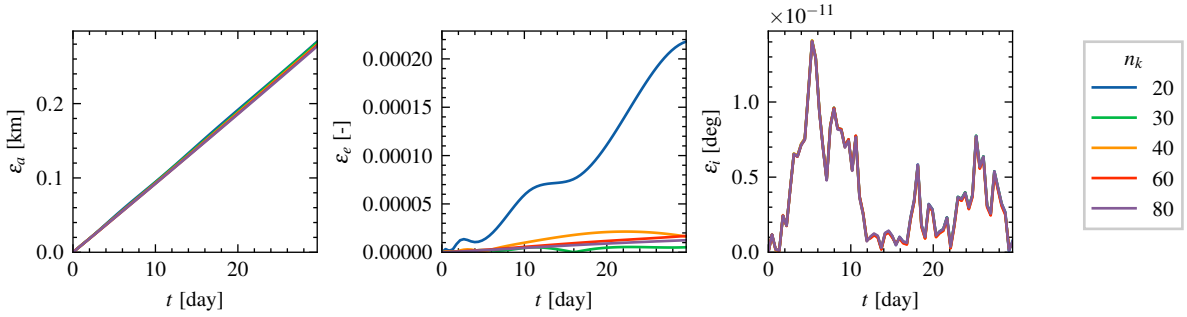

Figure 3.16: Interpolated absolute error at apogee between OA and benchmark trajectory for radial thrust.

out-of-plane thrust Surprisingly, the out-of-plane thrust profile reveals a small error in a and e (Figure 3.17), that cannot be attributed to rounding or numerical errors. It is suspected this error is caused by the implementation

of the thrust profile in the MEE propagation. Still, this is acceptable as the error is sufficiently small and only occurs for these simplified thrust profiles. The error in inclination again decreases for increasing n_k.

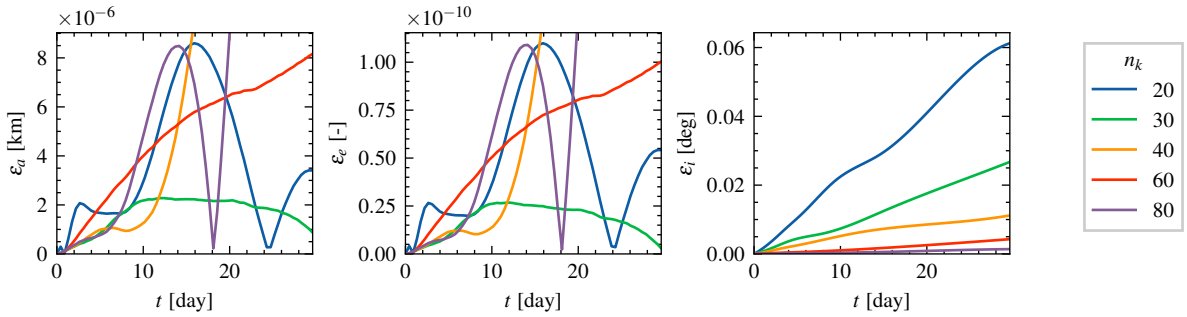

Figure 3.17: Interpolated absolute error at apogee between OA and benchmark trajectory for out-of-plane thrust.

Nonetheless, each case shows a significant improvement over the results obtained by Jimenez-Lluva (2017). The author suspects this can be largely attributed to the numerical integration employed, which is believed to be standard Euler integration, although not explicitly stated. A large accumulation of under- or overestimation is visible, especially for the tangential-thrust case used, which is often the case for the Euler approximation, and which can be eliminated by using a higher-order numerical integration method. Jimenez-Lluva also notes the apparent higher accuracy achieved by Boudestijn (2014). The complete reference results are provided in Appendix A.2.

Overall the accuracy of the OA approximation is deemed acceptable for preliminary design, showing improved results compared to the reference implementation, Jimenez-Lluva (2017), for each thrust profile. Nevertheless, for certain elements and certain cases, the difference will show a diverging behavior, most apparent for the semi-major axis in the tangential-thrust case. Although these types of trajectories are not considered in this project, care should be taken when employing the OA approximation for trajectories such as Lunar transfer trajectories.

3.2.2. Case 2: LEO Trajectory

Like Case 1, each initial state is propagated for 30 days using a tangential, radial, and out-of-plane thrust profile. First, the CI propagations are compared to the reference benchmark. Because the orbital period is significantly smaller, only a section of about 2 hours, near the end of the propagation is shown. The full results of the benchmark trajectories and error behavior are found in Appendix A.1. The error between the CI and benchmark trajectory for the tangential thrust case is shown in Figure 3.18. The other thrust cases behave comparably and can also be found in Appendix A.1.

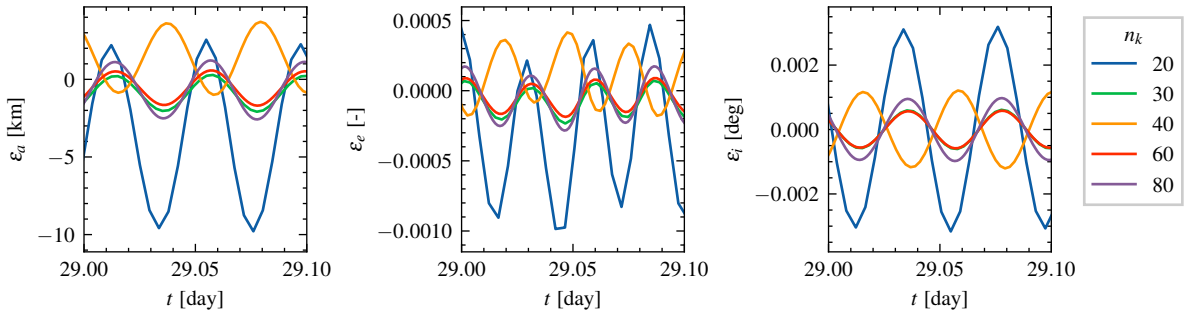

Figure 3.18: Error between the CI propagation and benchmark trajectory for the tangential thrust case.

Because the error shows oscillatory behavior, caused to the short-period variations of the trajectory due to the perturbations, direct numerical analysis of the error at t_f has little extra value. Therefore, the discussion is limited to the average behavior of the error. In general, the error behaves as expected: increasing n_k increases the accuracy, as the changing dynamics due to perturbations can be more accurately captured (Figure 3.18). Again, $n_k = 20$ and to a lesser degree $n_k = 30$ show an unacceptable error. For the tangential thrust case, the error using

$n_k = 40$ is actually larger than for $n_k = 30$. Additionally, the general oscillatory behavior of the error appears exactly mirrored. However, it should be noted this is no cause for concern, for the simple reason that the amplitude of the short-period variations of each element due to perturbations, is considerably larger. Because these short-period variations disappear through the use of OA, these errors are acceptable as long as their amplitude remains well within this range. For example, the amplitude of the short-period variation of the inclination, $\Delta i_{sh,max}$, can be approximated by (Wakker, 2015):

$$\Delta i_{sh,max} = \left| \frac{3}{8} J_2 \left(\frac{R_E}{\bar{a}} \right)^2 \sin 2\bar{i} \right| \tag{3.3}$$

where $\bar{a}$ and $\bar{i}$ are the mean semi-major axis and eccentricity, respectively. For the example trajectory with $\bar{a} = 7103.0$ km and $\bar{i} = 95.5$ deg this yields $\Delta i_{sh,max} = 0.00358$ deg, which is larger than the differences shown in Figure 3.18.

Based on the behavior of the error, $n_k = 60$ is considered as providing a reasonable trade-off between computation times and predictable propagation performance. As shown previously, computation times increase linearly with increasing n_k. Any higher number of segments does not significantly increase performance, any lower either shows too large an error. This is for example apparent in the radial thrust case, where the eccentricity has slightly accumulated, while the mean of the error for $n_k \geq 60$ remains approximately 0 (Figure 3.18).

Repeating the same exercise for the LEO case with OA propagation does not yield any useful results, as is apparent from Figure 3.19. Although the magnitude of the error remains within acceptable boundaries, its behavior is seemingly random and has no evident dependence on the number of segments n_k. For these cases, the error is no longer dominated by the number of integration segments n_k, but by the limitations of the OA method to capture the short-term oscillations caused by the various perturbations. This can be interpreted as a failure to accurately sample the difference at identical locations. The magnitude of these oscillations is significantly larger than their secular effects, including thrust. Because of the averaging effect, these variations disappear.

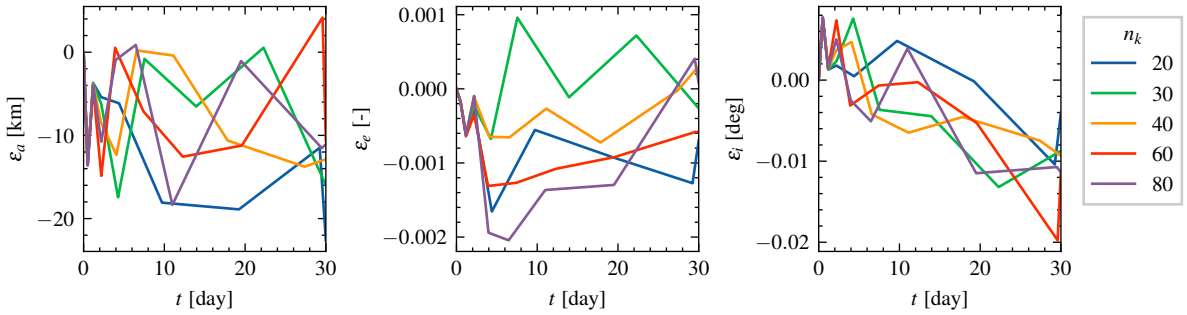

Figure 3.19: Error between the OA propagation and benchmark trajectory for the tangential thrust case.

This effect is illustrated by Figure 3.20, showing the values of the first three Keplerian elements of the propagated benchmark trajectory and the OA propagated trajectories. Firstly, it can be seen that the magnitudes of the semi-major axis, eccentricity, and inclination short-periodic variations are as much as 20 km, 0.03, and 0.01°, respectively. The OA method still captures the secular trend but can be seen diverging from the oscillatory changes, in particular for the inclination. The overall trend of semi-major axis and eccentricity is considered good. It is suspected this diverging difference is caused by the approximation used for the time-step conversion: $\mathrm{d}E/\mathrm{d}t \approx na/r$ (Equation (2.43)). The full expression for $\mathrm{d}E/\mathrm{d}t$ follows from the derivation of the Gaussian form of the planetary equations as given by Equation (2.42):

$$\frac{\mathrm{d}E}{\mathrm{d}t} = \frac{na}{r} + \frac{1}{nae}\left[a_R(\cos\theta - e) - a_S\left(1 + \frac{r}{a}\right)\sin\theta \right] \tag{3.4}$$

The disturbing accelerations a_R and a_S, although small, are suspected to no longer be negligible. This means the trapezoidal quadrature for the averaged effect of each orbital element will be slightly over or under exactly one revolution. Due to the sinusoidal behavior of the elements, this results in an interpreted secular effect, even if there are no actual secular or long-period variations present.

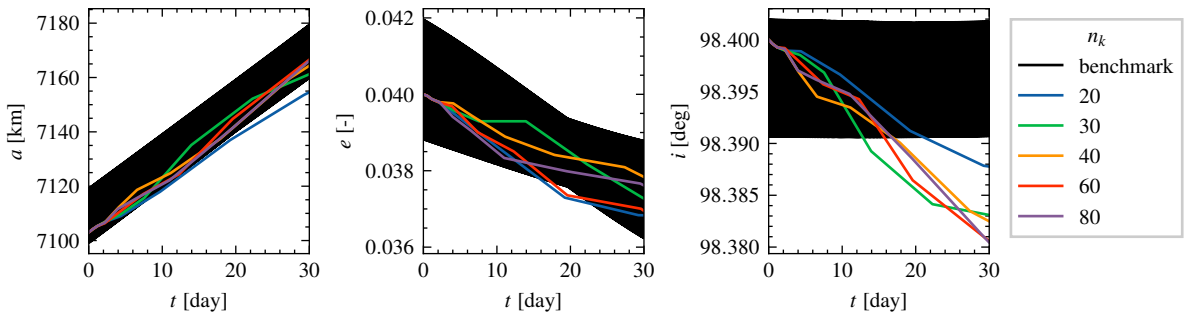

Figure 3.20: Propagation values obtained through OA overlaid on the amplitude range of the benchmark trajectory for the tangential-thrust case.

Nonetheless, because this effect is relatively small, i.e. for the example above about 5.0×10^{-5} deg per revolution, using the OA propagation for inclined LEO trajectories can still be considered valid. Furthermore, because this error is approximately equal in magnitude to the amplitude of the short-period variations, the impact of this error drift is limited, as the required final error constraints are generally larger than this boundary.

A suggested method for improving this behavior is by deriving analytical expressions for the *average* contribution of the non-spherical gravity field perturbations, instead of the fully numerical OA implementation in the OT. As this would require a fundamental restructuring of the methodology, it was decided to continue using the current approach as the error remained acceptable. However, when more predictable error behavior is desired or higher accuracy requirements need to be used, it is recommended to rework the OA methodology by deriving analytical expressions for the averaged change due to Earth's gravity potential and then assuming constant orbital elements. As described in Section 2.3, this way n_k state derivatives can be evaluated over this constant orbit and numerically integrated using a trapezoidal quadrature to arrive at the averaged state derivatives. The analytically derived expressions for the gravity field perturbations are then simply added to these. This way, the short-period variations due to Earth's non-spherical gravity field, will not be interpreted as a secular effect, due to a small error in the approximation of the time-step conversion. Instead, the short-period variations are already discarded through the analytical approximation. For a derivation of this average perturbing potential, the reader is referred to Gómez-Jenkins (2015).

4

Transfer from GTO-to-GEO

One of the project goals set in advance of this thesis project was to improve and streamline the Hybrid Method based on Jimenez-Lluva (2017), including the novel coasting arc mechanism. This chapter aims to investigate the performance of the implemented method and compare its performance to the reference material of Jimenez-Lluva (2017) and previous authors.

The type of transfer trajectories studied is the category of GTO-to-GEO transfers. These trajectories were selected as they are a common problem in Earth-centered trajectory optimization, particularly due to their commercial applications. Furthermore, they were also studied by previous authors, allowing comparison with previous results. The first case is minimum-time GTO-to-GEO optimization as found in Jimenez-Lluva (2017), who based this case on the work by Geffroy and Epenoy (1997) and Sanchez and Campa (2014). As the work in this project is a continuation of the work done by Jimenez-Lluva (2017), this case aims to demonstrate the expected improved performance.

4.1. Minimum-Time GTO-to-GEO Transfer

4.1.1. Without Perturbations

The first minimum-time problem is considered in its simplest form: transfer trajectory starting from a slightly inclined GTO trajectory targeting GEO, without any perturbations. No perturbations are taken into account, as these were also not considered in the mentioned references. The initial and target conditions are given in Table 4.1.

Table 4.1: Initial and target Keplerian elements for minimum-time GTO-to-GEO optimization.

	a [km]	e [-]	i [deg]	Ω [deg]	ω [deg]	θ [deg]
initial state	24505.9	0.725	7.0	0	0	0
target state	42165.0	0	0	0	0	0

As discussed in Section 2.3, a single co-state arc is used, which means 11 parameters are optimized. For each case, OA propagation is used. The result is verified using a CI propagation, to ensure the errors are within the set boundaries. The number of segments $n_k = 40$ was chosen based on the analysis performed in Section 3.2. The error boundaries are also taken equal to the reference, i.e. $\varepsilon_a = 100\,\text{km}$, $\varepsilon_e = 0.01$ and $\varepsilon_i = 0.1$ deg, as discussed in Section 2.4. As the final trajectory is a non-inclined, circular trajectory, the RAAN and Argument of Periapsis (AOP) are not taken into account. Four runs of the optimization were performed to both ensure consistent convergence and prevent interpreting results as local optima. The population size N_p was set to 110 individuals, following the rule-of-thumb $N_p = 10D$ where D is the number of design parameters, i.e. 11 for the minimum-time problem. All other optimization parameters and settings are given in Table 4.2.

Table 4.2: Parameters for Case 1: Minimum-time GTO-to-GEO transfer trajectory.

	Parameter	Value
Propulsion	T [N]	0.350
	m_0 [kg]	2000
	I_{sp} [s]	2000
Simulation	Initial Epoch	01-01-2000, 12:00
	n_k [-]	40
	OA	yes
	ϵ_{abs}	10^{-3}
	ϵ_{rel}	10^{-3}
	initial step size [day]	1.0
	min step size [day]	0.1
	max step size [day]	10
	$t_{f,lower}$ [day]	100
	$t_{f,upper}$ [day]	150
Perturbations	J_2	no
	drag	no
	eclipse	no
Optimization	N_p [-]	$10D$
	N_{gen} [-]	2000
	w_a [-]	1.0
	w_e [-]	1.0
	w_i [-]	1.0
	w_Ω [-]	0.0
	w_ω [-]	0.0
	w_θ [-]	0.0
	w_{t_f} [-]	1.0
	w_m [-]	0.0

The initial epoch was arbitrarily set to J2000 (January 1st, 2000, 12:00), as thrust during eclipse conditions are not taken into account, and the initial epoch will not influence results. The bounds on the Time of Flight (TOF) were somewhat arbitrarily set to be between 100 and 150 days, based on an expected $t_f \approx 137$ days (Jimenez-Lluva, 2017). The number of generations is limited to 2000, although generally convergence is reached earlier as seen in Figure 4.1. This serves to limit the optimizer as no stopping mechanism has been implemented. Table 4.3 shows the TOFs found for each run and their corresponding final orbit errors, i.e. the difference with respect to the targets orbit given by Table 4.2.

Table 4.3: Results and final orbit error for four optimization runs for the minimum-time GTO-to-GEO transfer, without perturbations, for both the OA and CI propagations.

run		t_f [day]	m_{prop} [kg]	Δa [km]	Δe [-]	Δi [deg]
1	OA	136.503	210.462	0.5571	0.0062	0.0093
	CI	-	-	17.3777	0.0084	0.0004
2	OA	136.575	210.573	1.9234	0.0058	0.0039
	CI	-	-	94.7096	0.0080	0.0005
3	OA	136.585	210.588	1.2251	0.0058	0.0042
	CI	-	-	97.1021	0.0082	0.0006
4	OA	136.512	210.476	0.4015	0.0063	0.0018
	CI	-	-	88.3908	0.0086	0.0005

The results show a very good internal consistency in terms of found TOF, within 0.1 days of each other. This convergence consistency is also demonstrated by the progression of the fitness for each generation as shown in Figure 4.1. This is considered a good improvement over the reference method, Jimenez-Lluva notes allowed bounds of the TOF required incremental adjustment to arrive at a global optimum. This can be attributed to the co-state scaling mechanism and the SaDE algorithm. The optimal initial and final co-states found for each run are shown in Table 4.4. As seen, the co-states related to the semi-latus rectum (λ_p) are similar in magnitude to the other co-states. Additionally, while there are some differences between each solution, the obtained optimal co-states are similar. Recall, the co-states can be interpreted as being the relative importance of changing that specific element at some point in time, with respect to the other elements. In other words, their absolute magnitude is of little importance but their relative magnitudes are.

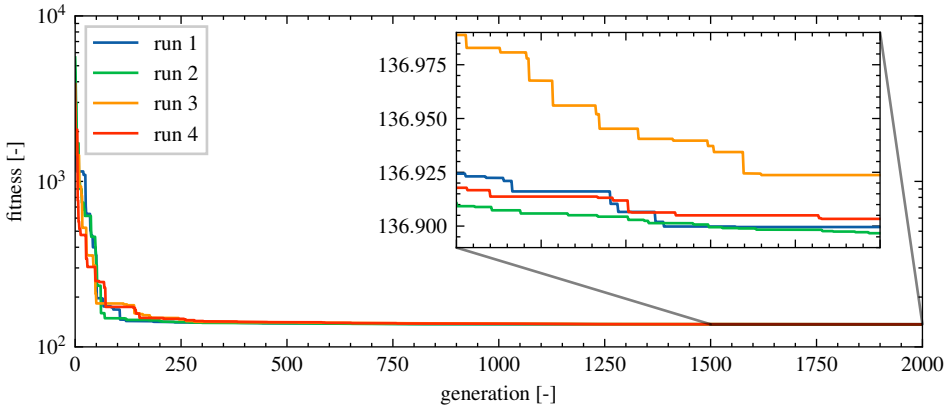

Figure 4.1: Fitness of each run, for each generation, for the GTO-to-GEO minimum-time optimization problem.

Table 4.4: Best initial and final co-states for four optimization runs for the minimum-time GTO-to-GEO transfer, without perturbations.

run		λ_p	λ_f	λ_g	λ_h	λ_k
1	$\boldsymbol{\lambda}_0$	−1690.48	−2572.20	103.34	1092.15	−113.92
	$\boldsymbol{\lambda}_f$	−1166.96	7993.65	−62.19	4840.60	148.24
2	$\boldsymbol{\lambda}_0$	−2036.57	−3342.74	−124.19	1348.97	−69.54
	$\boldsymbol{\lambda}_f$	−1181.06	9675.82	41.83	5491.69	38.83
3	$\boldsymbol{\lambda}_0$	−1931.62	−3224.31	−147.14	1608.70	90.93
	$\boldsymbol{\lambda}_f$	−1088.28	9162.13	49.29	4360.31	−157.65
4	$\boldsymbol{\lambda}_0$	−2033.02	−3236.36	−87.22	1298.97	−122.66
	$\boldsymbol{\lambda}_f$	−1142.04	9493.38	23.71	5593.87	108.74

Surprisingly, when compared to results obtained by previous authors, the results obtained by the OT show a slightly improved result in terms of TOF of approximately 1 day, i.e. approximately one orbital revolution at t_f. This is less than the expected optimum of around 137.45 days as obtained by the reference methods, see Table 4.5.

Table 4.5: Summary of the best TOFs and propellant mass results obtained by previous authors for the minimum-time GTO-to-GEO optimization without perturbations.

	t_f [day]	m_{prop} [kg]
(Jimenez-Lluva, 2017)	137.45	211.91
Montealegre	137.41	211.86
Sanchez	137.5	212
(Geffroy and Epenoy, 1997)	137.5	212
This project	136.50	210.46

Because four independent references arrived at a best solution of approximately 137.5 days, the obtained results cannot directly be considered superior but might be attributed to a suspected difference in implementation. As the final orbit error of the CI propagated trajectories are within the boundaries, and thus yield similar fitness, albeit only marginally with a maximum error of 97.1 km, they are still considered feasible, i.e. a propagation using CI would have a similar fitness. Therefore this discrepancy cannot be attributed to the OA approximation. Furthermore, as no perturbations are taken into account, their implementation will also not impact the obtained solutions. Nevertheless, the behavior of the obtained solutions will be discussed here to analyze and verify these solutions. The Keplerian elements versus time are shown in Figure 4.2 and behave as expected. During the early phase of the transfer, more emphasis is placed on changing the semi-major axis, moving to circularization during the later phases.

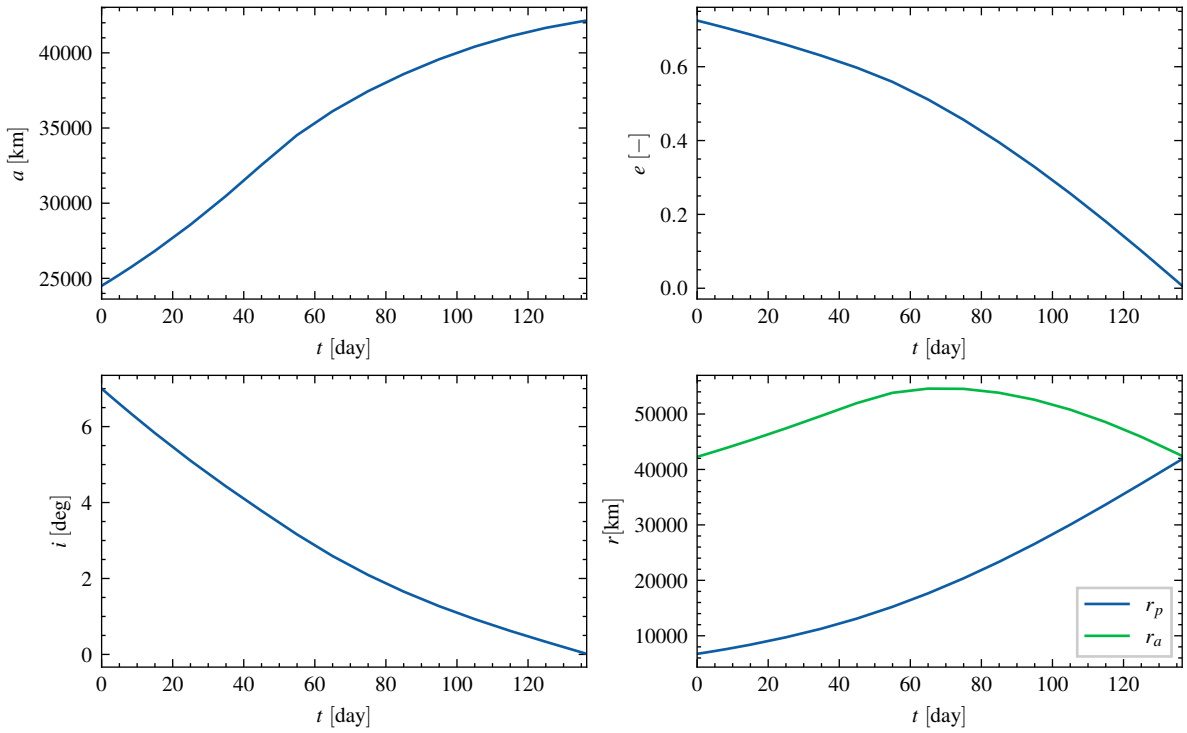

Figure 4.2: First three Keplerian elements and apogee, perigee radii versus time for run 1 solution of the minimum-time GTO-to-GEO transfer without perturbations.

The representation of the trajectory in Figure 4.3 also demonstrates this behavior. The color indicates the progression in time and shows the simultaneous increase in semi-major axis and decrease in eccentricity, evident as an increase and subsequent decrease of the apogee altitude.

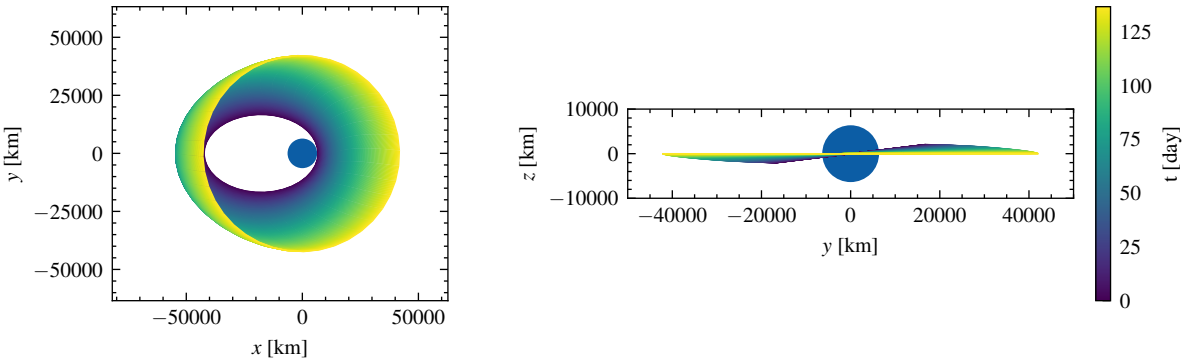

Figure 4.3: Transfer orbit representation of run 1 solution of the minimum-time GTO-to-GEO transfer without perturbations. Left: top-view, right: side view.

To further investigate the behavior of the OA technique and optimizer, a second GTO-to-GEO transfer was optimized, based on the work presented by Kluever (2010) and subsequently Boudestijn (2014) and Gómez-Jenkins (2015). This transfer will take into account the effect of zero thrust during eclipse conditions.

4.1.2. Including Eclipse Conditions

To investigate the influence of the eclipse conditions on the optimization results, a slightly different minimum-time GTO-to-GEO transfer is investigated. This case is based on the original OA implementation from Kluever (2010) and describes to transfer between GTO (28.5°) to GEO. Furthermore, the transfer takes into account a loss of thrust during eclipse conditions, and the initial orbit is chosen such that the apogee of the initial trajectory is in Earth's shadow. The initial and target Keplerian elements for the minimum-time GTO-to-GEO transfer are given in Table 4.6.

Table 4.6: Initial and target Keplerian elements for minimum-time GTO-to-GEO case in Kluever (2010).

	a [km]	e [-]	i [deg]	Ω [deg]	ω [deg]	θ [deg]
initial state	24364.0	0.7306	28.5	0	0	0
target state	42164.0	0	0	0	0	0

All settings and parameters used for the optimization are given in Table 4.7. The upper and lower boundary for the TOF were selected based on the expected time of flight of about 118 days (Kluever, 2010). The vehicle properties are chosen equal to the reference, where the thrust is obtained from the engine power and engine efficiency stated in the reference and using Equation (2.18). No perturbations are taken into account as they were not considered in the reference. Again, only the first three Keplerian elements are considered, as the target orbit is non-inclined and circular, making Ω and ω undefined. The initial epoch was given as March 22, 2000, at noon (12:00); at which point the apogee of the initial trajectory will be in Earth's shadow. All other optimization and simulation parameters remain equal to the previous case.

Table 4.7: Parameters for Case 1: Minimum-time GTO-to-GEO transfer trajectory.

	Parameter	Value
Propulsion	T [N]	0.31158
	m_0 [kg]	1200
	I_{sp} [s]	1800
Simulation	Initial Epoch	22-03-2000, 12:00
	n_k [-]	40
	OA	yes
	ϵ_{abs}	10^{-3}
	ϵ_{rel}	10^{-3}
	initial step size [day]	1.0
	min step size [day]	0.1
	max step size [day]	10
	$t_{f,lower}$ [day]	100
	$t_{f,upper}$ [day]	150
Perturbations	J_2	no
	drag	no
	eclipse	yes
Optimization	N_p [-]	$10D$
	N_{gen} [-]	2000
	w_a [-]	1.0
	w_e [-]	1.0
	w_i [-]	1.0
	w_Ω [-]	0.0
	w_ω [-]	0.0
	w_θ [-]	0.0
	w_{t_f} [-]	1.0
	w_m [-]	0.0

The best TOF and propellant mass m_p of each run are given in Table 4.8. Note there is not necessarily a direct connection between the time of flight and propellant mass, as this is now influenced by the time spent in shadow conditions. Still, the lowest t_f does correspond with the least amount of propellant used.

Table 4.8: Results for four optimization runs, for $\omega_0 = 0°$.

run	t_f [day]	m_{prop} [kg]	Δa [km]	Δe [-]	Δi [deg]
1	122.853	176.173	3.3043	0.0079	0.0495
2	118.375	170.270	16.3597	0.0018	0.0396
3	118.625	170.050	20.6081	0.0064	0.0389
4	116.560	168.026	4.9808	0.0039	0.0187

It is immediately clear there is a larger spread in obtained solutions, indicating that this specific case is susceptible to finding local optima, with the optimizer struggling to find a global optimum. This is suspected to be caused by the high sensitivity to eclipse conditions, with the OA approximation failing to accurately average and/or propagate the effects of eclipse conditions. To gain a better understanding of these local optima we can first inspect the progression of the Keplerian elements for runs 1, 2, and 4 (Figures 4.4 to 4.6). Run 3 was nearly identical to run 2 and therefore left out. While the eccentricity and inclination change similarly for each case and follow a similar pattern, the semi-major axis is distinctly different.

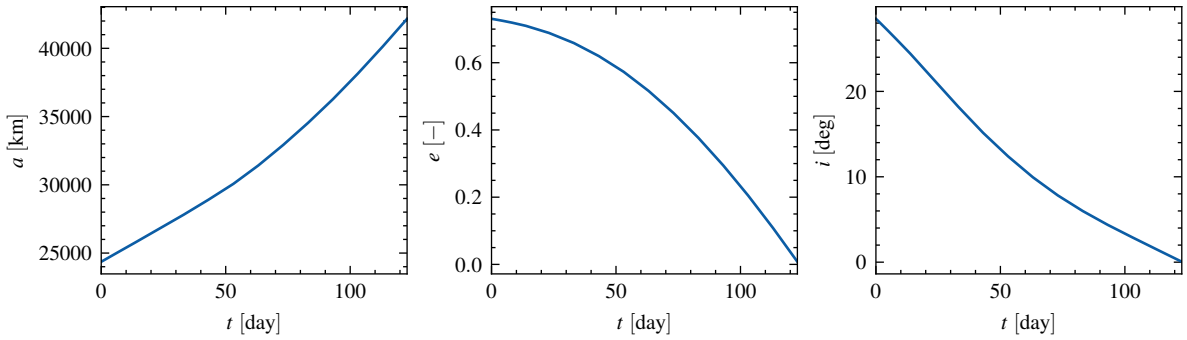

Figure 4.4: Semi-major axis, eccentricity and inclination versus time for the minimum-time GTO-to-GEO trajectory found by run 1.

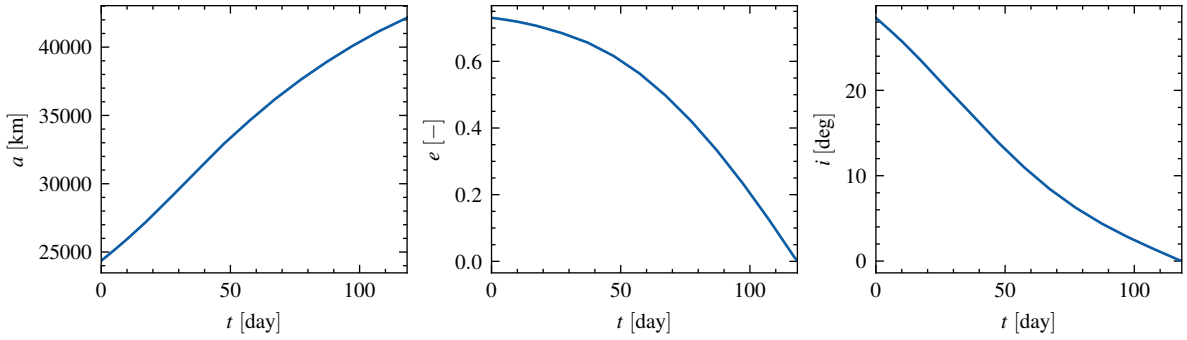

Figure 4.5: Semi-major axis, eccentricity and inclination versus time for the minimum-time GTO-to-GEO trajectory found by run 2.

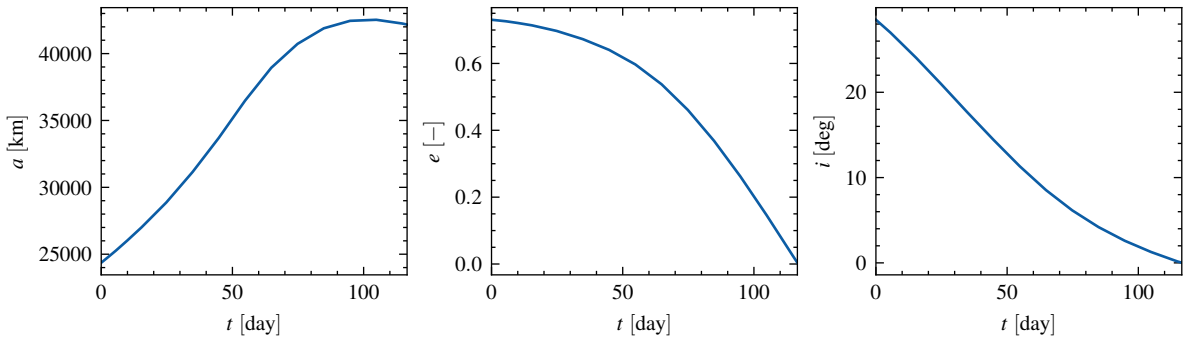

Figure 4.6: Semi-major axis, eccentricity and inclination versus time for the minimum-time GTO-to-GEO trajectory found by run 4.

The fourth run showed the smallest time of flight (Table 4.8). For this one, the semi-major axis changes most during the first part of the trajectory, after which most effort is spent circularizing and reducing the inclination. By looking at the maximum amplitude of the thrust steering angles α and β, in Figure 4.7 we see that the general pattern is the same. Around 50 days into the trajectory, the maximum pitch steering angle increases to 180 degrees, at which point thrust will be retrograde near perigee.

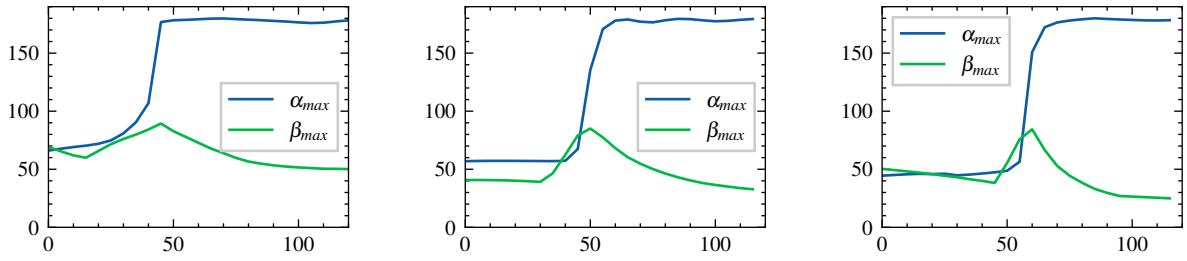

(a) Run 1 **(b)** Run 2 **(c)** Run 4

Figure 4.7: Maximum thrust steering angles for the first, second and fourth run.

To verify these results they can be compared to the results obtained by Kluever (2010), showing the progression of each orbital element in Figure 4.8 and the maximum steering angles in Figure 4.9. Note that the steering angle shown α in Figure 4.9 was defined with respect to the velocity vector (Kluever, 2010). Hence, the difference between the maximum amplitude of α Figure 4.7 and Figure 4.9 for the first part of the trajectory. The general pattern of the change in orbital elements and steering angles is similar. The maximum amplitude of α increases to 180° after approximately 50 days, at which point the maximum amplitude of β shows a peak.

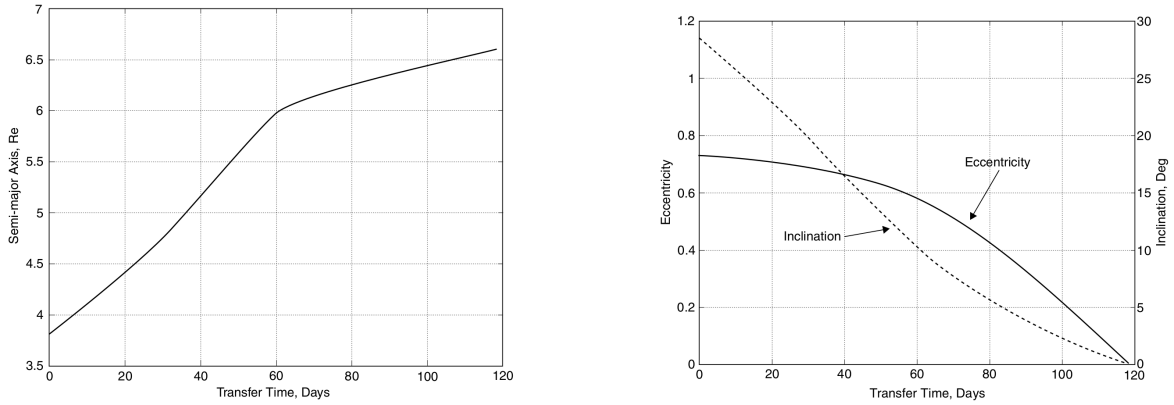

Figure 4.8: Semi-major axis, eccentricity and inclination versus time for the minimum-time GTO-to-GEO transfer trajectory found by Kluever (2010).

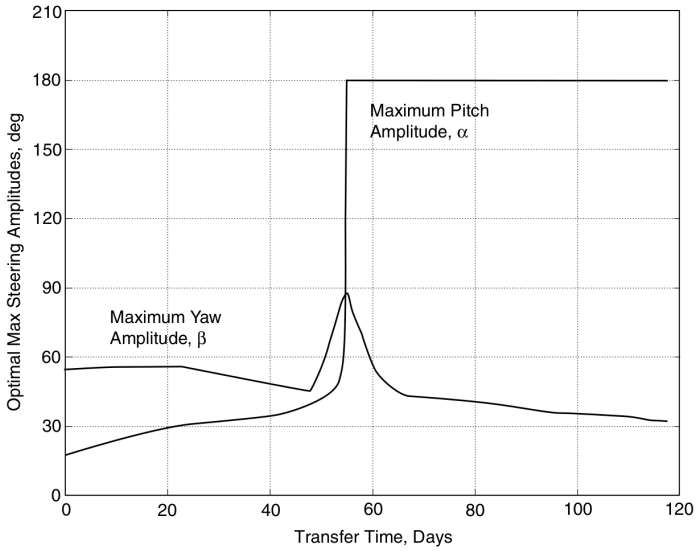

Figure 4.9: Maximum steering angle amplitudes for the minimum-time GTO-to-GEO transfer trajectory found by Kluever (2010).

In addition to the results obtained by the OT, there is also a large discrepancy in the results obtained by previous authors, summarized in Table 4.9.

Table 4.9: Summary of the results obtained by previous authors for a minimum-time GTO-to-GEO transfer optimization, including eclipses, with $\omega_0 = 0°$.

	t_f [day]	m_{prop} [kg]
(Kluever, 2010)	118.894	-
(Boudestijn, 2014)	114.294	174.307
(Gómez-Jenkins, 2015)	112.425	162.687
this project	116.560	168.026

This shows that the inclusion of thrust during eclipse conditions, especially for a worst-case scenario such as an apogee in shadow, complicates the optimization problem. Therefore, an additional case was run by Kluever (2010) and Boudestijn (2014), where the initial argument of perigee ω_0, was changed to 180°. This corresponds to an initial orbit where perigee is in Earth's shadow. All other parameters remain the same. For this case, the results obtained as shown in Table 4.10 show better accordance with reference results, as summarized in Table 4.11.

Table 4.10: Results for four optimization runs, for $\omega_0 = 180°$.

run	t_f [day]	m_{prop} [kg]	Δa [km]	Δe [-]	Δi [deg]
1	113.060	162.273	10.5616	0.0028	0.0097
2	112.728	162.141	16.1517	0.0027	0.0069
3	112.682	161.961	7.2403	0.0036	0.0153
4	112.974	163.644	23.7307	0.0031	0.0449

Table 4.11: Summary of the results obtained by previous authors for a minimum-time GTO-to-GEO transfer optimization, including eclipses, with $\omega_0 = 180°$.

	t_f [day]	m_{prop} [kg]
(Kluever, 2010)	112.11	-
(Boudestijn, 2014)	112.63	171.76
this project	112.68	161.96

The obtained results by the OT show better consistency, both internally compared to each run, and compared to the reference results. Based on these results, we conclude that the additional consideration of thrust under eclipse conditions increases the likelihood of the optimizer converging to local optima, at least in its current implementation. Therefore the use of eclipse conditions will not be used in the remainder of this work. Although this limits the applicability of the method, it will yield better insights into the obtained solutions when convergence is guaranteed. Furthermore, because the obtained solutions for the second case, where eclipses play a smaller role, are consistent with the reference materials, the implementation is still considered valid. Nevertheless, it should be noted that more extensive testing will be required to ensure the validity of obtained solutions.

4.2. Minimum-Propellant with Coasting Arcs

The addition of a coasting arc mechanism in Jimenez-Lluva (2017) can be an attractive option for finding optimal minimum-propellant trajectories. This section briefly examines the obtained results and the influence of the implemented enhancements. Although the coasting arc mechanism was a primary focus of this project, its inclusion in Tudat is a valuable addition. Therefore this section aims to demonstrate the coasting arc performance for the minimum-propellant GTO-to-GEO trajectory optimization, following the implementation by Jimenez-Lluva (2017), but with the enhancements made in this project. To perform this comparison the same parameters as the reference material are used. Multiple optimizations were run for a fixed TOF; they were fixed at 150, 175, 200, 225, and 250 days. OA is again used to improve performance. The mass optimizer weight is set to 1000, to a ensure similar magnitude of the mass contribution to the cost function. All other parameters are given in Table 4.12.

Table 4.12: Parameters for minimum-propellant cases of the GTO-to-GEO transfer trajectory.
*: Adjusted to 175, 200, 225, 250 for each run.

	Parameter	Value
Propulsion	T [N]	0.350
	m_0 [kg]	2000
	I_{sp} [s]	2000
Simulation	Initial Epoch	01-01-2000, 12:00
	n_k [-]	40
	OA	yes
	ϵ_{abs}	10^{-3}
	ϵ_{rel}	10^{-3}
	initial step size [day]	1.0
	min step size [day]	0.1
	max step size [day]	10
	$t_{f,lower}$ [day]*	150
	$t_{f,upper}$ [day]*	150
Perturbations	J_2	no
	drag	no
	eclipse	no
Optimization	N_p [-]	$10D$
	N_{gen} [-]	1500
	w_a [-]	1.0
	w_e [-]	1.0
	w_i [-]	1.0
	w_Ω [-]	0.0
	w_ω [-]	0.0
	w_θ [-]	0.0
	w_m [-]	1000.0
	w_{t_f} [-]	0.0

The full results of each GTO-to-GEO minimum-propellant optimization run, for each t_f are given in Table 4.13. Additionally, the optima in terms of propellant mass, for each run, are plotted in Figure 4.10a and the results found by Jimenez-Lluva (2017) in Figure 4.10b, which also shows the theoretical analytical Pareto front based on his reference. Because no factual reference of the numerical results was available, only a visual comparison is performed.

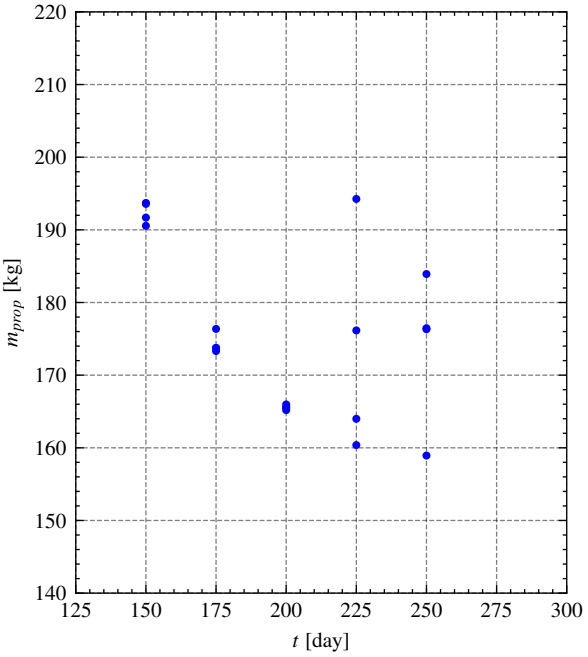

(a) Scatter plot of all propellant-optimal solutions for fixed TOFs

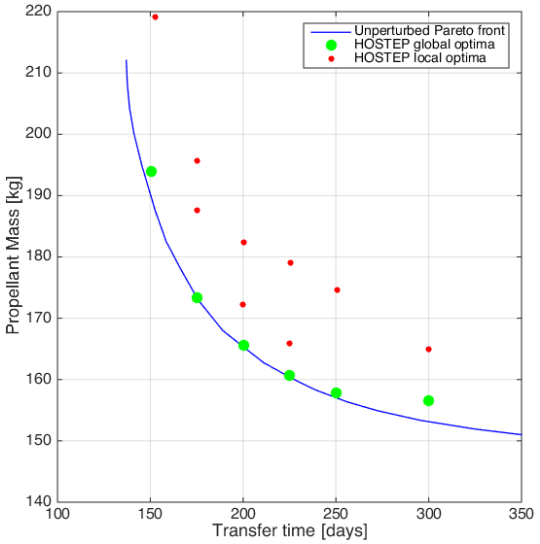

(b) Scatter plot of all propellant-optimal solutions for fixed TOFs

Figure 4.10: Resulting propellant masses obtained in this project and those in Jimenez-Lluva (2017)

Table 4.13: Results of all GTO-GEO minimum propellant optimization runs

t_f [day]	m_{prop} [kg]	Δa [km]	Δe [-]	Δi [deg]
150	193.57	0.77	0.0099	0.0402
150	193.71	44.89	0.0130	0.0242
150	191.69	7.74	0.0075	0.0288
150	190.60	9.50	0.0123	0.0114
175	173.76	18.24	0.0074	0.0123
175	173.74	12.89	0.0059	0.0300
175	173.32	1.36	0.0049	0.0069
175	176.36	1.94	0.0014	0.0111
200	165.97	98.80	0.0100	0.1305
200	164.92	15.11	0.0108	0.0618
200	165.50	2.18	0.0079	0.0092
200	165.61	22.54	0.0045	0.0296
225	163.99	25.97	0.0112	0.1199
225	176.16	50.12	0.0065	0.0252
225	160.38	17.31	0.0018	0.0568
225	194.25	112.22	0.0091	0.0651
250	176.32	8.23	0.0078	0.0507
250	176.46	62.47	0.0102	0.0114
250	183.92	5.72	0.0098	0.0664
250	158.93	25.40	0.0031	0.0394

Surprisingly, the coasting behavior for the example 150-day trajectory, as shown in Figure 4.11, where the gray areas indicate coasting, is slightly different. As expected, the main coasting areas are near perigee, as raising perigee is most efficient near apogee. However, The coasting areas are distributed somewhat differently, with the implemented method yielding no coasting during later parts of the transfer, whereas the solution found by

Jimenez-Lluva (2017) includes coasting in each revolution, but with decreasing duration. Nonetheless, the progression of the orbital elements as shown in Figure 4.12 shows similar behavior: the apogee is initially raised, before being decreased to circularize the trajectory during the latter part of the transfer trajectory.

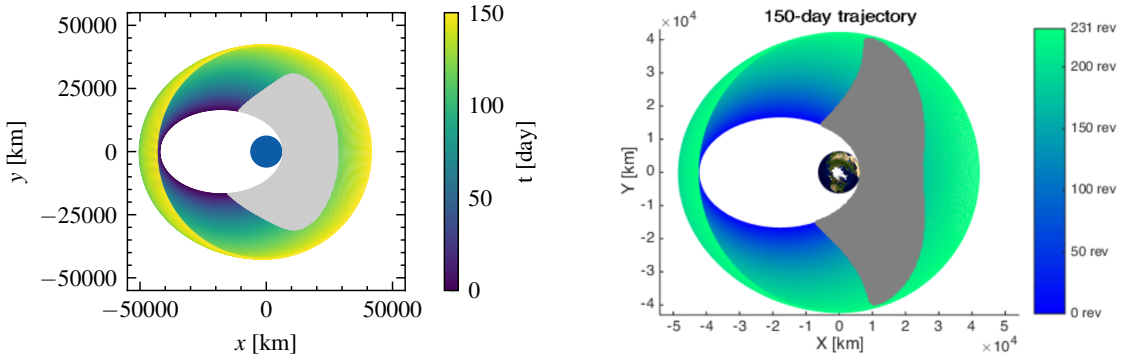

(a) This study **(b)** (Jimenez-Lluva, 2017)

Figure 4.11: Illustration of the coasting arcs for a 150-day GTO-to-GEO trajectory.

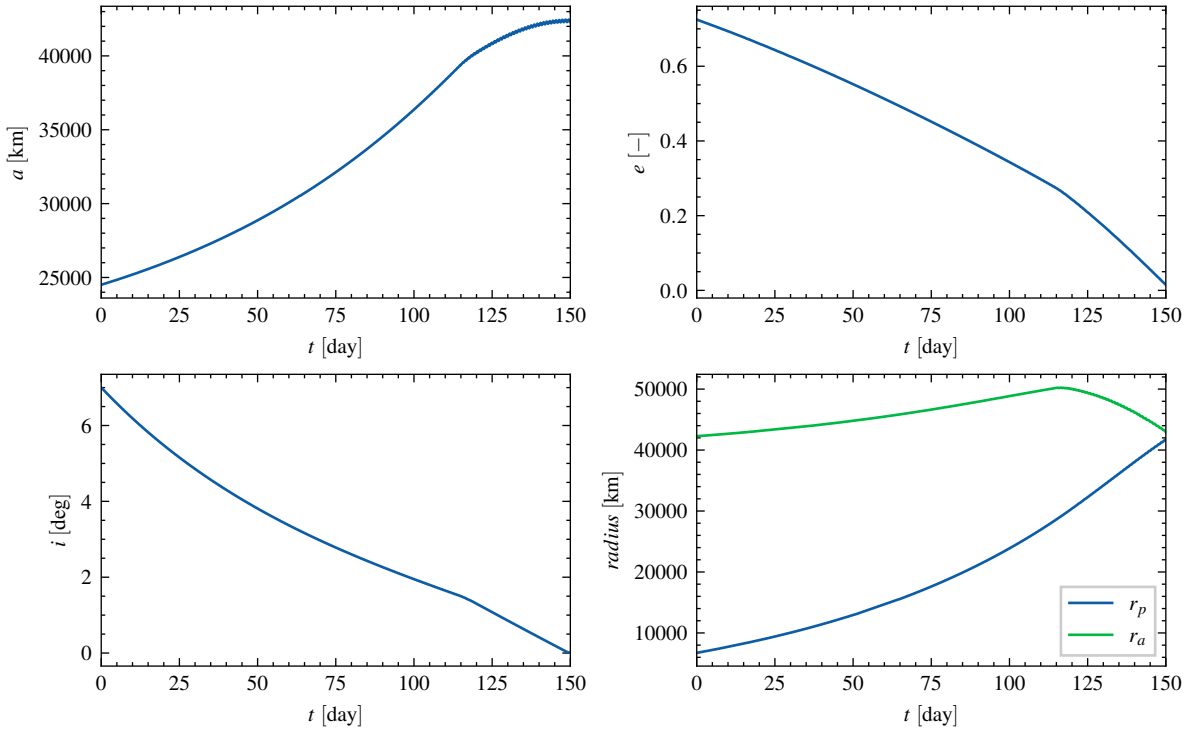

Figure 4.12: Progression of the semi-major axis, eccentricity, inclination, and perigee and apogee radii for fixed 150-day GTO-to-GEO trajectory.

It's important to note that based on the results in this study do not allow us to definitively conclude an improved performance over the reference implementation. Although better convergence was shown for transfers with a lower TOF, e.g. 200 days or less, this was not the case for transfers with longer flight times. Nevertheless, for each case, the OT was able to find solutions near the expected global optima, based on the reference material. As previously mentioned, the inclusion of coasting arcs was not a primary goal, but this result is considered promising as these results were again obtained without any manual tuning of parameters or tweaking of the implementation.

4.3. Conclusions

This chapter has investigated the GTO-to-GEO transfer problem and compared results to several reference results. The implementation of the minimum-time GTO-to-GEO case, as used by Jimenez-Lluva (2017), showed a significantly improved convergence behavior. No tuning of the TOF range was required to yield consistent results. However, the inclusion of the eclipse model, as was done in the initial implementation by Kluever (2010) and later in the work by Boudestijn (2014), showed a flawed behavior when its effect on the propagation was large. The author is confident that this flaw can be attributed to the difference in the specific implementation of the eclipse conditions, and not by the hybrid method, as the references obtained better results using a similar approach, i.e. switching thrust off during umbra. However, more work is needed to ensure the validity of the implementation, and therefore eclipse conditions are not be taken into account for the remaining optimization cases, to ensure consistency of the results. Additionally, because this problem arises for the worst-case scenario, it is not deemed a significant deficiency, as these conditions would be avoided.

The minimum-propellant case was also briefly discussed. Although ensuring acceptable behavior of the coasting arc mechanism was not the main focus of this project, its performance was already considered an improvement over the reference method. Nonetheless, for trajectories with a longer TOF, the optimizer had difficulty to consistently arrive at the expected global optimum, requiring multiple runs. Nevertheless, this result is still considered remarkable as it highlights the strengths of this method, no tuning or tweaking was done, and no good a-priori estimate is required. Furthermore, it is expected that some manual tuning of the co-state scaling and DE implementation can further improve convergence.

5

Space Debris Transfer

Ultimately the main motivation for this thesis work was to contribute to the tools available for the preliminary design of MADR missions. MADR remains one of the most promising options for reducing the space debris problem and can even be argued to become a necessity if stabilization of the debris population requires removal of at least five pieces of debris per year. Two general approaches for a MADR mission are identified: The first consists of a mothership carrying several 'de-orbit' packages, which attach themselves to a space debris object and perform a combined de-orbit maneuver. The second approach uses a single spacecraft which, after rendezvous with a particular debris object, attaches itself to this object and then transfers to a decay orbit. It will then detach itself and perform a transfer to the next debris object, repeating the process. The second approach is considered here, as currently the methods by which ADR will be performed, such as a tether system, would imply such an approach. For a more in-depth discussion on the space debris problem and ADR, the reader is referred to the literature survey (Klavers, 2020) accompanying this project.

In this chapter two transfer types are investigated. The first case is the most simple case: a transfer trajectory from an initial parking orbit to a debris object, with only a change in semi-major axis and a small change in inclination and eccentricity. The only perturbation taken into account is the J_2 effect, as the change in RAAN due to Earth's oblateness during the transfer is an important effect to consider. This case serves as a base to which the following cases can be compared. These cases will discuss the effect of adding an additional RAAN change to the maneuver, i.e. other than the natural drift. Additionally, the effect of atmospheric drag is considered, with the goal of demonstrating the benefits and limitations of the hybrid method for these types of transfer trajectory optimization problems. It is worth noting that we still only consider transfer trajectories between two specific orbits, as the rendezvous problem cannot be solved through the use of OA. First, Section 5.1 describes the design parameters used for the cases, including any assumptions made and their motivation. Section 5.2 describes the results obtained for the basic transfer optimization, and Section 5.3 the results of the more complex transfer problem.

5.1. Design Parameters

The transfer problem under consideration is the optimization of a low-thrust transfer trajectory, from an initial parking orbit in LEO, to a target object. The parking orbit is either the initial orbit after launch injection or interim de-orbit trajectory. From a mission design perspective, we can make several observations before defining the problem. Firstly, the required ΔV for changing semi-major axis and inclination, using a low-thrust propulsion system and assuming circular initial and target orbits, can be approximated using Edelbaum's approximation (Edelbaum, 1961):

$$\Delta V = \sqrt{v_0^2 + v_f^2 - 2v_0 v_f \cos\left(\frac{\pi}{2}\Delta i\right)} \tag{5.1}$$

where v_0 and v_f are the circular velocities of the initial and final trajectories, and Δi is the desired change in inclination. Because the ΔV, i.e. propellant mass, required for this specific transfer cannot be further reduced, the trajectory with the lowest TOF is consequently also the trajectory using the lowest amount of propellant. Because both target and initial orbits are near-circular, differences in eccentricity and argument of perigee can be

ignored for this first-order approximation analysis. However, the remaining element, RAAN, can be significantly different between possible target objects. Furthermore, due to the non-spherical distribution of Earth's gravity field, the RAAN will show a secular drift, as shown in Section 2.2.4.

This effect needs to be taken into account in two ways: Firstly, if we want to minimize TOF and propellant usage it is beneficial to select a target object such that no, or a small change in RAAN is required, whilst taking into account RAAN drift for both chaser and target during the transfer. Secondly, if two or more targets are fixed, and have a large difference in RAAN, a different mission strategy such as using a second interim drift orbit could be beneficial. This second case is not considered in this project, as this requires a different approach than the coasting arc mechanism in the hybrid method provides. A recent example is the line of research by Jorgensen and Sharf (2020), where optimal drift orbits for RAAN changes were investigated. Therefore, it is assumed that the target object can be chosen such that it will require a limited change in RAAN. Finally, it should be noted that through the use of OA only the transfer between initial and final orbit is considered, i.e. not the rendezvous problem.

5.1.1. Debris Selection

Candidate debris objects for removal can be selected based on several parameters, such as collision risk, orbital properties, mass, or size. Based on these properties clusters of debris, sharing common orbital elements such as altitude or inclination can be identified. Because plane-change maneuvers are expensive when compared to changing altitude and eccentricity it is desirable to focus on objects in the same inclination range. Figure 5.1 shows examples of these clusters, for the 500 objects with the largest target selection criteria, defined as a function of collision probability and object mass (Liou, 2011). Based on this analysis the SL-3 rocket bodies were selected as rendezvous candidates, which are derelict second stages of the Soviet Vostok launcher, about 2.6 m by 3.8 m and a dry mass of 1440 kg, orbiting at inclinations of around $i \approx 81.2°$ and altitudes ranging between approximately 750 and 950 km.

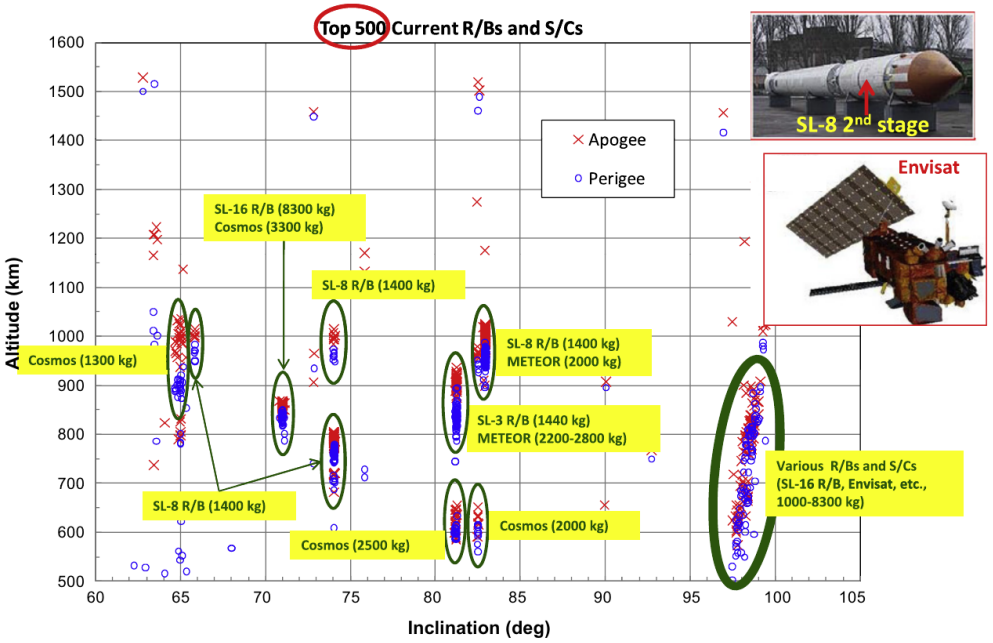

Figure 5.1: Perigee and apogee altitudes versus inclination for top 500 objects with the highest target selection criteria (Liou, 2011).

Because we only consider a single transfer in this project, the target object is the somewhat arbitrarily selected object SL-3 R/B with NORAD ID 6393. Its orbital parameters are given in Table 5.1:

Table 5.1: Initial orbital parameters for the target object, a derelict Vostok second stage.

NORAD ID	i [deg]	a [km]	e [-]
6393	81.25	7254.617	0.0057

For completeness sake, a full overview of possible target objects is given by Table 5.2. The (approximate) orbital elements can be obtained from the publicly available Two-Line Element set (TLE). Their format is described in Appendix B.2.

5.1.2. Assumptions

To simplify the problem several assumptions are made, which are discussed and motivated in this section. For each case, an initial parking orbit at an altitude of 200 km is assumed. It should be noted that a higher orbit is desired, as the orbital decay of objects at those altitudes is considerable and would require significant amounts of propellant when using a low-thrust propulsion system to counteract aerodynamic drag. However, this altitude was selected precisely for the considerable presence of aerodynamic effects, to analyze their effect on the optimization. At this altitude, the object will decay within several weeks[1], depending on solar conditions, whilst not requiring significant amounts of propellant for the chaser to maintain the orbit (Wertz, 2001).

The chaser maximum thrust is set to $T_{max} = 0.5$ N, a specific impulse of $I_{sp} = 2000$ s, the and initial mass is set to $m_0 = 2000$ kg; similar to those used for the GTO-to-GEO case and representative of modern electric propulsion platforms. The drag coefficient and frontal area are assumed constant and taken as $C_D = 4$, $A = 10\,\text{m}^2$. In reality, both drag coefficient and frontal area can vary significantly depending on the orientation of the chaser. The inclusion of drag serves to understand its impact on the optimization; for a full scenario both attitude and vehicle shape will need to be taken into account, as well as a more accurate atmospheric model. The requirements on the final orbit error are lower than for the GTO-to-GEO case and are given in Table 5.3, based on the expected OA error, as discussed in Section 3.2. The number of segments was increased to $n_k = 60$ to accurately capture the perturbing effects. Finally, as discussed in Chapter 4, thrust under shadow conditions is not considered. All parameters are given in Table 5.4.

Table 5.3: Upper bound of final orbit error for the space debris transfer case.

element	**Upper Bound**
a [km]	10.0
e [-]	0.001
i [deg]	0.01
Ω [deg]	1.0

[1] Based on $C_D \approx 2.7$ for a cylindrical shape and a frontal area of $10\,\text{m}^2$

Table 5.4: Parameters for space debris transfers.

	Parameter	Value
Propulsion	T [N]	0.50
	m_0 [kg]	2000
	I_{sp} [s]	2000
Simulation	Initial Epoch	01-01-2000, 12:00
	n_k [-]	60
	OA	yes
	ϵ_{abs}	10^{-3}
	ϵ_{rel}	10^{-3}
	initial step size [day]	1.0
	min step size [day]	0.1
	max step size [day]	10
	$t_{f,lower}$ [day]	0
	$t_{f,upper}$ [day]	100
Perturbations	J_2	yes
	drag	no
	eclipse	no
Optimization	N_p [-]	$10D$
	N_{gen} [-]	500
	w_a [-]	1.0
	w_e [-]	1.0
	w_i [-]	1.0
	w_Ω [-]	1.0
	w_ω [-]	0.0
	w_θ [-]	0.0
	w_{t_f} [-]	1.0
	w_m [-]	0.0

5.1.3. RAAN Drift

For the selection of a rendezvous target object, an additional limitation needs to be taken into consideration. As shown in Section 2.2.4, the oblateness of the Earth causes a drift in RAAN Ω. The change in RAAN that can be obtained by active orbit control is limited by the propulsion system. These two effects imply there is a limit on the obtainable orbits, from a given initial orbit, depending on inclination, semi-major axis, and TOF. When assuming a transfer between two near-circular trajectories, which is valid for the initial parking orbit and debris target objects in Sun-Synchronous Orbit (SSO), an approximation can be found for this RAAN range.

The secular drift of Ω for a circular orbit due to oblateness follows from Equation (2.21) and is:

$$\dot{\Omega}_{J_2} = -\frac{3}{2} n J_2 \left(\frac{R_E}{a}\right)^2 \cos i \tag{5.2}$$

The maximum change in Ω due to thrust is obtained from the planetary equations Equation (2.11e), again under the assumption of a circular trajectory:

$$\dot{\Omega}_T = a_W \frac{a \sin\theta}{H \sin i} \tag{5.3}$$

where $H = \sqrt{\mu p}$ and $a_W = (T/m)\sin\beta$. So to maximize the change in Ω it follows that $\beta = (\pi/2)\,\mathrm{sgn}(\sin\theta)$. The minimum and maximum obtainable RAAN can be approximated:

$$\Delta\Omega_{max} = \Delta\Omega_{J_2} \pm \Delta\Omega_T \tag{5.4}$$

This approximation can be obtained by numerically integrating the combined effect of $\dot{\Omega}_{J_2}$ and $\dot{\Omega}_T$ from t_0 to t_f, assuming the semi-major axis and inclination change linearly during the transfer. t_f follows from Edelbaum's approximation (Equation (5.1)) and the ideal rocket equation:

$$\Delta V = g_0 I_{sp} \ln \frac{m_0}{m_f} \tag{5.5}$$

as thrust and I_{sp} are assumed constant:

$$\dot{m} = -\frac{T}{g_0 I_{sp}} = \frac{m_0 - m_f}{t_f} \tag{5.6}$$

5.2. Case 1: Co-planar transfer without RAAN change

The initial and final Keplerian elements for the basic transfer case are given by Table 5.5.

	a [km]	e [-]	i [deg]	Ω [deg]
initial state	6579.0	7.0e-4	81.15	0
target state	7254.617	0.0057	81.25	-19.5467

Table 5.5: Initial and target Keplerian elements for a basic chaser to target transfer

The small difference in inclination and eccentricity accounts for injection errors and is simply twice the standard deviation of the injection error of the Ariane 5 launcher for a typical SSO (Arianespace, 2016). The target RAAN is obtained by using the approximation described in the previous section. The range of obtainable RAANs is shown in Figure 5.2. This approximation is valid for finding the natural change in Ω due to J_2 in order to minimize the required thrust for changing the RAAN. The expected t_f and m_{prop} are then given in Table 5.6:

Table 5.6: Expected time of flight and propellant mass based on analytical analysis.

time of flight t_f [day]	**propellant mass** m_{prop} [kg]
17.05	37.56

In Figure 5.2 the solid line can be interpreted as the natural drift due to J_2, the shaded area then represents the actual values of Ω that can be obtained due to thrust.

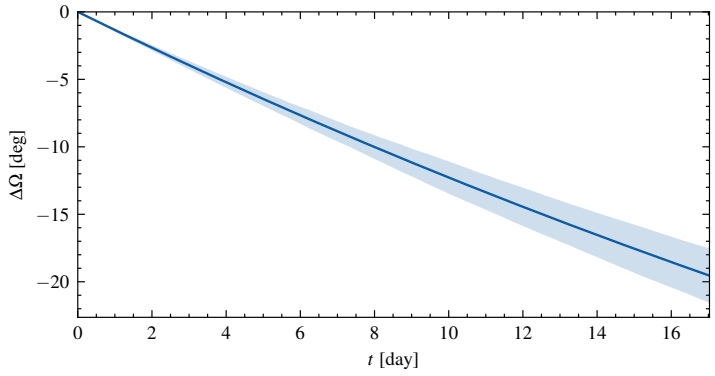

Figure 5.2: Approximation of the RAAN range obtainable for the given initial and target conditions.

Again, the optimization was run four times with different seeds, to ensure consistency and quality of the results. Table 5.7 shows the resulting t_f, m_{prop} and final orbit differences for the OA results and the CI verification runs.

Immediately, it is clear the results for the simple transfer case show great consistency, the best and worst results only differing by 0.12 days (0.17%).

Table 5.7: Results for four optimization runs

run		t_f [day]	m_{prop} [kg]	Δa [km]	Δe [-]	Δi [deg]	$\Delta\Omega$ [deg]
1	OA	17.097	37.657	0.5867	1.396×10^{-4}	9.175×10^{-4}	0.0047
	CI	-	-	20.0615	8.284×10^{-4}	2.000×10^{-3}	0.1607
2	OA	16.988	37.416	0.9275	2.405×10^{-4}	8.895×10^{-4}	0.0211
	CI	-	-	32.6779	2.469×10^{-3}	7.300×10^{-3}	0.1981
3	OA	17.040	37.531	0.3919	1.250×10^{-5}	7.496×10^{-4}	0.1528
	CI	-	-	10.3139	7.424×10^{-4}	8.900×10^{-3}	0.3393
4	OA	16.973	37.383	4.7461	2.284×10^{-5}	3.880×10^{-3}	0.2415
	CI	-	-	28.604	7.604×10^{-4}	2.400×10^{-3}	0.4004

A geometrical representation of the transfer is shown in Figure 5.3, clearly demonstrating the precession of the RAAN and the increasing semi-major axis. The color indicates the time, ranging from t_0 in blue, to t_f in yellow. When looking at the progression of the Keplerian elements in Figure 5.4 it is seen that the semi-major increases approximately linear. Furthermore, the small short-period variations of the inclination and eccentricity are clearly visible.

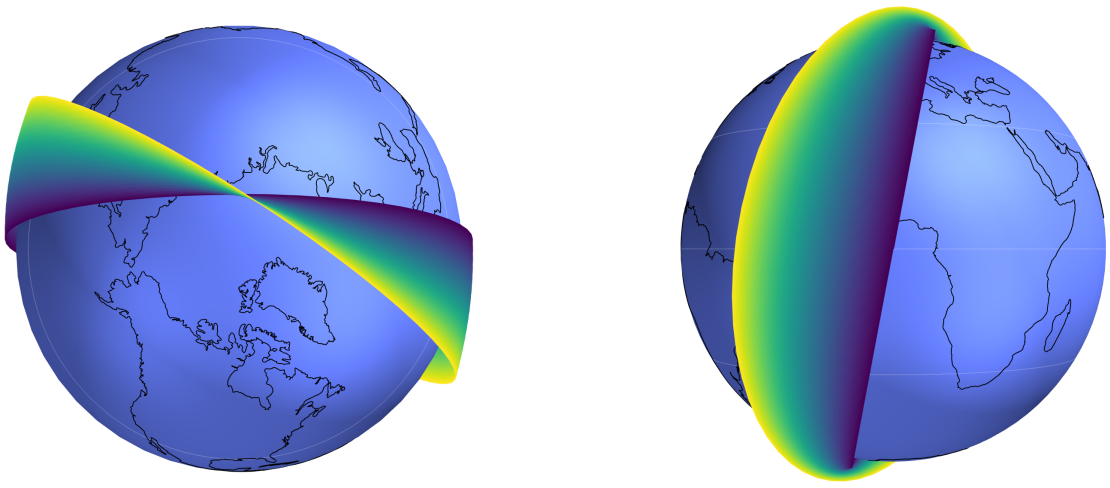

(a) Top view **(b)** side view

Figure 5.3: Representation of the optimal transfer trajectory found by run 1 of the simple debris transfer optimization, from t_0 (blue) to t_f (yellow)).

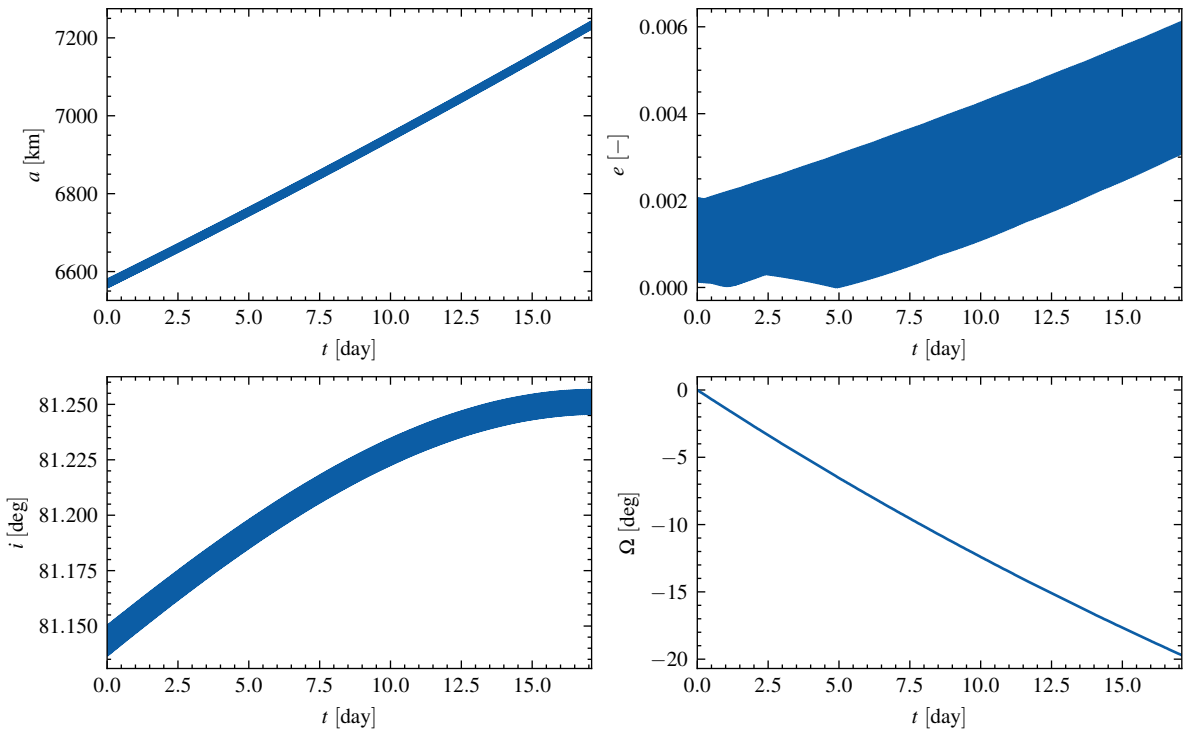

Figure 5.4: Progression of the semi-major axis, eccentricity, inclination and RAAN versus time for run 1 of the simple debris transfer.

This behavior is supported by the control history of the thrust acceleration, shown in Figure 5.5. The thrust is predominantly in the direction of velocity, which is expected for a co-planar transfer between two near-circular trajectories.

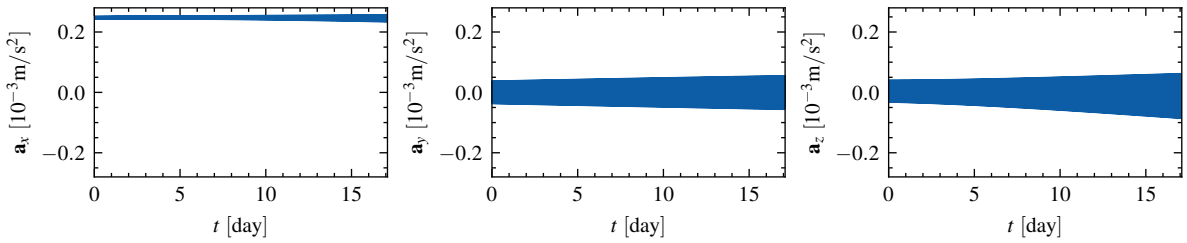

Figure 5.5: Thrust acceleration components in the NTW-frame

The best time-of-flight found was was 16.97 days, which is close to the approximated required time t_f = 17.05 days. While the optimization result for this problem is perhaps not surprising, it is worth noting that no additional tuning or tweaking of the OT was required. The process followed compared to the GTO-to-GEO was identical, with the most significant difference being adjustment of the final orbit error constraints. This case served as a baseline to which a more complex transfer problem can be compared against.

5.3. Case 2: Complex transfer with planar changes

The second case aims to investigate the performance of the optimizer for a more complex transfer problem. By starting from the same initial parking orbit, the transfer to a target object, requiring a plane change is considered. Additionally, the impact of aerodynamic drag is taken into account. The initial orbit is equal to the previous case but with a higher initial orbital altitude of 300 km. At lower altitudes the orbital decay would be too large, as illustrated by Figure 5.6; active low-thrust propulsion cannot compensate for this. The target orbit now requires a significant change in RAAN, as well as a small change in inclination of 2°. This case can for instance arise when

the next target object can not be selected based on the ideal transfer properties but is for example based on a general requirement for certain debris objects. The target and initial orbital elements are given in Table 5.8.

Table 5.8: Initial and target Keplerian elements for complex chaser to target transfer, with inclination and significant additional change in RAAN.

	a [km]	e [-]	i [deg]	Ω [deg]
initial state	6679.0	7.0e-4	79.25	0
target state	7254.617	0.0057	81.25	-45

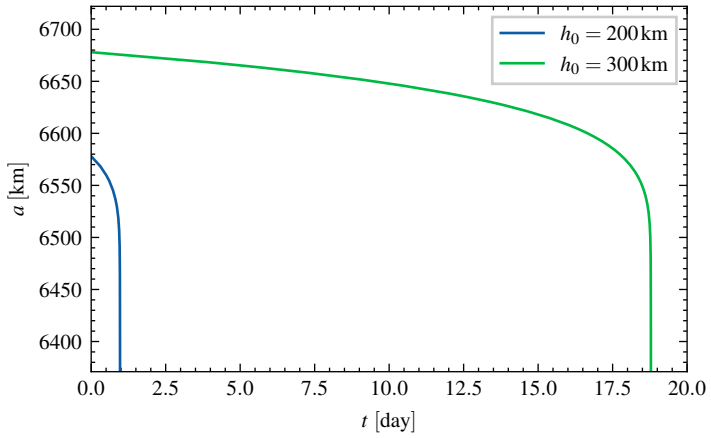

Figure 5.6: Illustration of the effects of aerodynamic drag on a trajectory with initial orbital height of 200 km and 300 km.

Again, four runs are done to test consistent behavior, and ensure the quality and reliability of the obtained solutions. Before investigating the simulation results, we expect a longer TOF to obtain the required additional change in RAAN and inclination. Furthermore, while the thrust vector for the previous case was almost entirely in line with the velocity, we now expect a larger out-of-plane component, as will be required to attain the required plane changes. The resulting errors, with respect to the target elements given by Table 5.8 are given by Table 5.9.

Table 5.9: Results and final orbit error for four optimization runs for the complex minimum-time debris transfer, for both the OA and CI propagations.

run		t_f [day]	m_{prop} [kg]	Δa [km]	Δe [-]	Δi [deg]	$\Delta\Omega$ [deg]
1	OA	34.407	75.784	3.0877	3.968×10^{-5}	1.479×10^{-3}	0.0026
	CI	-	-	41.8021	1.000×10^{-4}	2.990×10^{-2}	0.7306
2	OA	33.772	74.385	0.9929	8.025×10^{-5}	8.461×10^{-4}	0.0705
	CI	-	-	188.0963	4.727×10^{-3}	1.830×10^{-2}	2.5593
3	OA	34.292	75.531	3.2277	3.007×10^{-4}	2.008×10^{-3}	0.2624
	CI	-	-	41.4482	2.248×10^{-3}	1.590×10^{-2}	0.1220
4	OA	33.524	73.839	0.0293	7.337×10^{-5}	9.423×10^{-4}	0.7015
	CI	-	-	7.6056	2.900×10^{-4}	3.550×10^{-2}	0.3424

Firstly, it is immediately apparent that only a single run remains within the constraints. Three out of four runs show an error of the semi-major axis of 40 to 180 km. This error is attributed to the deficiency of the OA approximation. Because aerodynamic drag plays a significant role at these altitudes, an over-estimation of the altitude increase can quickly lead to an error accumulation. Additionally, as the eccentricity is increased throughout the first part of the transfer, the perigee altitude will drop, increasing the impact of the drag perturbation further. The author is

confident that this is not a flaw of the implemented optimization method, as the method demonstrates acceptable convergences to similar results, improving the OA approximation will yield more reliable results and is expected to further improve convergence. It is worth repeating that the CI error here is the difference between the target orbit and the trajectory propagated with CI, using the design vector obtained from the optimizer, which used OA. That is, the CI propagation verifies the feasibility of the obtained solution.

For the obtained best solution, run 4 (in terms of t_f), coincidentally showing the smallest CI error, the progression of the semi-major axis, eccentricity, inclination, and RAAN is shown in Figure 5.7. The figure shows the CI propagated trajectories, with the thickness of each lining indicating the magnitude of the short-period variations, most notably for the semi-major axis and inclination.

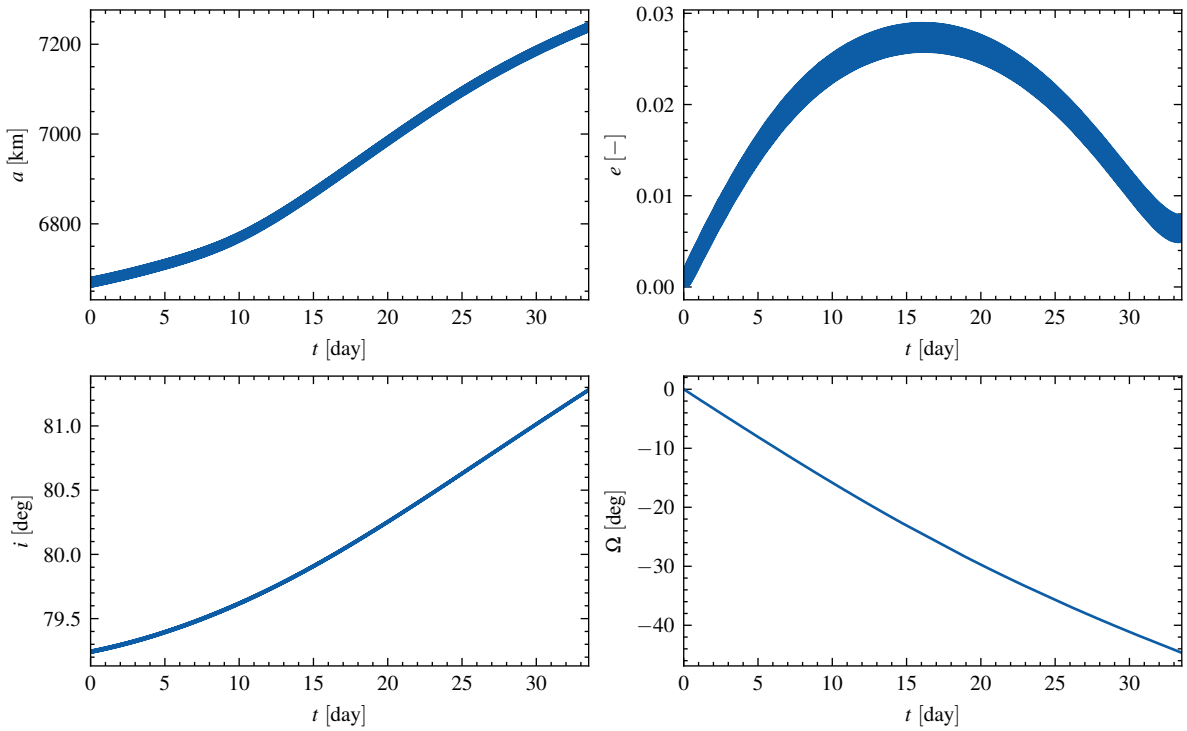

Figure 5.7: Progression of the semi-major axis, eccentricity, inclination and RAAN versus time for run 1 of the complex debris transfer.

Compared to the simple transfer, the change in semi-major axis is more gradual, and not linear. This can also be seen by looking at the components of the thrust accelerations in Figure 5.8, showing the magnitudes of each direction, in the NTW-frame. The thrust effort is both in-plane and out-of-plane, to achieve a simultaneous change of each element.

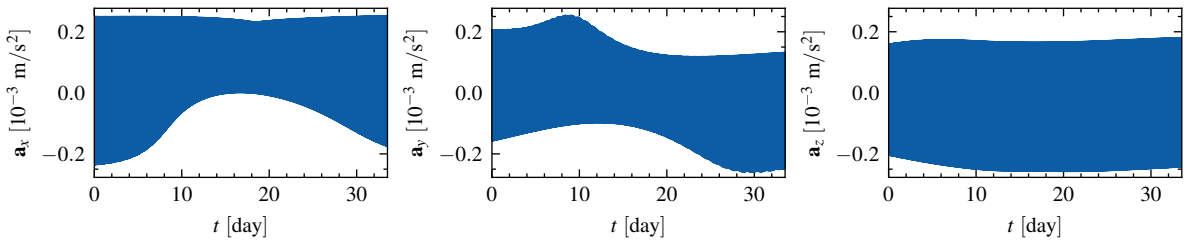

Figure 5.8: Thrust acceleration components in the NTW-frame.

5.4. Summary

This chapter detailed the trajectory optimization for a low-thrust trajectory, starting from a polar orbit in LEO to a target object. Two cases were considered: a simple co-planar transfer case, close to the analytical optimum, and a more complex transfer that included significant plane changes and additional orbital perturbations. The effect of the oblateness of the Earth on the mission design process was demonstrated by looking at the RAAN envelope, detailing the obtainable RAAN changes, assuming near-optimal trajectory transfers.

For the simple transfer case, the global optimum was reliably found, and the results are in accordance with the expected results based on an analytical approximation. The optimizer reliably converged for the more complex transfers, consisting of plane changes and taking into account aerodynamic drag. Nonetheless, the verification using CI propagation demonstrated an unacceptable error in semi-major axis for three out of four runs. This is caused by the OA approximation, because an over-estimation of the semi-major axis increase, combined with an increase in eccentricity, i.e. decrease in perigee altitude, leads to an under-estimation of the drag. This is not considered a flaw of the implementation method, and it is expected that improving the OA approximation accuracy will also improve the reliability of these cases.

Table 5.2: SL-3 R/B data currently in orbit

NORAD ID	i [deg]	a [km]	e [-]	h_a [km]	h_p [km]
877	65.08	7073.216	0.0079	751	639
13819	81.12	6895.267	0.0030	538	496
4814	81.14	6833.171	0.0024	472	439
12155	81.16	6842.407	0.0028	484	445
7493	81.16	7245.648	0.0083	928	807
14453	81.17	7187.453	0.0104	884	735
13771	81.17	6911.231	0.0046	565	501
13403	81.17	6921.863	0.0033	567	521
13154	81.18	6948.409	0.0039	597	543
12904	81.18	6926.211	0.0028	568	529
13121	81.18	6916.548	0.0016	549	527
13068	81.20	6921.380	0.0022	558	528
8294	81.21	7242.343	0.0106	941	787
11608	81.21	7250.841	0.0054	912	833
8846	81.22	7242.343	0.0039	892	836
7715	81.22	7248.481	0.0053	909	832
12646	81.23	7217.289	0.0067	887	791
5918	81.23	7251.785	0.0057	915	832
6660	81.23	7251.785	0.0048	908	839
7364	81.23	7250.841	0.0050	909	836
11822	81.23	6782.998	0.0008	410	399
4420	81.23	7230.530	0.0088	916	789
7575	81.24	7233.839	0.0049	891	820
7275	81.24	7248.953	0.0055	911	831
7210	81.24	7226.749	0.0080	906	791
4394	81.24	6850.664	0.0037	498	447
6080	81.24	7268.767	0.0048	926	856
10515	81.24	7241.870	0.0028	884	843
11289	81.24	7231.948	0.0076	909	799
11166	81.24	7224.384	0.0066	894	798
12465	81.24	6898.655	0.0034	544	497
6393	81.25	7254.617	0.0057	918	835
13719	81.25	7221.547	0.0070	894	793
8800	81.25	7237.146	0.0096	928	789
5732	81.25	7251.313	0.0052	911	836
6257	81.26	7249.425	0.0059	914	829
9904	81.26	7248.009	0.0054	909	831
5118	81.26	6898.655	0.0047	553	488
9482	81.26	7246.120	0.0086	930	806
12457	81.27	7247.065	0.0061	913	824
9662	81.28	7268.767	0.0053	929	852
8520	81.28	7240.926	0.0029	884	842
11963	81.28	7238.564	0.0076	915	805
8027	81.30	7246.593	0.0053	907	830
10114	97.37	6890.426	0.0012	521	504
19046	97.39	6935.866	0.0040	585	530
14208	97.45	6909.781	0.0038	558	505
16111	97.47	6718.425	0.0008	346	335
12586	97.66	6910.748	0.0017	544	521
18961	99.17	7269.710	0.0053	930	853
21689	99.34	7265.466	0.0026	906	868

6

Conclusions and Recommendations

This final chapter of the report will discuss the conclusions that can be drawn from the work presented, and outline recommendations for future work on this subject.

6.1. Conclusions

This section aims to answer the main research question as discussed in Chapter 1:

> *To what extent can a hybrid control parametrization optimization method, including Orbital Averaging (OA), be used to find optimal low-thrust transfer trajectories to space debris objects in Low Earth Orbit (LEO), with the ultimate purpose of enabling its use in Active Debris Removal (ADR) trajectory optimization?*

The hybrid optimization method, or control parametrization method, as presented by Jimenez-Lluva (2017) and based on work by previous authors such as Kluever (2010), Boudestijn (2014), and Gómez-Jenkins (2015), was implemented as part of the TU Delft Astrodynamics Toolbox (Tudat). The implementation was further developed, implementing several improvements in terms of accuracy and convergence. The optimization model was expanded with the additional aerodynamic drag perturbation in addition to the non-spherical gravity distribution and the absence of thrust in Earth's shadow.. Their implementation was tested for both CI and OA propagation, by comparing to benchmark trajectories and references in literature. However, it was found that the approximation used to convert from time to eccentric anomaly as independent parameter, was insufficient in the perturbed LEO environment.

The use of an adaptive integrator for the propagation of the averages used in OA decreased the number of function evaluations and fixed the deficiency of OA as observed by Jimenez-Lluva (2017). In addition to co-state scaling, the use of SaDE improved convergence, and further improved the flexibility of the method by reducing the manual tuning required. Nonetheless, it is expected that a properly tuned implementation of a well-chosen DE method, depending on the application, will show better behavior in terms of convergence speed as no time is spent by the optimizer 'tuning itself'. The performance of the implemented method was shown for the GTO-to-GEO transfer trajectories and compared to the reference results. This comparison showed the implementation of eclipse conditions was insufficient. However, the author is confident this is a deficiency of the implementation, not of the method, as the results obtained by Boudestijn (2014) and Gómez-Jenkins (2015) did not show this behavior. Nevertheless, to ensure consistent behavior, eclipses were turned off for the space debris transfer case.

A transfer from a parking orbit to a space debris object, in a polar LEO orbit, was modeled and optimized. A simple transfer, with parameters as close to an analytical optimum as possible, served as a baseline. The method reliably found the near-optimal results. Following this, a more complex case, including plane changes and aerodynamic drag was optimized. Consistent results were found. This highlights the remarkable properties of this method: With barely any manual tuning, a significantly different case compared to the GTO to GEO transfer can be optimized, yielding satisfactory results. No a-priori estimate is required, but good solutions are nonetheless obtained.

Based on this work, most research questions can now be answered. The use of SaDE improves convergence

and decreases manual tuning, at the cost of convergence speed. The use of variable-step integration for OA propagation decreases computational cost, at no cost of accuracy loss. The method successfully finds time-optimal Earth-centered many-revolution transfer trajectories to a space debris object, including relevant perturbations, answering the main research question.

> *Expand the Tudat low-thrust optimization suite with a novel hybrid optimization approach in order to improve optimization capabilities for the many-revolution problems, such that we can find optimal solutions for the multiple active space debris removal problem.*

In terms of project goals, the work presented in this document yields another powerful addition to the low-thrust trajectory design module of Tudat. Next to recent additions such as shape-based methods and the Sims-Flanagan trajectory model, the hybrid method provides an additional option to the toolbox. Although the large effort needed for the method implementation meant fully investigating the MADR problem was infeasible, the author is confident that this method provides a powerful option for generating near-optimal solutions for this category of transfer trajectories.

6.2. Recommendations

Based on the conclusions drawn from this project and the work done therein, several recommendations for future work are stated here.

Improve implementation, verification and validation of thrust shadow conditions

The implementation of eclipse conditions, their contribution to thrust in the OA propagation, was deemed flawed and insufficient for the optimization. The author recommends verifying its implementation and effect on the propagation in more detail, to ensure its reliability. When this reliability can be verified it is recommended to repeat the space debris transfer optimization with RAAN changes. Although many SSO trajectories are in constant dusk/dawn orbits, i.e. in near-permanent sunlight, this is not always true and will not be the case for derelict objects, implying trajectories that avoid shadow conditions can yield better results.

Improve OA performance for perturbed environments

The approximation used to determine a fixed step size in eccentric anomaly is suspected to be inaccurate for trajectories with relatively large short-period variations of the orbital elements. This would result in an apparent secular variation whereas the true trajectory shows only short-period variations. It is recommended to investigate this behavior in more detail and confirm this cause. This problem can be approached by either improving the time-step calculation, by taking into account the perturbing accelerations. A different approach is to derive expressions for the average effect of certain perturbations. Although this is not possible for every possible perturbation, this can be done for the J_2 effect. This would limit the flexibility of the method, as each additional perturbation required deriving averaged expressions for each.

Analyze rendezvous problems with enhancements

Because OA was used from the outset of this project, the problem of rendezvous was discarded at an early phase of the project, as the fast-changing element is lost. Nonetheless, the described enhancements are expected to improve the results for the geodetic longitude targeting. It is recommended to re-evaluate the minimum-propellant longitude targeting. Additionally, the space debris rendezvous problem should be considered. This problem contains the additional challenge of the simultaneous propagation of the target object, subject to perturbations.

Exploit PaGMO strengths

SaDE was used in the project with default settings, running each optimization single-threaded. It is recommended to further exploit the powerful options PaGMO provides, especially the generalized island model (Izzo et al., 2012), a method allowing parallel, asynchronous cooperative optimization. This is expected to further improve the performance of the optimizer.

Computational performance improvements

The author was limited by the Tudat environment, as well as working with an old version. Additionally, the focus of the implementation phase was not on computational performance but on results. Therefore, there is still a significant improvement possible in terms of computational speed. Several shortcuts were taken to ensure compliance with the existing Tudat code, which causes a lot of data to be shuffled around and additional unnecessary coordinate conversion.

Bibliography

Acton, C. H. (Jan. 1996). "Ancillary Data Services of NASA's Navigation and Ancillary Information Facility". In: *Planetary and Space Science* 44.1, pp. 65–70. ISSN: 00320633. DOI: 10.1016/0032-0633(95)00107-7.

Arianespace (Oct. 2016). *Ariane 5 User's Manual, Issue 5, Revision 2*.

Betts, J. T. (Aug. 2000). "Very Low-Thrust Trajectory Optimization Using a Direct SQP Method". In: *Journal of Computational and Applied Mathematics* 120.1-2, pp. 27–40. ISSN: 03770427. DOI: 10.1016/S0377-0427(00)00301-0.

Boudestijn, E. (Jan. 30, 2014). "Development of a Low-Thrust Earth-Centered Transfer Optimizer for the Preliminary Mission Design Phase". Master of Science Thesis. Delft University of Technology.

Brest, J. et al. (Dec. 2006). "Self-Adapting Control Parameters in Differential Evolution: A Comparative Study on Numerical Benchmark Problems". In: *IEEE Transactions on Evolutionary Computation* 10.6, pp. 646–657. ISSN: 1089-778X, 1089-778X, 1941-0026. DOI: 10.1109/TEVC.2006.872133.

Burden, R. L. and Faires, J. D. (2011). *Numerical Analysis*. 9th ed. Boston, MA: Brooks/Cole, Cengage Learning. 872 pp. ISBN: 978-0-538-73351-9.

Choueiri, E. Y. (Mar. 2004). "A Critical History of Electric Propulsion: The First 50 Years (1906-1956)". In: *Journal of Propulsion and Power* 20.2 (2), pp. 193–203. ISSN: 0748-4658, 1533-3876. DOI: 10.2514/1.9245.

Curtis, H. D. (2008). *Orbital Mechanics for Engineering Students*. 1. ed., reprinted. Elsevier Aerospace Engineering Series. Amsterdam: Elsevier/Butterworth-Heinemann. 673 pp. ISBN: 978-0-7506-6169-0.

Differential Evolution — Pagmo 2.17.0 Documentation (2021). URL: https://esa.github.io/pagmo2/docs/cpp/algorithms/de.html (visited on 07/05/2021).

Edelbaum, T. N. (Aug. 1961). "Propulsion Requirements for Controllable Satellites". In: *ARS Journal* 31.8, pp. 1079–1089. ISSN: 1936-9972. DOI: 10.2514/8.5723.

Elsayed, S. M., Sarker, R. A., and Essam, D. L. (June 2011). "Differential Evolution with Multiple Strategies for Solving CEC2011 Real-World Numerical Optimization Problems". In: *2011 IEEE Congress of Evolutionary Computation (CEC)*. 2011 IEEE Congress on Evolutionary Computation (CEC). New Orleans, LA, USA: IEEE, pp. 1041–1048. ISBN: 978-1-4244-7834-7. DOI: 10.1109/CEC.2011.5949732.

Gao, Y. and Kluever, C. A. (Nov. 2005). "Analytic Orbital Averaging Technique for Computing Tangential-Thrust Trajectories". In: *Journal of Guidance, Control, and Dynamics* 28.6, pp. 1320–1323. ISSN: 0731-5090, 1533-3884. DOI: 10.2514/1.14698.

Gao, Y. and Kluever, C. (Aug. 16, 2004). "Low-Thrust Interplanetary Orbit Transfers Using Hybrid Trajectory Optimization Method with Multiple Shooting". In: *AIAA/AAS Astrodynamics Specialist Conference and Exhibit*. AIAA/AAS Astrodynamics Specialist Conference and Exhibit. Providence, Rhode Island: American Institute of Aeronautics and Astronautics. ISBN: 978-1-62410-075-8. DOI: 10.2514/6.2004-5088.

Geffroy, S. and Epenoy, R. (Aug. 1997). “Optimal Low-Thrust Transfers with Constraints—Generalization of Averaging Techniques”. In: *Acta Astronautica* 41.3, pp. 133–149. ISSN: 00945765. DOI: 10.1016/S0094-5765(97)00208-7.

Gómez-Jenkins, M. (Feb. 24, 2015). “Optimization of Low-Thrust Trajectories in Earth-Centered Orbit”. Master of Science Thesis. Delft University of Technology.

Henry, C. (Aug. 22, 2017). “All-Electric Satellites Halfway to Becoming Half of All Satellites”. In: *SpaceNews Magazine* (July 3, 2017).

Izzo, D., Ruciński, M., and Biscani, F. (2012). “The Generalized Island Model”. In: *Parallel Architectures and Bioinspired Algorithms*. Ed. by F. Fernández de Vega, J. I. Hidalgo Pérez, and J. Lanchares. Vol. 415. Studies in Computational Intelligence. Berlin, Heidelberg: Springer Berlin Heidelberg, pp. 151–169. ISBN: 978-3-642-28788-6. DOI: 10.1007/978-3-642-28789-3_7.

Jimenez-Lluva, D. (July 2017). “Hybrid Optimization of Low-Thrust Many-Revolutions Trajectories with Coasting Arcs and Longitude Targeting for Propellant Minimization”. Master of Science Thesis. Delft University of Technology.

Jimenez-Lluva, D. and Root, B. (Dec. 2020). “Hybrid Optimization of Low-Thrust Many-Revolution Trajectories with Coasting Arcs and Longitude Targeting for Propellant Minimization”. In: *Acta Astronautica* 177, pp. 232–245. ISSN: 00945765. DOI: 10.1016/j.actaastro.2020.06.015.

Jorgensen, M. K. and Sharf, I. (July 2020). “Optimal Planning for a Multiple Space Debris Removal Mission Using High-Accuracy Low-Thrust Transfers”. In: *Acta Astronautica* 172, pp. 56–69. ISSN: 00945765. DOI: 10.1016/j.actaastro.2020.03.031.

Kawaguchi, J., Fujiwara, A., and Uesugi, T. (May 2008). “Hayabusa - Its Technology and Science Accomplishment Summary and Hayabusa-2”. In: *Acta Astronautica* 62.10-11, pp. 639–647. ISSN: 00945765. DOI: 10.1016/j.actaastro.2008.01.028.

Kechichian, J. A. (Jan. 1997). “The Treatment of the Earth Oblateness Effect in Trajectory Optimization in Equinoctial Coordinates”. In: *Acta Astronautica* 40.1, pp. 69–82. ISSN: 00945765. DOI: 10.1016/S0094-5765(97)00025-8.

Kessler, D. J. and Cour-Palais, B. G. (1978). “Collision Frequency of Artificial Satellites: The Creation of a Debris Belt”. In: *Journal of Geophysical Research* 83.A6, p. 2637. ISSN: 0148-0227. DOI: 10.1029/JA083iA06p02637.

Klavers, R. (Aug. 19, 2020). *Finding Optimal Low-Thrust Trajectories for Active Debris Removal*. Literature Survey. Delft University of Technology, p. 67.

Kluever, C. A. (2010). “Low-Thrust Trajectory Optimization Using Orbital Averaging and Control Parameterization”. In: *Spacecraft Trajectory Optimization*. Ed. by B. Conway. Cambridge: Cambridge University Press, pp. 112–138. ISBN: 978-0-511-77802-5. DOI: 10.1017/CBO9780511778025.006.

Kluever, C. A. and Pierson, B. L. (July 1995). “Optimal Low-Thrust Three-Dimensional Earth-Moon Trajectories”. In: *Journal of Guidance, Control, and Dynamics* 18.4, pp. 830–837. ISSN: 0731-5090, 1533-3884. DOI: 10.2514/3.21466.

Liou, J. C. et al. (2013). “Stability of the Future LEO Environment – an Iadc Comparison Study”. In: *6th European Conference on Space Debris*. 6th European Conference on Space Debris. Darmstadt, Germany.

Liou, J.-C. (June 2011). “An Active Debris Removal Parametric Study for LEO Environment Remediation”. In: *Advances in Space Research* 47.11, pp. 1865–1876. ISSN: 02731177. DOI: 10.1016/j.asr.2011.02.003.

Longuski, J., Guzmán, J. J., and Prussing, J. E. (2014). *Optimal Control with Aerospace Applications*. Space Technology Library. New York, New York : El Segundo, California: Springer ; Published jointly by Microcosm Press. 273 pp. ISBN: 978-1-4614-8944-3.

Markley, F. L. and Crassidis, J. L. (2014). *Fundamentals of Spacecraft Attitude Determination and Control*. New York, NY: Springer New York. ISBN: 978-1-4939-0801-1 978-1-4939-0802-8. DOI: 10.1007/978-1-4939-0802-8.

Martinez-Sanchez, M. and Pollard, J. E. (Sept. 1998). "Spacecraft Electric Propulsion-an Overview". In: *Journal of Propulsion and Power* 14.5 (5), pp. 688–699. ISSN: 0748-4658, 1533-3876. DOI: 10.2514/2.5331.

Michalewicz, Z. (1995). "A Survey of Constraint Handling Techniques in Evolutionary Computation Methods." In: *Evolutionary programming* 4, pp. 135–155.

Montenbruck, O. and Gill, E. (2000). *Satellite Orbits: Models, Methods, and Applications*. Berlin : New York: Springer. 369 pp. ISBN: 978-3-540-67280-7.

Pontryagin, L. S. (1987). *Mathematical Theory of Optimal Processes*. CRC press. ISBN: 2-88124-077-1.

Price, K. V., Lampinen, J. A., and Storn, R. M. (2005). *Differential Evolution a Practical Approach to Global Optimization*. Berlin, Heidelberg: Springer-Verlag Berlin Heidelberg. ISBN: 978-3-540-31306-9.

Racca, G. et al. (Dec. 2002). "SMART-1 Mission Description and Development Status". In: *Planetary and Space Science* 50.14-15, pp. 1323–1337. ISSN: 00320633. DOI: 10.1016/S0032-0633(02)00123-X.

Rayman, M. D. et al. (July 2000). "Results from the Deep Space 1 Technology Validation Mission". In: *Acta Astronautica* 47.2-9, pp. 475–487. ISSN: 00945765. DOI: 10.1016/S0094-5765(00)00087-4.

Sanchez, J. M. and Campa, A. (Jan. 26–30, 2014). "Automation of Multi-Revolution Low-Thrust Transfer Optimization via Differential Evolution." In: *AAS/AIAA Space Flight Mechanics Meeting*. AAS/AIAA Space Flight Mechanics Meeting. Vol. Volume 152. Santa Fe, New Mexico: Univelt.

Schlueter, M. et al. (June 2021). "GTOPX Space Mission Benchmarks". In: *SoftwareX* 14, p. 100666. ISSN: 23527110. DOI: 10.1016/j.softx.2021.100666.

Storn, R. and Price, K. (1995). *Differential Evolution - A Simple and Efficient Adaptive Scheme for Global Optimization over Continuous Spaces*. ICSI Technical Report TR-95-012. International Computer Science Institute, p. 12.

Storn, R. and Price, K. (1997). "Differential Evolution – a Simple and Efficient Heuristic for Global Optimization over Continuous Spaces". In: *Journal of Global Optimization* 11.4, pp. 341–359. ISSN: 09255001. DOI: 10.1023/A:1008202821328.

Sundaramoorthy, P. P. et al. (Sept. 8, 2010). "Two CubeSats with Micro-Propulsion in the QB50 Satellite Network". In: *Proceedings of the 24th Annual AIAA / USU Conference on Small Satellites*. 24th Annual AIAA /USU Conference on Small Satellites Period. Logan, Utah, USA: AIAA & Utah State University, p. 11.

Vallado, D. A. and McClain, W. D. (2001). *Fundamentals of Astrodynamics and Applications*. 2nd ed. Space Technology Library v. 12. Dordrecht ; Boston: Kluwer Academic Publishers. 958 pp. ISBN: 978-0-7923-6903-5.

Visser, H. (Jan. 2014). *AE4447 Aircraft Performance Optimization: Course Notes*. Delft University of Technology.

Wakker, K. F. (2015). *Fundamentals of Astrodynamics*. TU Delft Library. ISBN: 978-94-6186-419-2.

Walker, M. J. H., Ireland, B., and Owens, J. (Aug. 1985). “A Set Modified Equinoctial Orbit Elements”. In: *Celestial Mechanics* 36.4, pp. 409–419. ISSN: 0008-8714, 1572-9478. DOI: 10.1007/BF01227493.

Wertz, J. R. (2001). *Mission Geometry: Orbit and Constellation Design and Management ; Spacecraft Orbit and Attitude Systems*. Space Technology Library 13. El Segundo, Calif: Microcosm Press. 934 pp. ISBN: 978-1-881883-07-4.

Wertz, J. R., Everett, D. F., and Puschell, J. J., eds. (2011). *Space Mission Engineering: The New SMAD*. Space Technology Library v. 28. Hawthorne, CA: Microcosm Press. 1033 pp. ISBN: 978-1-881883-16-6.

A

Additional Verification Figures

A.1. SSO Trajectory

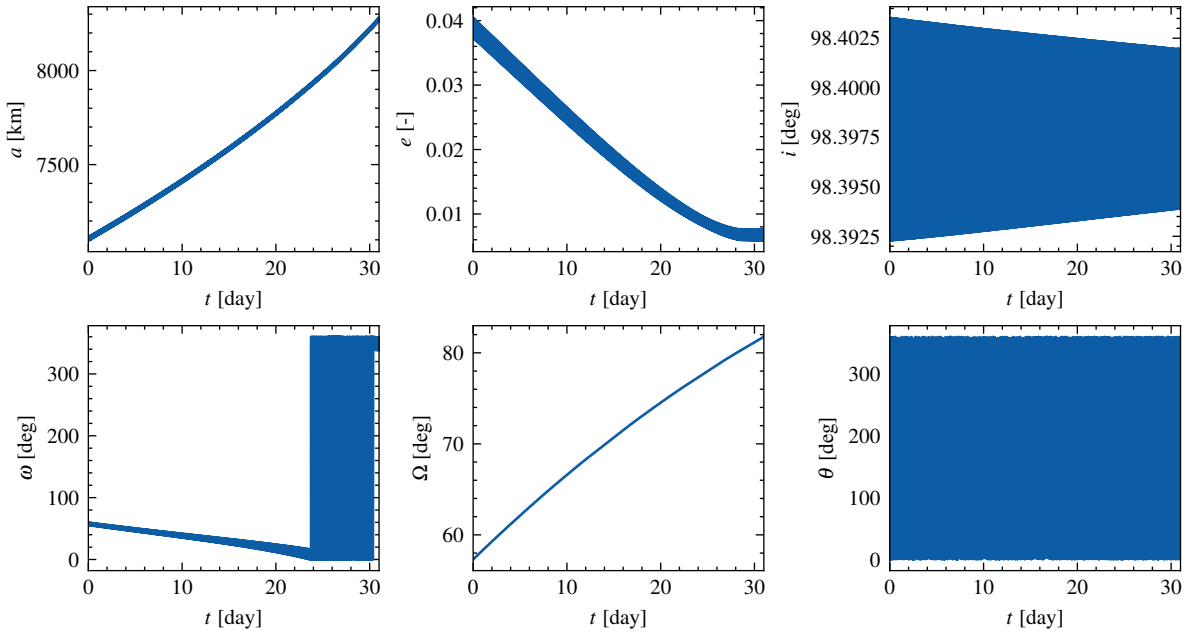

Figure A.1: Progression of the first three Keplerian Orbital Elements for tangential thrusting program.

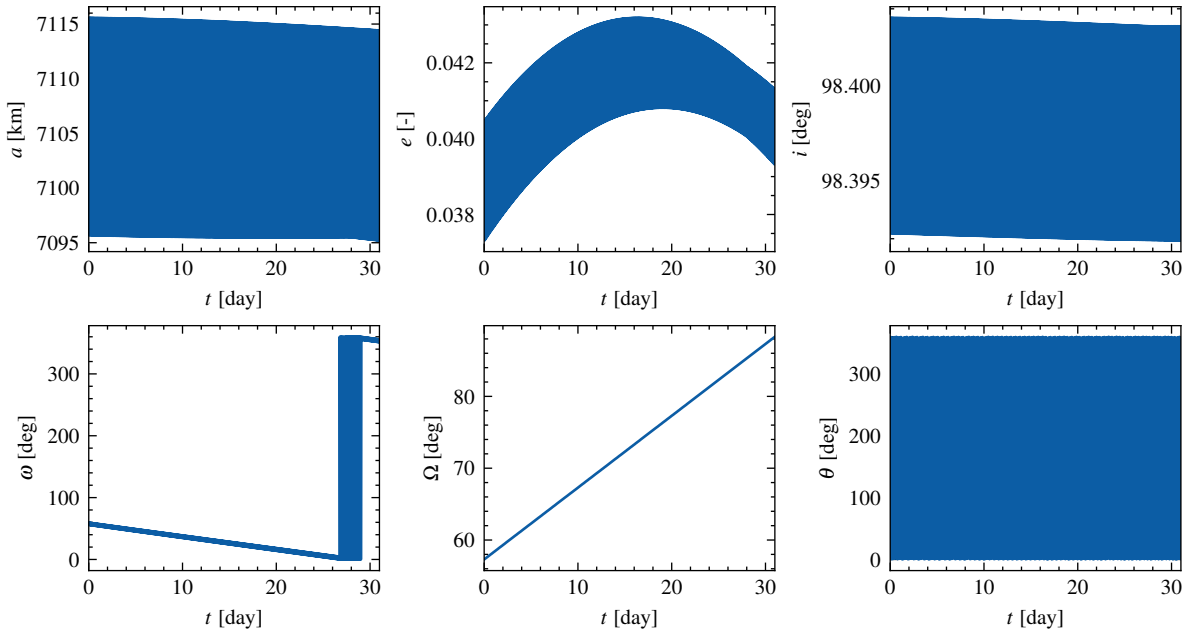

Figure A.2: Progression of the first three Keplerian Orbital Elements for radial thrusting program.

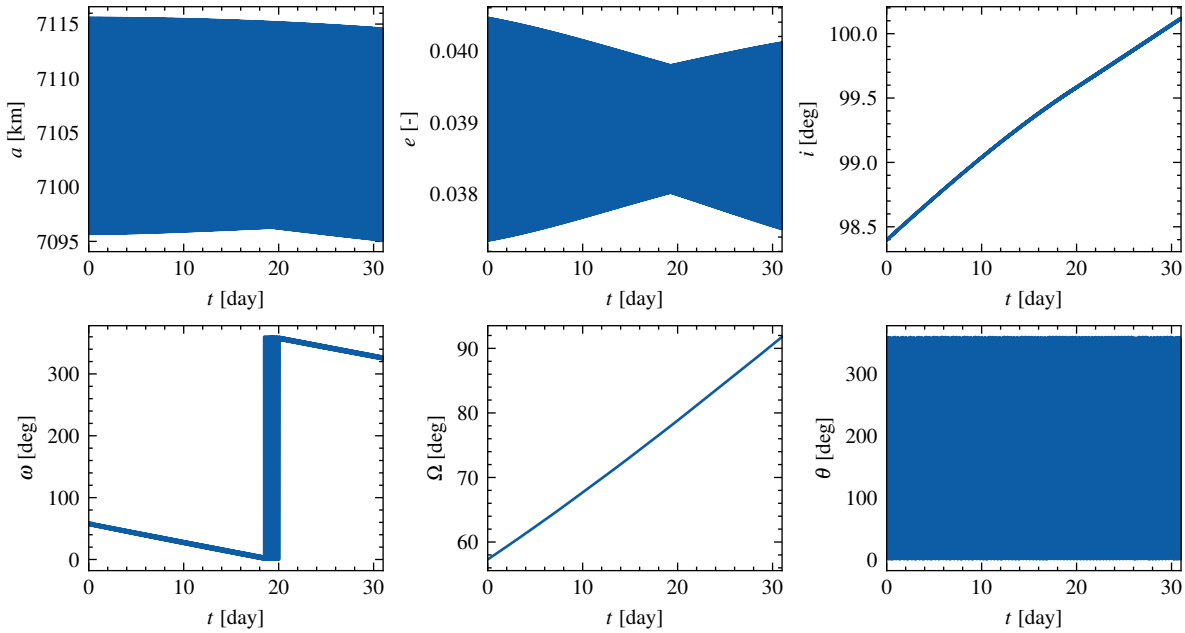

Figure A.3: Progression of the first three Keplerian Orbital Elements for out-of-plane thrusting program.

A.1.1. Error CI

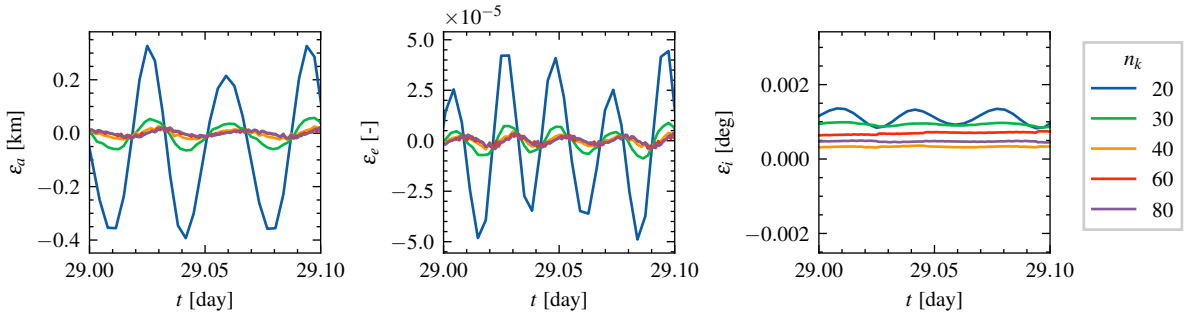

Figure A.4: Error between the CI propagation and benchmark trajectory for the out-of-plane thrust case.

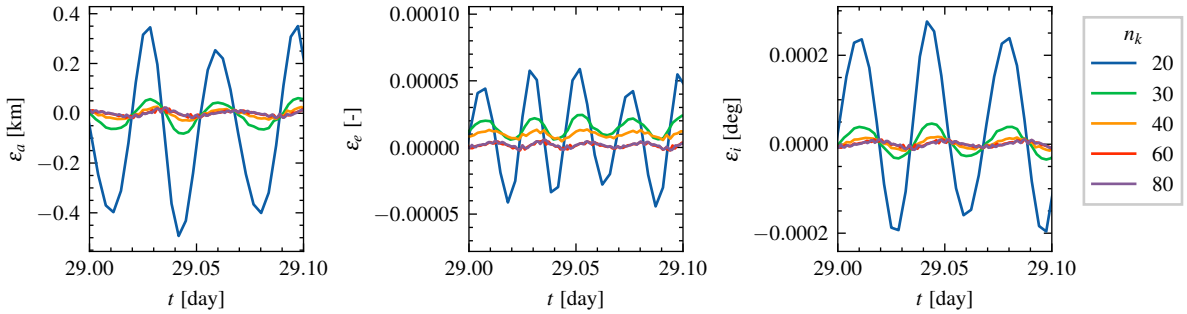

Figure A.5: Error between the CI propagation and benchmark trajectory for the radial thrust case.

A.1.2. Error OA

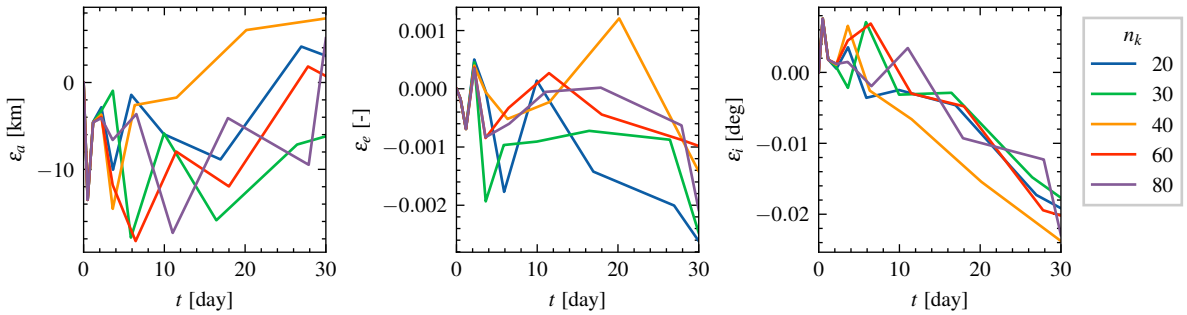

Figure A.6: Error between the OA propagation and benchmark trajectory for the out-of-plane thrust case.

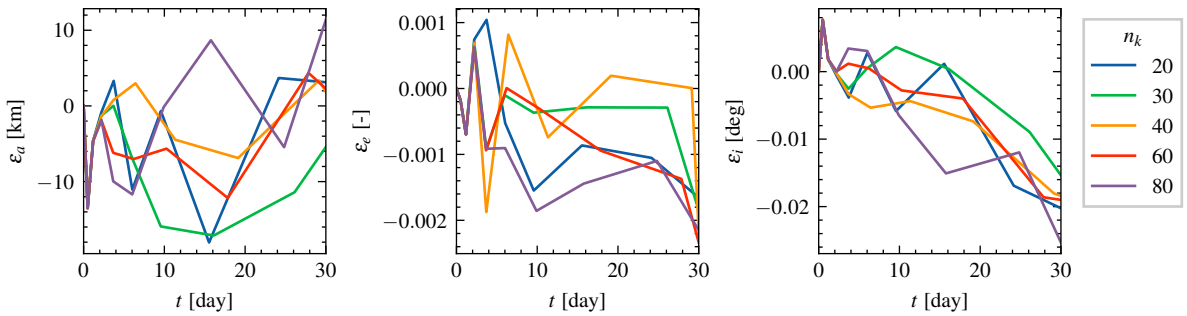

Figure A.7: Error between the OA propagation and benchmark trajectory for the radial thrust case.

A.2. Reference Results

A.2.1. OA Propagation Implementation comparison

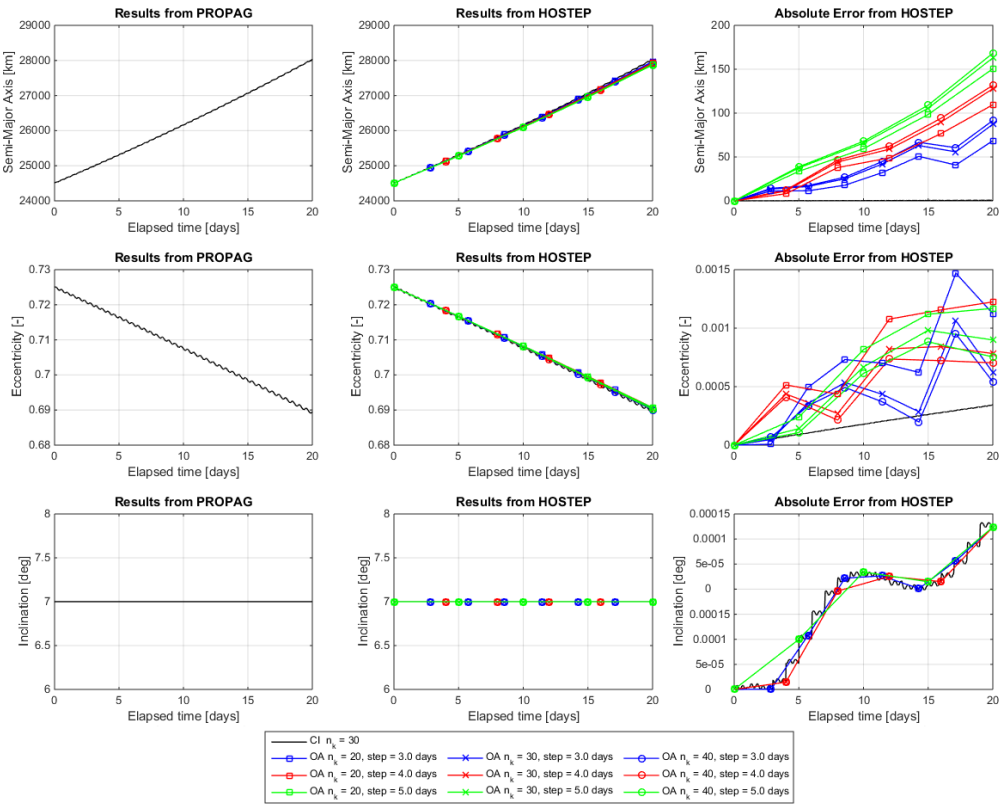

Figure A.8: Validation results of Jimenez-Lluva (2017) for the tangential thrust case

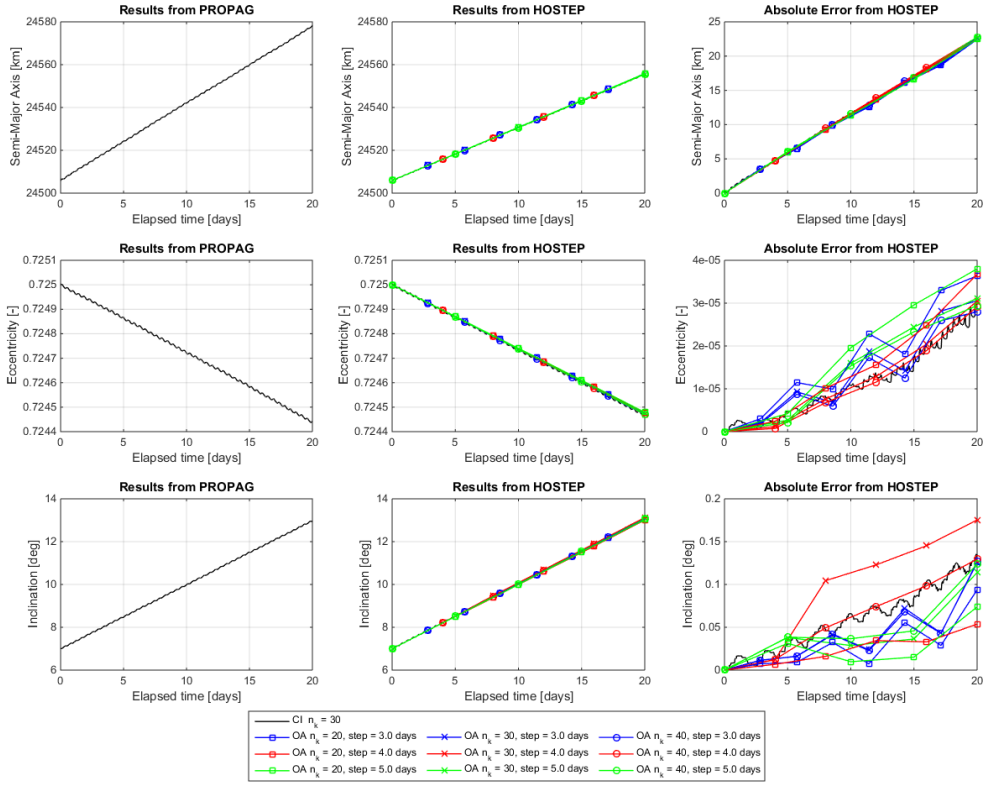

Figure A.9: Validation results of Jimenez-Lluva (2017) for the out-of-plane thrust case

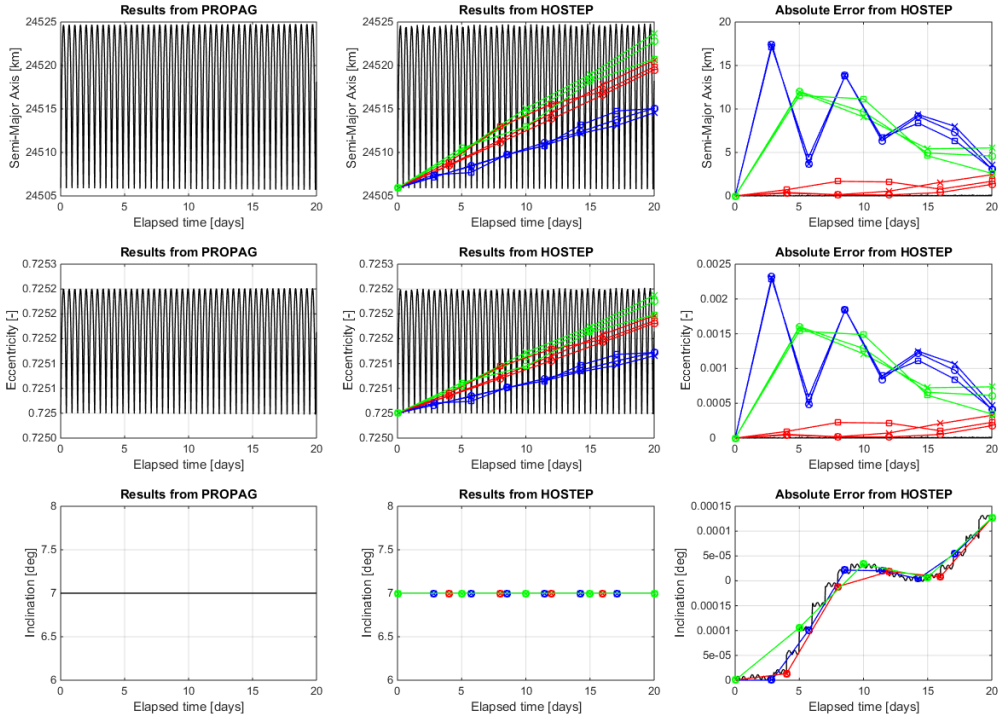

Figure A.10: Validation results of Jimenez-Lluva (2017) for the radial thrust case

A.2.2. GTO to GEO minimum propellant results

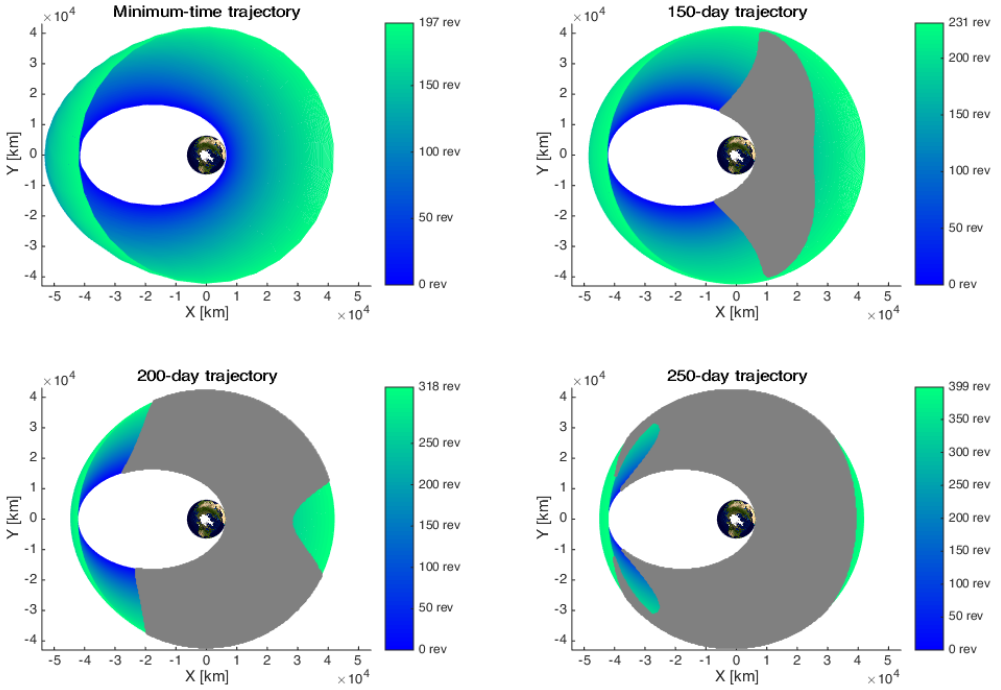

Figure A.11: Minimum-time and minimum-propellant results for the 150-, 200-, and 250-day trajectories.

B

Implementation Details

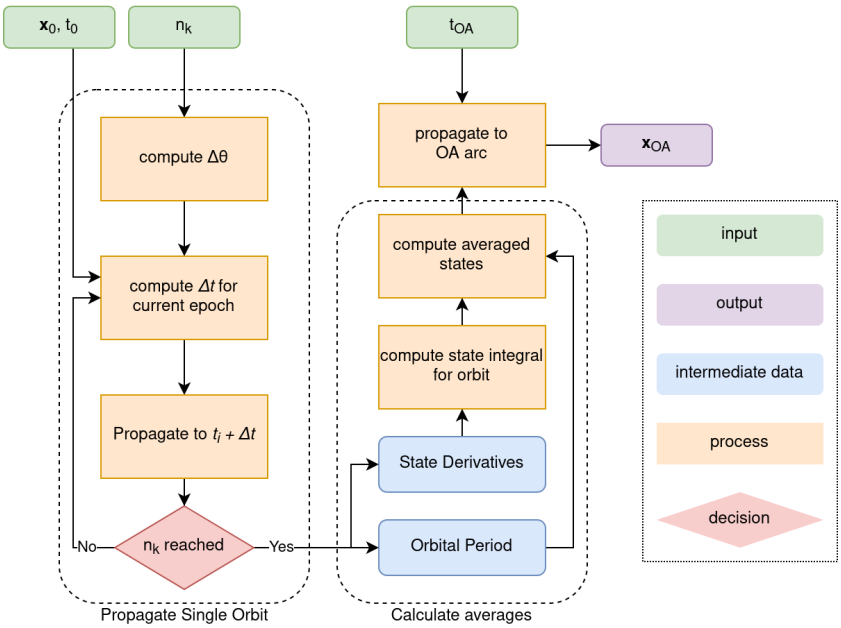

Figure B.1: Propagation Flowchart

B.1. Development Platform

All simulations were run on a desktop computer with specifications:

OS	Ubuntu 20.04.3 LTS
CPU	Intel® Core™ i5-4690K CPU @ 3.50GHz × 4
RAM	16GB DDR3

All simulation code was developed in C++ as part of the Tudat suite[1], supported by the `Boost` and `Eigen` libraries. All analysis was done using Python 3, using the `matplotlib` and `mayavi` packages for data visualization, `numpy` for data handling and mathematical analysis and a custom library was used, providing a range of

[1] `https://tudat.tudelft.nl/`

generic plotting and utilities[2]. This report was written using LaTeX, in a heavily modified version of the TU Delft LaTeX report template.

B.2. Two-line Element Sets

A TLE is a common data format used to encode the orbital elements of Earth-orbiting satellites and other objects, at any given time epoch. The TLE of many objects orbiting Earth are tracked by the United States Air Force, and made publicly available. In the context of this project, TLE are used to obtain accurate orbital elements for target objects and orbits. This section briefly summarizes the TLE format and the method by which it is used. TLE consist of an (optional) satellite name, and two lines containing all data. Their full format is described in Table B.1.

Table B.1: `https://www.celestrak.com/NORAD/documentation/tle-fmt.php`

	Column	Description
Line 1	1	Line Number of Element Data
	03-07	Satellite Number
	8	Classification (U=Unclassified)
	10-11	International Designator (Last two digits of launch year)
	12-14	International Designator (Launch number of the year)
	15-17	International Designator (Piece of the launch)
	19-20	Epoch Year (Last two digits of year)
	21-32	Epoch (Day of the year and fractional portion of the day)
	34-43	First Time Derivative of the Mean Motion
	45-52	Second Time Derivative of Mean Motion (Leading decimal point assumed)
	54-61	BSTAR drag term (Leading decimal point assumed)
	63	Ephemeris type
	65-68	Element number
	69	Checksum (Modulo 10) (Letters, blanks, periods, plus signs = 0; minus signs = 1)
Line 2	1	Line Number of Element Data
	03-07	Satellite Number
	09-16	Inclination [Degrees]
	18-25	Right Ascension of the Ascending Node [Degrees]
	27-33	Eccentricity (Leading decimal point assumed)
	35-42	Argument of Perigee [Degrees]
	44-51	Mean Anomaly [Degrees]
	53-63	Mean Motion [Revs per day]
	64-68	Revolution number at epoch [Revs]
	69	Checksum (Modulo 10)

For example, the TLE of a Vega Secondary Payload Adapter (VESPA) upper part, is

```
AVUM DEB (ADAPTOR)
1 39162U 13021D   21244.09511911  .00000256  00000-0  78198-4 0  9998
2 39162  98.7786 121.7892 0094151 284.1787  74.8959 14.48416320439567
```

The orbital elements given by a TLE can be directly converted to a set of classical Keplerian orbital elements. The semi-major axis is obtained from the mean motion n. The true anomaly is obtained from the mean anomaly, through conversion to the eccentric anomaly, using Kepler's Equation. For obtaining a general orbit to demonstrate the optimization process, this would be sufficient. However, for practical applications, care needs to be taken with this approach. The TLE are updated sporadically, so the elements need to be propagated to the required time epoch. TLE are specifically presented with the simplified perturbations model in mind. Therefore, to accurately obtain the object state, it will need to be propagated using one of the SGP models to propagated to the time epoch of interest.

[2] `https://github.com/RobertKlavers/spacestuff`